APPLICATION OF CONVECTION HEAT TRANSFER IN NEAR-WALL JETS TO ELECTRON-BEAM-PUMPED GAS LASERS

A Dissertation
Presented to
The Academic Faculty

by

Bo Lu

In Partial Fulfillment
of the Requirements for the Degree
Doctor of Philosophy in Nuclear Engineering

Georgia Institute of Technology

August 2010

APPLICATION OF CONVECTION HEAT TRANSFER IN NEAR-WALL JETS TO ELECTRON-BEAM-PUMPED GAS LASERS

Approved by:

Dr. Said I. Abdel-Khalik, Advisor
School of Mechanical Engineering
Georgia Institute of Technology

Dr. S. Mostafa Ghiaasiaan
School of Mechanical Engineering
Georgia Institute of Technology

Dr. Sheldon M. Jeter
School of Mechanical Engineering
Georgia Institute of Technology

Dr. Donald R. Webster
School of Civil and Environmental Engineering
Georgia Institute of Technology

Dr. Michael F. Schatz
School of Physics
Georgia Institute of Technology

Date Approved: June 29, 2010

ACKNOWLEDGEMENTS

First, I would like to thank my advisor Dr. Said I. Abdel-Khalik for his invaluable support, guidance and encouragement throughout my study and research in the thermal hydraulics lab at Georgia Tech. Special thanks go to Mr. Dennis Sadowski for his assistance in designing and constructing the experimental apparatus and his additional help in the experiments and personal encouragement. I would also like to thank Mr. Kevin G. Schoonover for his support and suggestions for the project.

I would like to thank my committee members, Dr. S. Mostafa Ghiaasiaan, Dr. Sheldon M. Jeter, Dr. Donald R. Webster, and Dr. Michael F. Schatz for their advice and recommendations. A special thank you is given to Dr. S. Mostafa Ghiaasiaan for his help in data analysis.

I would also like to thank the many colleagues and fellow graduate students that I have worked with and who helped enhance my Ph.D. research experience. Thanks go to Dr. Lorenzo Crosatti, Dr. Chieh-Chih Hu, Dr. Timothy P. Koehler, Dr. Celine Lascar, Jordan Rader, and James B. Weathers.

Finally and most importantly, I want to thank my beloved wife, Na Wang, who has supported and encouraged me through all the years that we have been separated and also my parents and sister, who always stand behind me and encourage me to achieve what I want in my life.

TABLE OF CONTENTS

CHAPTER 5 IMPINGING JET COOLING OF A HEATED FLAT FOIL 73

LIST OF TABLES

LIST OF FIGURES

LIST OF SYMBOLS AND ABBREVIATIONS

Variables:

α	Constant used in the correlation for planar jet cooling
β	Constant used in the correlation for planar jet cooling
C	Constant used in the correlation for planar jet cooling
d	Jet diameter
ε	Turbulent dissipation rate
h	Heat transfer coefficient
I	Current
k	Thermal conductivity or turbulent kinetic energy
L	Jet-to-foil distance
$\dot{m}$	Mass flow rate
Nu	Nusselt number
μ	Dynamic viscosity coefficient
P	Pressure
Re	Reynolds number
Pr	Prandtl number
q''	Heat flux
ρ	Gas density or resistivity of stainless steel foil
r	Radial distance from the stagnation point
R	Resistance
s	Planar jet width

S	Spacer thickness
T	Temperature
θ	Impinging angle
Φ	Impinging angle
x	Downstream distance from the leading edge of the foil
y	Perpendicular distance from the foil
U	Voltage
W	Foil width or planar jet length

Subscripts:

avg	Average value
min	Minimum value
max	Maximum value
f	Quantities related to the foil
h	Hydraulic
jet	Jet
w	Wall
∞	Bulk flow/free stream

Abbreviations

AC	Alternative current
CFD	Computational fluid dynamics
HTC	Heat transfer coefficient

ICF	Inertial confinement fusion
IFE	Inertial fusion energy
IR	Infrared
KrF	Krypton fluoride
LDV	Laser Doppler velocimetry
NRL	Naval Research Laboratory
T/C	Thermocouple

SUMMARY

Heating of the transmission foil separating the vacuum diodes from the laser gas in electron-beam-pumped gas lasers due to high-energy electron beam attenuation necessitates an external cooling scheme to prevent its failure under repetitively pulsed operating conditions. Attenuation of the electron beam (typically 500 kV, 100 kA and 100 ns pulse duration) produces a strong and pulsed volumetric heat source in the relatively thin stainless-steel foil (thickness of ~25 μm) causing it to fail. An experimental and numerical investigation has been conducted to study the cooling effectiveness of near-wall high-speed jets for a single stainless-steel foil strip that simulates the actual foil geometry between two neighboring support ribs in the Electra KrF gas laser developed by the Naval Research Laboratory. The foil is placed inside a rectangular channel with continuous gas flow to simulate the circulating laser gas. The foil is electrically heated with the heating power input adjusted to achieve the same foil temperatures observed in Electra when no active cooling is applied. Detailed studies include two jet geometries (planar and circular) and two injection methods (tangential/parallel or obliquely impinging jets) for two hibachi foil structure designs (flat and scalloped). The planar jet of ~1mm thickness flows parallel to the circulating laser gas across the entire foil span. The other configuration uses circular jets of small diameters (0.8 mm, 1.2 mm and 1.6 mm) positioned in two staggered rows located on the foil's two vertical edges with a pitch of 1.25 cm over the entire height of the foil. For both configurations, experiments have been conducted at various jet velocities (or jet Reynolds numbers), impingement angles and jet-foil spacing with an aim to identify the optimal operating parameters for the actual hibachi foil cooling.

Numerous investigations have been performed that covered a wide range of operating parameters. Local and average heat transfer coefficients for the foil were obtained and the data indicate that near-wall jets can enhance convection heat transfer by more than one order of magnitude when compared to forced convection that only uses the laser gas recirculation. The locally injected jets only affect the flow field close to the foil and the effect on the bulk flow is very limited, which is crucial to preserve the laser quality. The experimental data will provide the designers of the gas laser system an efficient and cost-effective option for foil cooling for the anticipated operating conditions.

Experimental results have also been compared to the predictions from CFD simulations using FLUENT® with a well-established k-ε turbulence model. Good agreement has been observed for the planar jet cooling experiments in terms of foil temperature and heat transfer coefficients. For impinging jet cooling experiments, a simplified three-dimensional model was developed and qualitative agreement was observed.

The results show that near-wall jets can effectively cool the foil that separates the vacuum diodes from the laser gas under prototypical pulsed (5Hz) operating conditions. The jets can prolong the lifetime of the foil and also minimize impact on electron beam quality and laser efficiency.

CHAPTER 1

INTRODUCTION

Near-wall jets, including both tangential and impinging jets, have been widely investigated and applied as an effective method for heat transfer enhancement for either heated or cooled surfaces. Previous studies were summarized and reviewed by many authors (Goldstein, 1971; Martin, 1977; Jambunathan, *et al.*, 1992; Viskanta, 1993). Typical applications include protection of high-temperature gas turbine blades and other components, paper drying, annealing of metals, and cooling of electronic components. In most applications, the surface is subjected to a high-temperature environment or the component has an inherent heat generating source. To protect the target surface, tangential jets are usually injected near the leading edge of the surface and flow parallel to the surface, increasing convection heat transfer from the surface to the ambient and reducing the surface temperature substantially. However, the cooling effectiveness decays quickly downstream from the injection point due to the mixing of the wall jet with the ambient flow. Additional injection points are desired along the flow direction to provide enough cooling for the entire surface. On the other hand, impinging jets can cool the entire surface when multiple discrete jets are used to cover a large portion of the surface to be cooled, thereby achieving a more uniform surface temperature profile. The enhancement in convection heat transfer of impinging jets depends on jet Reynolds number, jet arrangement, and jet impingement angles. The geometry of the jet also affects the overall performance. The motivation of this dissertation research derives from the development of an electron-beam-pumped gas laser system for inertial confinement fusion energy research, where the cooling of the thin transmission foil separating the vacuum diodes from the high pressure laser gas presents a formidable engineering challenge to the designers of the laser driver system.

1.1 Background

1.1.1 Inertial confinement fusion and driver technology

Nuclear fusion provides the enormous energy source for the sun and other stars in the universe. In a fusion reaction, energy is released when light elements, such as hydrogen isotopes, combine to form a heavier element. Nuclear fusion is believed to be capable of providing nearly unlimited energy to the human race because there is a nearly inexhaustible supply of the hydrogen isotope deuterium in seawater. In order to garner this energy source for long-term energy supply on earth, researchers around the world have been working on controlled nuclear fusion for more than 50 years to solve the difficulties involved in initiating and sustaining a fusion reaction.

One promising technique for controlled nuclear fusion is inertial confinement fusion (ICF), in which nuclear fusion reactions are initiated by compressing and heating a fuel pellet comprised of deuterium and tritium atoms through external drivers. The reactions are subsequently maintained by the energy released in previous fusion reactions (Figure 1-1). As a result of change in the mass before and after the fusion reaction, energy is released mainly in the forms of fusion products' kinetic energy. One of the key components in ICF research is the external driver, such as high-energy laser beams, electron beams, or ion beams, which supply energy to the target pellet to initiate the reaction. The outer layer of the fuel pellet is first heated and compressed to a very high temperature and pressure by the rapid energy release from the driver, causing it to explode outwards. The explosion creates a reaction force upon the inner target layer. This force accelerates the layers inward and also drives shock waves into the center. If the shock waves are powerful enough, the fuel target can be highly compressed and heated at its center for a fusion reaction to take place. Energy released from the fusion reaction in the center heat the surrounding fuel and more fusion reactions can occur. The aim of ICF is to create an environment in which the reactions are first ignited and sustainable reactions are maintained to burn the fuel pellet.

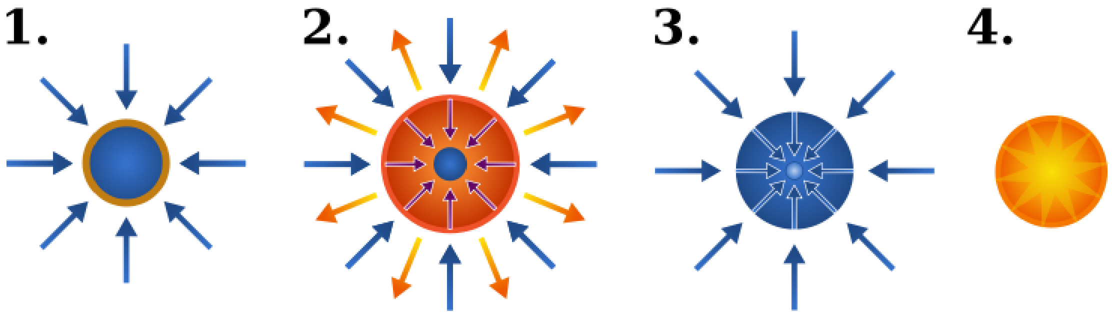

Figure 1-1 Schematic of inertial confinement fusion process

1.1.2 ICF laser driver mechanism

Current research activities on ICF driver technology mainly focus on high-energy laser driver system development, which include both diode-pumped solid-state lasers and electron-beam-pumped gas lasers (Bayramian, *et al.*, 2003; Sethian, *et al.*, 2001, 2003 and 2004). As one of the key components of ICF driver technology, “Electra”, a high-energy krypton fluoride (KrF) laser, has been developed and constructed at the Naval Research Laboratory. Electra is an electron-beam-pumped KrF excimer (excited dimer) laser designed to operate at a repetitive rate of 5 Hz with a laser energy output of 400-700 J, which is to be scaled to 15-25 kJ laser energy for an inertial fusion power plant module (Figure 1-2).

The laser generation mechanism shown in Figure 1-3 and Figure 1-4 starts by applying a pulsed voltage to the emission diodes to generate two pulsed electron beams (~100 ns), which pass through a thin transmission metal foil that isolates the vacuum diodes from the laser gas which is pressurized to ~1.5 atm. Electron beams are fired on both sides of the laser cell and excite the krypton fluoride gas in the laser cell. An input laser at low power triggers the system to emit an amplified laser beam at higher intensity when KrF^* de-excites to its ground state. The wavelength of the resulting KrF laser is 248 nm (ultraviolet). The laser gas, which has a total volume of 9,000 liters, is recirculated using a blower in a closed loop system (Figure 1-5). Gas flowing through the laser cell serves to homogenize the laser gas and help cool the transmission foil. To ensure a uniform amplified laser beam, it is important that the gas within the laser cell return to a relatively quiescent state between consecutive electron beam firings. If the bulk velocity of the gas in the laser cell is too high, the quality of the laser beam will deteriorate.

Figure 1-2 Electra at the NRL (laser cell open and recirculator detached, Sethian, *et al*, 2001)

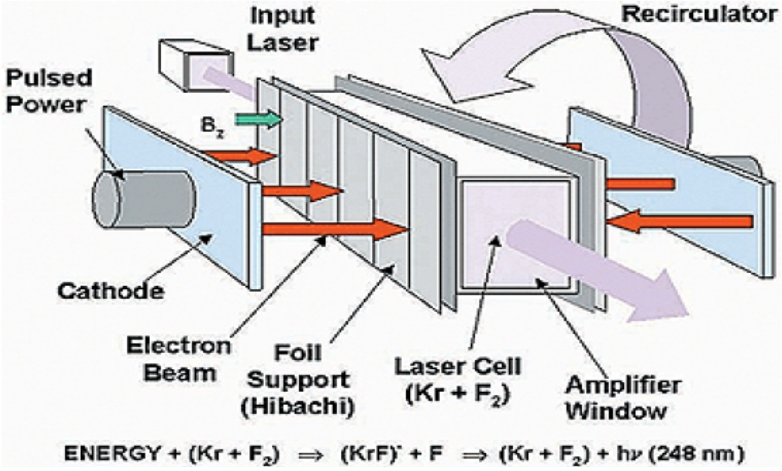

Figure 1-3 Electra KrF laser generation mechanism in laser cell (Sethian, *et al*, 2003)

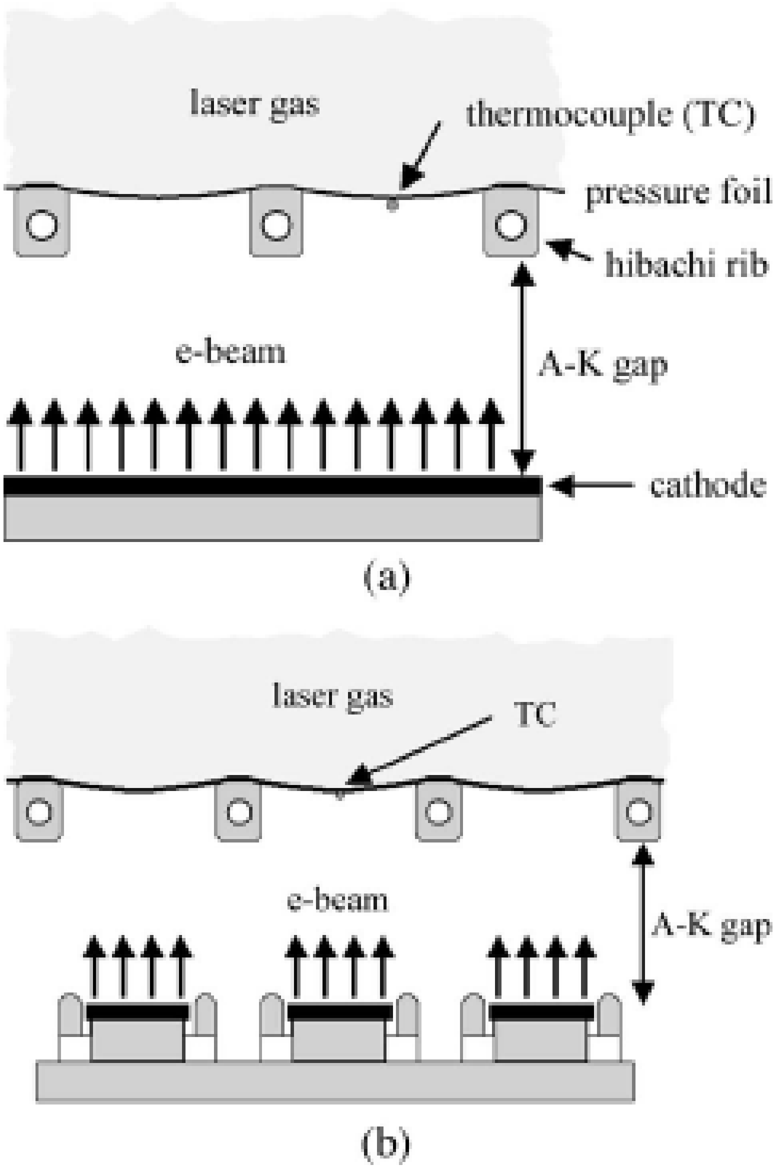

Figure 1-4 Schematic of the e-beam firing with temperature measuring setup. (a). Monolithic cathode; (b). Strip cathode (Hegeler, *et al*, 2005)

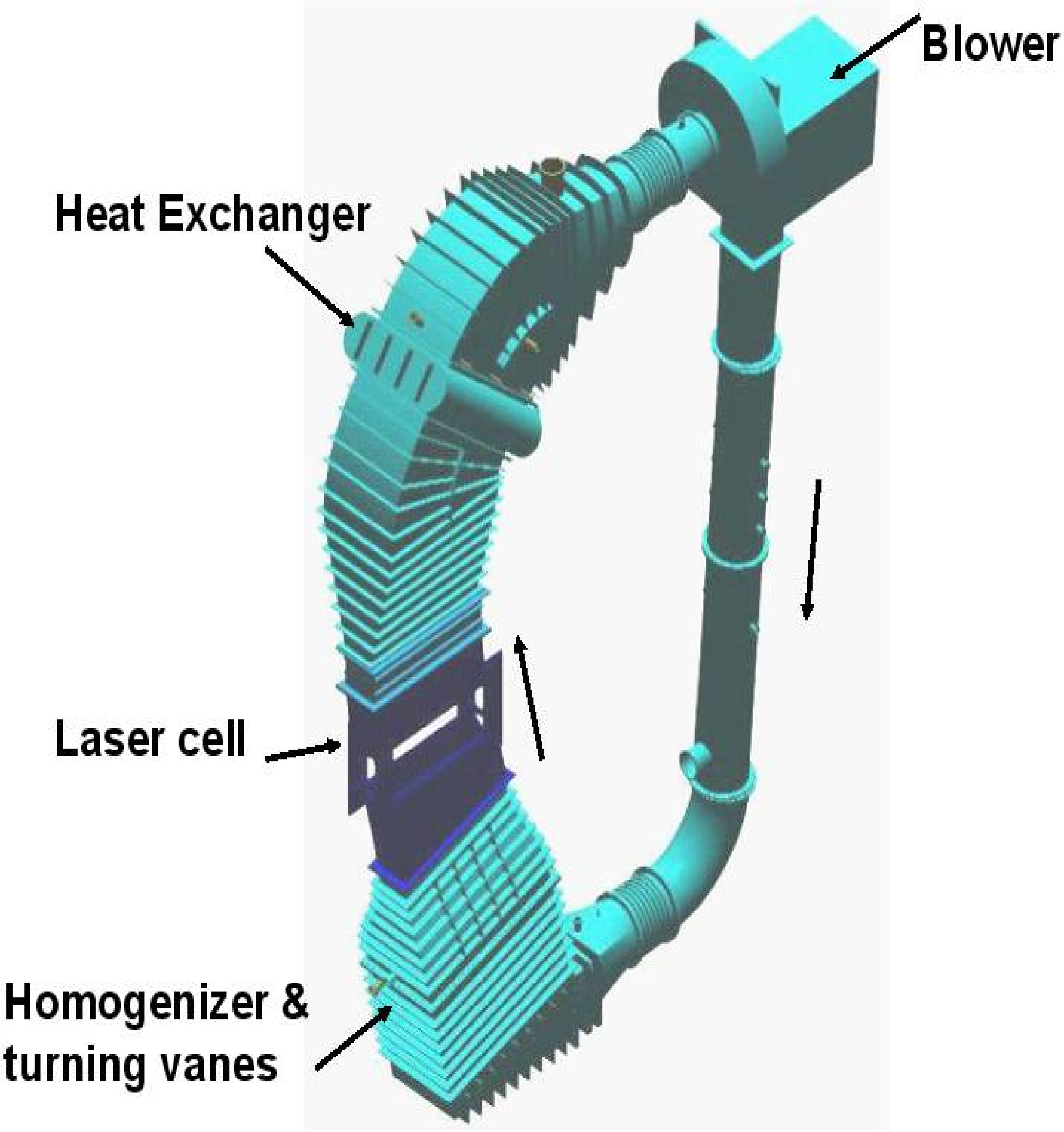

Figure 1-5 Schematic of Electra recirculator loop
(Black arrows showing the flow direction of the laser gas, Sethian, *et al*, 2003)

1.1.3 Hibachi foil and cooling

A hibachi-like structure (hereafter, hibachi) is used to support the foil that separates the vacuum diodes from the laser gas in the laser cell. Design of the foil and hibachi structure presents a formidable technical challenge, because the foil must be highly transparent to the electron beam (≥75% transmission), withstand the static pressure force from the laser gas, and also survive the very hostile environment present in the laser cell (including cyclic hydrodynamic shock, ultraviolet light, X-rays, electrons, fluorine and hydrogen fluoride) (Sethian, *et al.*, 2003). The search for qualified foil materials included testing of materials such as titanium, aluminum, silicon, and alloys such as HAVAR and HASTELLOY. Ultimately, a 25 μm-thick type-304 stainless-steel foil was chosen (Sethian, *et al*, 2004). The selected material with chosen thickness is believed to satisfy the following requirements for rep-rate operation of electron beam firing:

1. High electron transmission efficiency (≥75%)
2. Long lifetime ($>10^8$ shots projected for two years at 5 Hz between major maintenance of the laser system)
3. Operating in a very hostile environment

However, preliminary experiments at the NRL showed that the stainless steel foil quickly reached a very high temperature (>600 ^{o}C) and that operation at such elevated temperatures caused the foil to fail after a few hundred shots at the 5 Hz rep-rate (Hegeler, 2007). Figure 1-6 and Figure 1-7 show an example of a failed foil and its temperature history for 21 shots at 5 Hz when a monolithic cathode was used and the laser gas was quiescent. To improve the durability of the foil, it needs to have good mechanical strength and ductility and also be resistant to the laser gas, especially to fluorine. The key to the enhancement of the durability of the foil and the long-term rep-rate operation of the laser is to keep the foil sufficiently cool.

Several cooling schemes have been proposed and investigated during the past years to identify an efficient way for foil cooling; these include:

1. Radiation cooling (Hegeler, *et al.*, 2005)
2. Conduction cooling through the water-cooled hibachi ribs (Giuliani, *et al.*, 2006)
3. Convection cooling using oscillating louvers (Hegeler, *et al.*, 2005 and 2008)
4. Convection Cooling using air-water mist flow (Novak, *et al.*, 2005 and 2007)

Radiation cooling is efficient only if the foil is at very high temperatures, but then the mechanical strength of the foil would be substantially reduced, compromising its durability. Conduction cooling is inherent in Electra due to the fact that the hibachi ribs were designed to include channels with circulating water to remove the excess heat from the ribs. However, heat removal from the foil by conduction is severely limited because of the thinness of the foil and the poor thermal conductivity of type 304 stainless steel. Also, the ribs are made of MP35N Carpenter steel which has a relatively low thermal conductivity. This means there is relatively little heat transfer between the water flowing in the ribs and the foil pressing against the outer surface of the ribs. Although radiation and conduction cooling help cool the hibachi foil, they only contribute as secondary cooling effects.

Figure 1-6 A picture of a failed hibachi foil on Electra (Hegeler, F., *et al*, 2007)

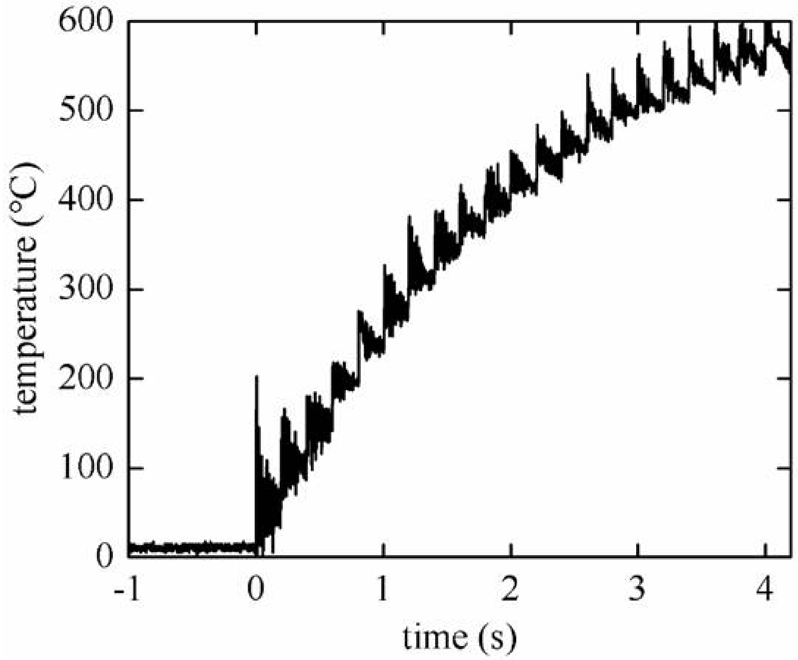

Figure 1-7 Temperature history of hibachi foil without active cooling after 21 shots at 5 *Hz* (Hegeler, F., *et al*, 2007)

Another potential foil cooling method is to utilize the flow of laser gas driven by the blower, since Electra is designed to recirculate the laser gas between two consecutive e-beam shots in order to quench the gas and improve the laser beam quality. Experimental studies have been carried out on Electra to test the thermal loads on the stainless-steel foil due to e-beam attenuation and to measure the foil temperature under various rep-rate operation conditions (Giuliani, *et al*, 2006; Hegeler, *et al*, 2005 and 2008). To improve forced convection cooling of the foil, louvers were also installed upstream of the hibachi window. These louvers operate in two different modes/positions: "open" and "closed," or "actuated" (Figure 1-8).

Experiments showed that without any active cooling schemes except radiation and conduction, the foil temperature rose to 480 ^{o}C after a short 15-shot burst at 5 Hz. When the louvers were fully open and the blower drove the laser gas at a relatively uniform velocity of ~7.5 m/s continuously, the foil temperature stabilized at ~430 ^{o}C due to turbulent forced convection heat transfer. By actuating the louvers so they were only closed for 100 ms between two shots, the foil temperature further decreased to 325 ^{o}C. This is because the laser gas was forced through two narrow channels, thus significantly increasing the gas velocity past the foils. When the louvers were kept fully closed, the best cooling was achieved and the maximum temperature was only 265 ^{o}C due to the fact that more laser gas flow was diverted towards the foil at relatively high speed, thereby increasing the forced convection heat transfer rate. While achieving acceptable foil cooling performance, this setup produced significant heterogeneities in the laser gas that both prolonged the time for recovery of the wavefront and severely compromised the laser beam uniformity (or focal profile) (Burns, *et al*, 2009).

Mist cooling was also proposed and found to be highly effective at cooling the foil. This method incorporates a very thin liquid film that is attached to the foil and evaporates (Novak, 2005 and 2007). To prevent the liquid from mixing with the laser gas, this method requires a two-foil arrangement which increases the system complexity (Figure 1-9). The e-beam needed to pass through two foils and the water mist, which significantly increased the portion of e-beam energy lost to attenuation. This, in turn, decreases the overall system efficiency, and also potentially adds unwanted material (such as water) into the laser cell, the diodes, or both in the event of a foil failure.

The search for another foil cooling method continued. Any new method must be efficient at cooling the foil using the limited power available for pumping. It also should not affect the laser beam quality significantly. The idea of using near-wall jets was suggested (Lu, *et al.*, 2009). The advantage of using near-wall jets is that the coolant can be the same medium as the laser gas. Also the effect on the flow field due to local near-wall jet injection is nearly negligible, so it has minimum impact on the laser beam uniformity compared to those previously investigated methods.

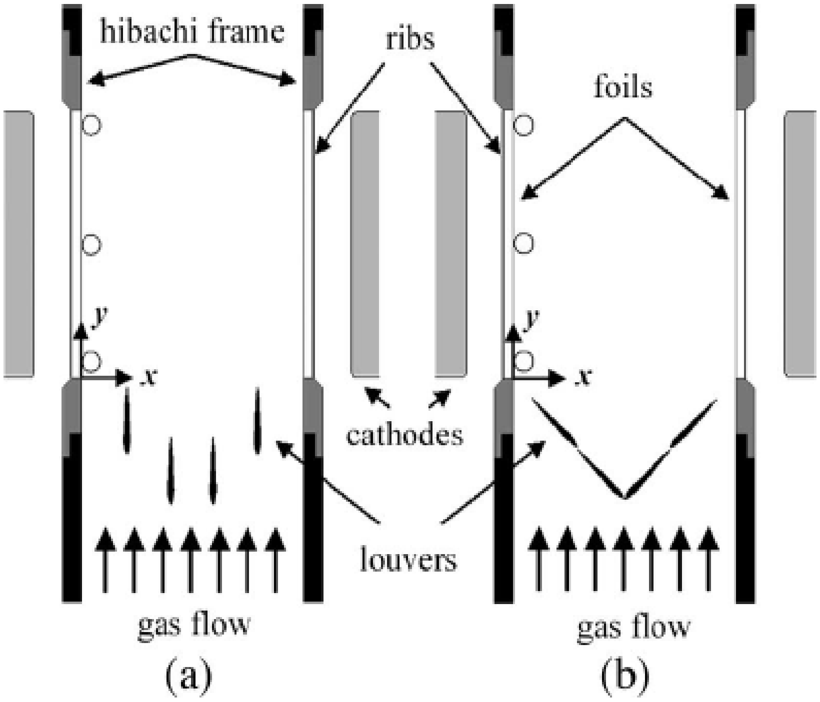

Figure 1-8 Foil cooling with louvers installed upstream of the laser window
(a). open position mode; (b). closed or actuated position mode (Hegeler, *et al*, 2008)

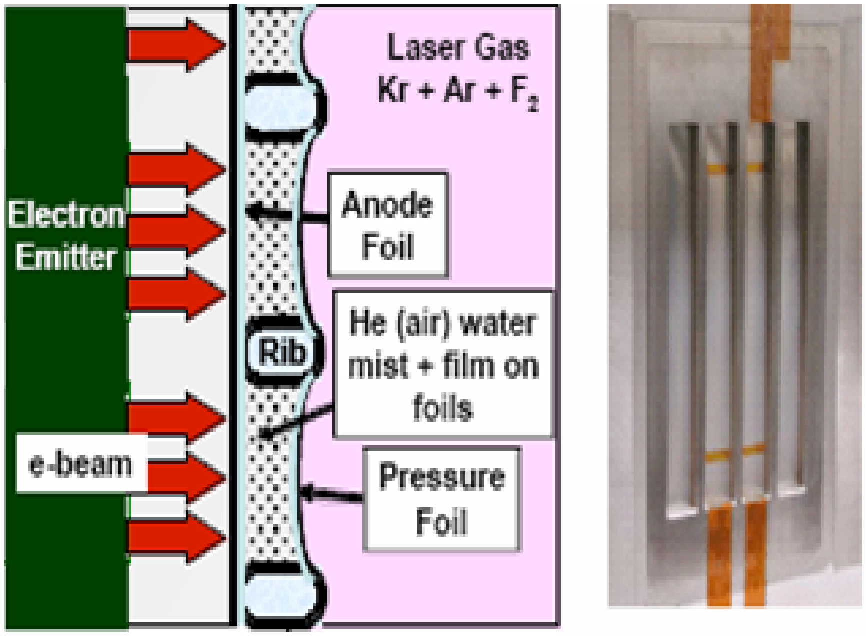

Figure 1-9 Mist cooling for hibachi foil (Novak, *et. al.*, 2007)

1.2 Objectives

The objective of this dissertation research is to examine the effectiveness of near-wall jets applied to foil cooling in electron-beam-pumped gas lasers using experimental studies and CFD simulations. Air jets are used in most experiments at a wide range of velocities covering the expected Reynolds number range of the actual system. The foil is electrically heated to achieve the temperature observed in the Electra KrF laser when only radiation cooling is used. A bench-top experimental rig has been designed and constructed with the capability of using planar tangential and circular impinging jet configurations. For the flat foil hibachi design, both tangential planar jets and impinging jets have been examined, while for a scalloped foil design only the cooling effectiveness of impinging jets has been studied. A 25 μm-thick stainless steel foil strip representing the foil geometry and shape between two support ribs in the actual Electra hibachi structure is vertically attached to two copper rods acting as electrodes and is spring tensioned in order to keep its original shape when it undergoes thermal expansion. The foil is either flat or scalloped to match the actual configurations in two different hibachi designs. The rig is equipped with a fan driving a bulk flow to simulate the circulating laser gas stream. Jet diameter, jet velocity, spacing between jet openings, and impingement angles are controlled and the corresponding cooled foil temperature profiles are measured using either thermocouples or infrared thermal imaging techniques. CFD simulations using FLUENT® have been conducted and the results have been compared to the experimental data. CFD tools can be used to predict the flow field and heat transfer characteristics which are difficult to measure experimentally. The aim is to identify the optimal configuration parameters for best cooling effects: jet speed, jet diameter, nozzle-target spacing and impingement angles at the acceptable cost of pumping power and system complexity.

The remainder of this dissertation is organized as follows. Chapter 2 provides a literature review of forced convection heat transfer in both tangential and impinging jets. Chapter 3 provides detailed descriptions of the experimental apparatus and procedures used in this investigation. The experimental and numerical results pertaining to planar tangential jets are presented in Chapter 4, while those for impinging jets are presented in Chapter 5 and Chapter 6 for the flat and scalloped foils, respectively. Conclusions and recommendations are given in Chapter 7. An uncertainty analysis of the data is given in Appendix A, while a detailed listing of all the experimental data obtained in this investigation in given in Appendix B.

CHAPTER 2

LITERATURE REVIEW

2.1 Introduction

In this chapter, literature reviews on forced-convection heat transfer for both tangential planar jets and impinging jets are presented.

2.2 Tangential Planar Jets

Tangential jets have been investigated for many decades to study the effects of various design and operational parameters on the convection heat transfer from the target surfaces. The jet flows along the surface either to enhance heat transfer from the surface to the ambient or to protect the surface that is exposed to an extremely hot environment (Figure 2-1). The term “film cooling” is exclusively used to refer to the latter case, where a second fluid stream is introduced into the boundary layer of the target surface which is exposed to a high-temperature gaseous environment. The jet is used here to reduce the heat transfer to the surface and to some extent acts as a shield protecting the surface from the surrounding hostile environment.

2.2.1 Experimental studies of planar jets

Extensive experimental studies on fluid flow and heat transfer characteristics of planar jets have been performed that mainly focused on the applications of film cooling. This part of the literature review only covers those studies where the jet geometry and other operating parameters closely relate to the current research project.

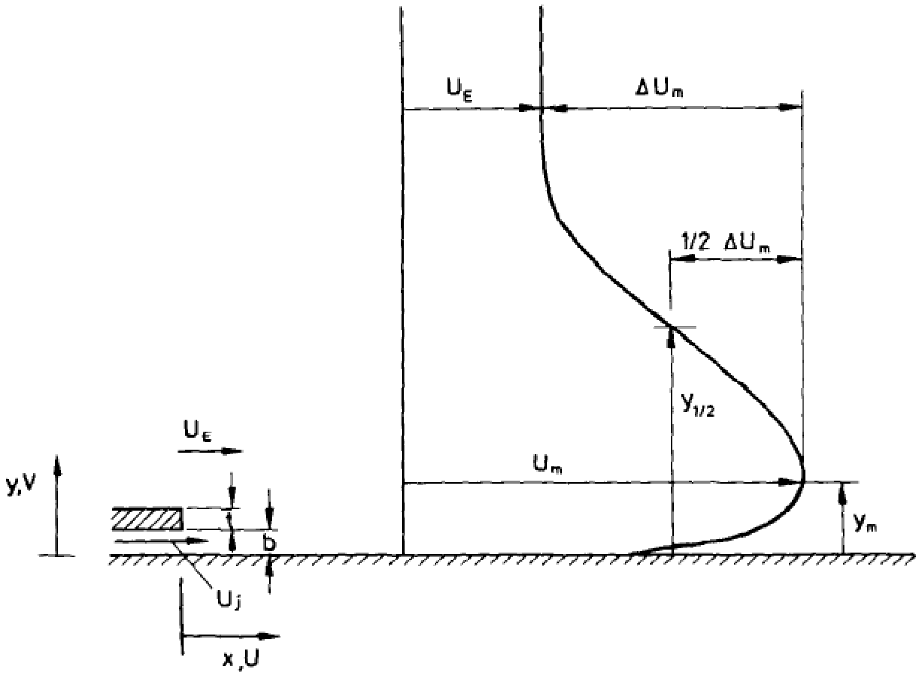

Figure 2-1 Wall planar jet and its velocity distribution (Launder and Rodi, 1983)

Wieghardt (1946) first experimentally studied the use of injecting a two-dimensional slot jet of hot air into the turbulent boundary layer of a wall as a de-icing method with the secondary jet parallel to the main stream. He measured wall temperature distribution downstream from the injection slot. The effect of the coolant entrainment in the mainstream as a function of injection angles was evaluated for different blowing ratios. He also derived a similarity expression for gas phase temperature as a function of the local thermal boundary thickness. Seban (1960) also performed experiments using a tangentially injected air jet but with a slightly different slot geometry and reported a different correlation for the dimensionless wall temperature from Wieghardt’s. Hartnett, Birkebak and Eckert (1961) extended Wieghardt’s experiments with detailed wall temperature and flow measurement at various heat inputs while using the same slot geometry. A correlation for cooling effectiveness was derived from their experiments and was shown to be consistent with the theoretical calculation by Klein and Tribus (1953), which assumed a line heat source at the leading edge of a flat surface and was based on an enthalpy balance. Seban and Back (1961) again performed velocity and temperature measurements on an approximated wall jet and confirmed the velocity profile predicted from the wall-jet theory, plus a reasonable agreement between the adiabatic temperature profiles.

To tackle the discrepancy existing in the experimental results, Stollery and El-Ehwany (1965) suggested slot Reynolds number must be taken into account when comparing the film cooling effectiveness between different experiments, even though there might be only small difference in the slot geometries. This led to the need to well characterize the inlet conditions including mean profiles and turbulence statistics to identify effects of turbulence intensity in film cooling performance.

For simplicity, the aforementioned correlations all assumed a fully developed turbulent boundary layer. For the developing flow near the injection region, Ballal and Lefebvre (1973) developed a correlation based on direct measurement of skin friction coefficients for both low and high blowing ratios. Goldstein (1971) gave a high-quality and comprehensive review of previous experimental studies on film cooling and scaling laws, which covered a wide range of jet slot geometries, temperature ratios, and blowing ratios. Another review by Launder and Rodi (1983) focused on the theory and modeling of the turbulent wall jet. The effect of foreign gas injection on the heat transfer was well characterized by Burns and Stollery (1969).

Lefebvre (1999) summarized the correlations appropriate for calculation of temperature and Nusselt numbers of a film-cooled wall, where

$$Nu_x = \frac{h_x x}{k_c} = \begin{cases} 0.069\left(\mathrm{Re}_s\, x/s\right)^{0.7} & 0.5 \le m \le 1.3 \\ 0.10\,\mathrm{Re}_s^{0.8}\left(x/s\right)^{0.44} & m > 1.3 \end{cases} \qquad \text{Eq. 2-1}$$

Here Nu_x is the local Nusselt number, Re_s is the Reynolds number defined as: $Re_s = \rho_{jet} V_{jet} s / \mu$, where s is the slot width and x is the distance from the leading edge. The parameter "*m*" is the "blow ratio" and is defined as the mass flux ratio between the jet and the bulk flow ($m = \rho_{jet} V_{jet} / \rho_\infty V_\infty$).

The correlations above used assumptions such as constant properties and did not account for the effect of turbulence intensity explicitly. Simon (1986) developed a method for calculating film cooling effectiveness, which included the effect of turbulence level. This more sophisticated method was based on a wall-jet analysis (Launder and Rodi, 1983), where the turbulence intensity in the slot flow and mainstream flow were explicitly used as part of the inputs.

More recently, with interest in high-speed aircraft propulsion growing rapidly, more effort has been devoted to film cooling studies. In such aircraft, the engine is exposed to very high heat loads due to a high thrust requirement at launch and aerothermal heating at high Mach numbers. Using detailed and novel turbulence and temperature measurements, Cruz and Marshall (2004 and 2007) did detailed studies of film-cooled surfaces, examining wall temperature, adiabatic effectiveness, and turbulence intensity. Their results confirmed the previously proposed scaling laws for far-field measurements, but underpredicted the significance of temperature ratio between the cooling stream and the mainstream.

2.2.2 Numerical simulations of planar jets

With increases in computing power, CFD simulations provide a strong engineering tool for modeling near-wall tangential jets. Various turbulence models have been adopted in an effort to identify a suitable set that produces good agreement between the simulations and experiment results.

Zhou, Salcudean and Gartshore (1993) first applied the standard k-ε turbulence model plus a near-wall low Reynolds number k model to near-wall jet modeling and showed good agreement with experimental data for velocity profiles and heat transfer enhancement at relatively low mass flow ratios. Jansson, *et al.* (1994) used an algebraic stress model and the standard k-ε turbulence model to simulate slot film cooling. Numerical results showed excellent agreement with experiments for the velocity profiles but not for temperature profiles. The authors surmised that the difference might be due to the way in which the transport equation modeled the temperature field. A more recent CFD study by Roy, et al (2003) adopted detached-eddy simulation (DES), combining Reynolds-averaged Navier-Stokes equations (RANS) near the wall and large eddy simulation (LES) for the region further away from the wall when discrete jets were used to cool a flat plate.

2.3 Impinging Jets

Impinging jets are also widely investigated and employed in various industrial applications and research projects for local heat/mass transfer rate enhancement on the target surface. A round/slot single jet, and more frequently an array of jets, impinges on the surface with very short flow paths to achieve high convection heat transfer rates. Typical industrial applications include the annealing of metal and plastic sheets, glass tempering, and paper and textile drying. Recently, impinging jet cooling has been of much interest for cooling electronic components and photovoltaic cells, where high heat generation occurs. A large number of investigations have been carried out in efforts to characterize momentum and heat and mass transport processes involved in jet impingement by varying jet diameter, jet velocity and distance between the nozzle exit and impinging surface.

2.3.1 Experimental studies of impinging jets

2.3.1.1 Single impinging jet

Extensive investigations of flow characteristics and heat transfer exist in the literature for the single impinging jet. When there is no cross flow present, the flow structure of an impinging jet is well described by dividing the flow field into three different regions: the free jet region (near the jet exit), the impingement region where the jet physically impacts on the surface, and the wall jet region where the jet exits after interaction with the wall (Figure 2-2) (Incropera and DeWitt, 2003). The jet is called submerged if the jet and the surroundings are of the same fluid, otherwise it is considered as a free jet. The jet can also be classified as a confined jet if the jet spread is confined between the impingement surface and the jet plate; it is an unconfined jet if the jet expansion is not contained. Heat transfer in single jet impingement is governed by jet Reynolds number, jet-to-plate spacing, and jet impact angle on the target plate, which was well documented in many researchers' work.

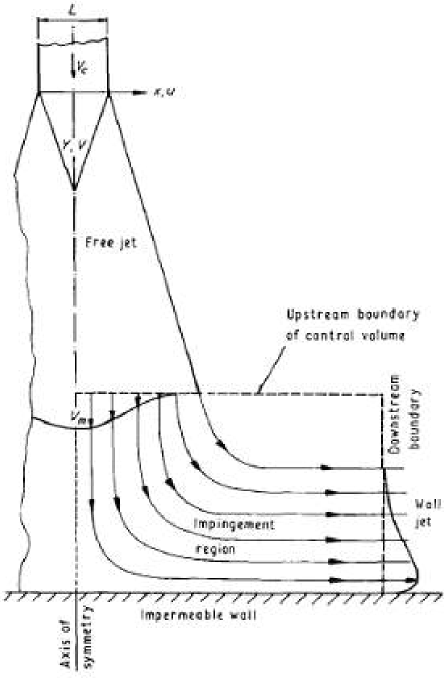

Figure 2-2 Schematic of an axisymmetric single impinging jet (Russell and Hatton, 1972)

An early comprehensive experimental study on impinging jet heat transfer was performed by Perry (1954). Heat transfer measurements were done at various air jet impinging angles and a fixed jet-to-plate spacing for temperature differences greater than 400 ^{o}C and Reynolds number varying from 7,000 to 30,000. The data showed that the heat transfer rate at an impingement angle of 90^{o} was approximately twice the value at 15^{o} at the same Reynolds numbers. It was also noted that at an attacking angle other than 90^{o}, the heat transfer was not maximum at the impacting point but shifted towards the forward jet direction. At fixed jet-to-foil spacing, Nusselt numbers were well correlated in the same form as those for forced convection in external flows over a flat plate and were power functions of jet Reynolds number. The relationship was confirmed by many other people's work with varying coefficients mainly due to the different ranges of experimental parameters (Martin, 1977; Jambunathan, 1992, Huang and El-Genk, 1994, Lin, Chou and Hung, 1997). A typical plot of stagnant Nu vs. Re_d is shown in Figure 2-3 (Smirnov, Verevochkin and Brdlick, 1961), where Nusselt numbers increased linearly with Reynolds numbers in a log-log plot.

Smirnov, Verevochkin and Brdlick (1961) studied the stagnant heat transfer from a normally impinging water jet to a fixed plate both as a function of jet Reynolds numbers and jet-to-plate distances. They first incorporated the dimensionless jet-to-plate spacing in the correlation of Nusselt number and concluded that the Nusselt number exponentially and monotonically decreased as the normalized jet-to-foil spacing increased.

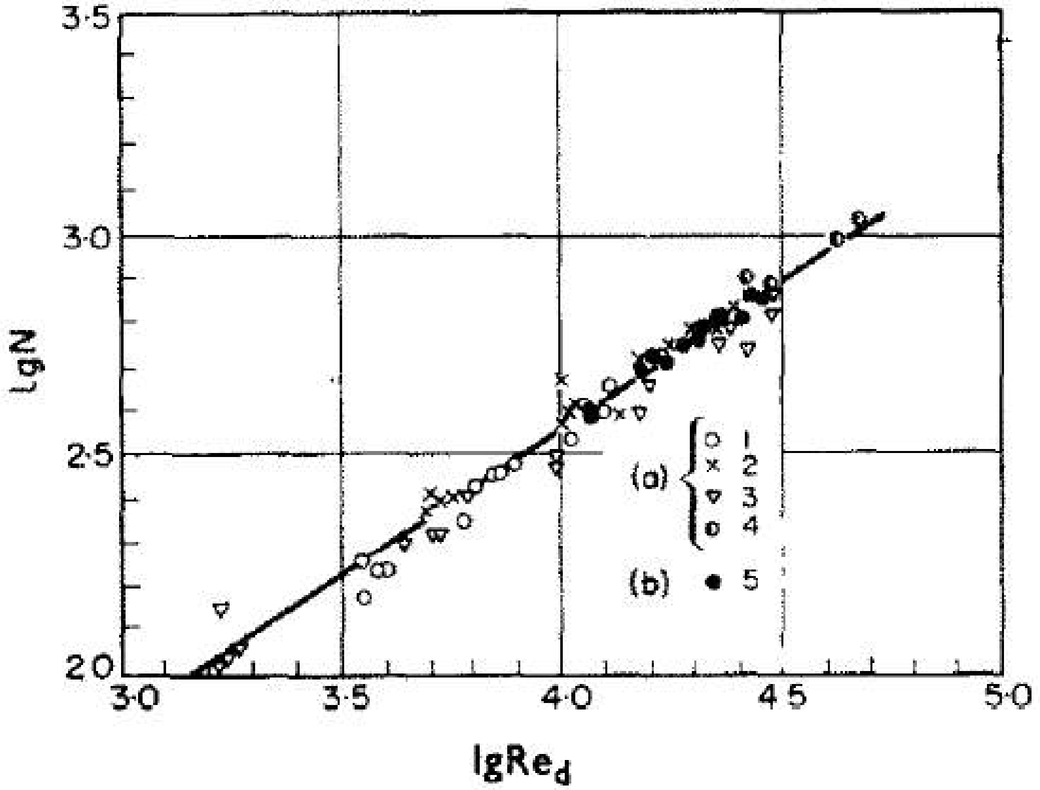

Figure 2-3 Dependence of Nusselt numbers on Reynolds number
(Smirnov, Verevochkin and Brdlick, 1961)

Gardon and Akfirat (1966) extended the range of jet-to-plate spacing and jet Reynolds number in their experimental investigations and concluded that when the jet Reynolds number exceeded a certain threshold (~3,000), stagnation Nusselt number first increased, reached its maximum, and then decreased when the jet exit move further away from the impingement plate (Figure 2-4). They explained that these disturbances/humps were caused by the mixing-induced turbulence, especially in the regions where the turbulence was not fully developed, which resulted in the non-monotonic variation of stagnation heat transfer coefficients (Gardon and Akfirat, 1965).

The local heat transfer coefficients with respect to radial distance away from the impingement point of a normally impinging jet were also very important in understanding the distribution and average heat transfer enhancement for the area around the jet impingement. It has been found that local Nusselt numbers generally followed a bell-shaped monotonically decreasing trend from the stagnation point when the normalized jet-to-plate distance is greater than a certain value. Gardon and Akfirat (1966) reported a value of 14 for a slot jet and Goldstein, *et al.* (1986) reported a value of 8 for a circular jet, both of which were unconfined. Garimella and Rice (1995) and San, Huang and Shu (1997) reported a much smaller value of ~2 for a confined and submerged circular jet. However, when the jet-to-plate spacing was further decreased, secondary maxima at smaller values emerged in the radial profile of the local heat transfer coefficients (Jambunathan, *et al*, 1992; Garimella and Rice, 1995; Glynn and Murray, 2005, Zhou and Lee, 2007). Typical results for the lateral distribution of heat transfer coefficient taken from Zhou and Lee (2007) are shown in Figure 2-5. These studies showed that the secondary peaks almost identically appeared near the location with $r/d_h=2$ (where r is the radial distance from the impingement point and d_h is the hydraulic diameter of the jet). It was explained that the secondary peaks resulted from the elevated turbulence level in the wall jet region, where the transition to turbulence occurred.

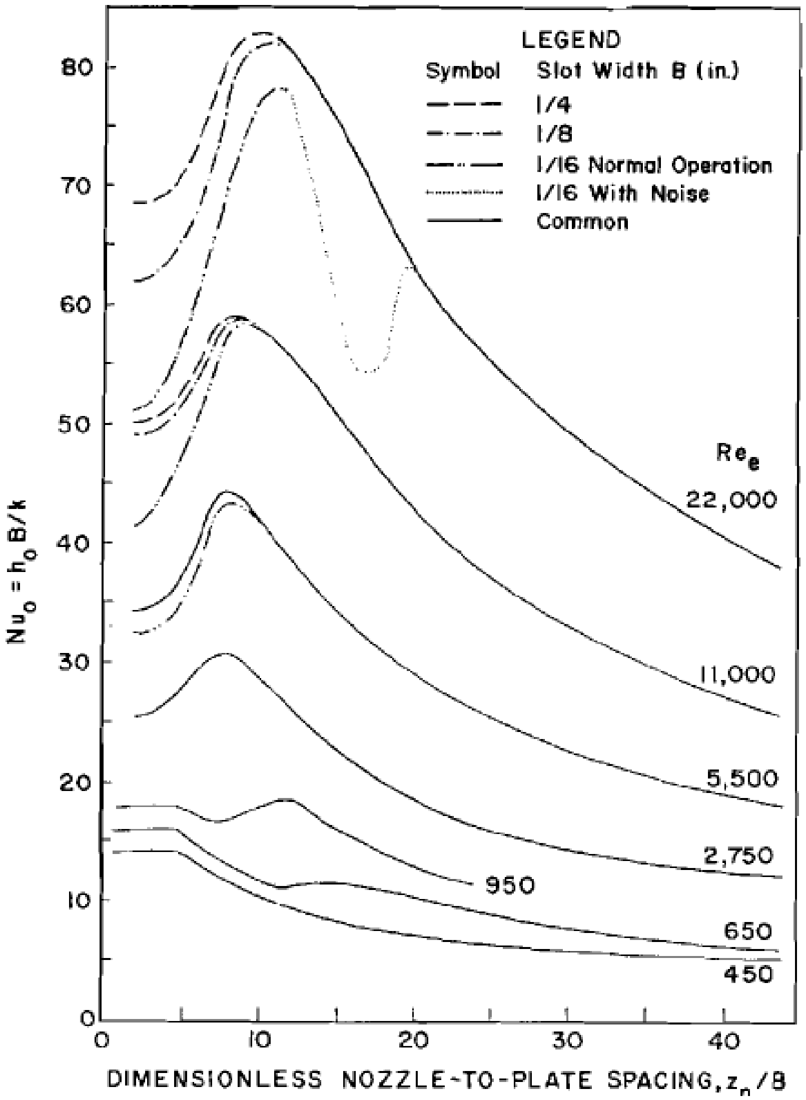

Figure 2-4 Correlation of Nusselt numbers of a two-dimensional impinging jet (Gardon and Akfirat, 1965)

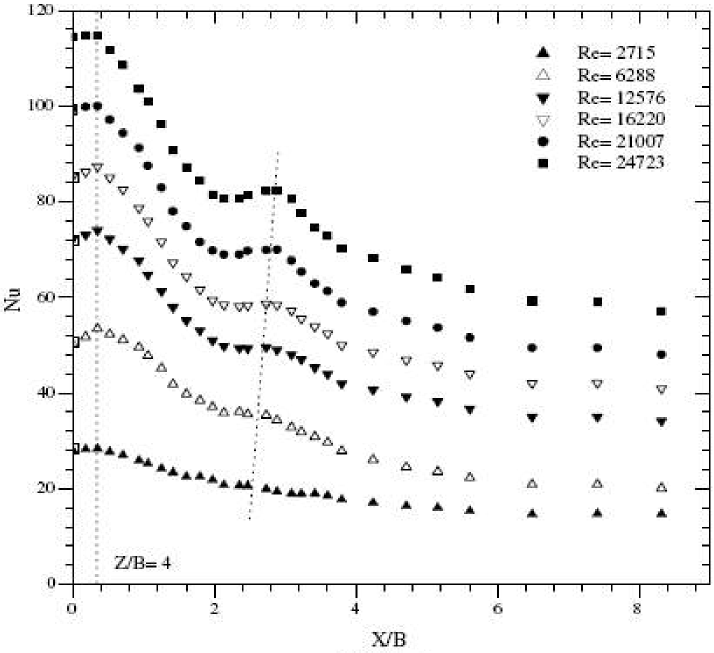

(a) Z/B= 4

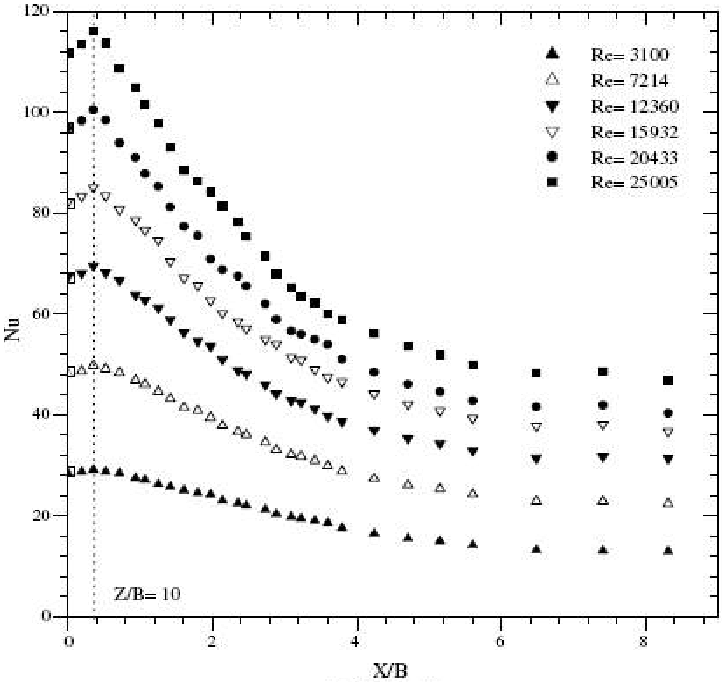

(b) Z/B= 10

Figure 2-5 Lateral variation of local Nusselt number at various jet-to-plate spacings (Zhou and Lee, 2007)

As most studies were focused on the heat transfer of an impinging jet for a flat surface, heat transfer of a jet impinging on surfaces of other shapes are also of engineering significance, in which the curvature effect needs to be taken into consideration due to the centripetal force induced flow instability (a.k.a. Taylor-Gortler type vortex). Chupp, *et al.* (1969) and Metzger, *et al.* (1969) both measured heat transfer coefficients on a parabolic concave surface and studied the effects of the curvature of the cooled surface and the nozzle plate. To further understand the flow characteristics, Gau and Chung (1991) visualized the jet flow impinging on both convex and concave semi-circular surfaces and found distinct characteristics of both flow field and heat transfer on these surfaces. Yang, *et al.* (1999) studied slot jet impingement cooling on a concave surface and the effects of jet nozzle shape and curvature were also identified. Choi, *et al.* (2000) extended the study of slot jet impingement cooling on a concave semi-circular surface by performing detailed flow measurement using laser Doppler anemometry technique (LDA).

Another important factor affecting the heat transfer in impinging jets is the sweeping effect of a cross flow, which occurs in many engineering problems, such as internal turbine blade cooling. The cross flow modifies the jet flow upon impingement. It shifts the stagnation point downstream and also reduces the heat transfer coefficients at the stagnation point. The axisymmetric distribution of heat transfer coefficients around the impingement point is also distorted. Bouchez and Goldstein (1975) first studied the effect of a constant cross flow on the impinging jet cooling for various jet blow rates. The heat transfer measurement indicated at a larger jet-to-plate distance, the stagnation point was more shifted downstream. Also, the heat transfer coefficients were smaller than those reported in the literature when no cross flow was present and the normalized jet-to-plate spacing was greater than 6. The interaction between the jet and the cross flow also created a recirculation zone upstream of the stagnation point. Goldstein and Behbahani (1982) extended the experimental studies by varying the cross flow rate and found at small jet-to-plate spacing, moderate cross flow enhanced the stagnation heat transfer coefficient. Cross flow also arises naturally as the spent gas spreads when multiple confined impinging jets are used. A review of these studies is covered in the next section.

2.3.1.2 Array of impinging jets

The studies on single jet impingement heat transfer indicate that only a very small area around the impingement point sees the enhancement in heat transfer rates. Far from the stagnation point, the heat transfer coefficient decays rapidly to the same value as if there is no jet present due to the mixing with the ambient flow. For the purpose of effectively cooling a large heated surface using impinging jets, multiple jets arranged in certain pattern can be used to cover a large part of the target surface and elevate the overall heat transfer rate for the surface. The impinging jets, circular or of other shapes, can be ordered in a line, a square array, or a staggered array. For single jet impingement, the heat transfer characteristics are determined by the jet velocity, jet hydraulic diameter, jet-to-plate spacing, jet impinging angle, and the magnitude of cross flow. For multiple jet impingement, besides all the parameters above, the jet-to-jet spacing also affects the overall heat transfer.

Gardon and Akfirat (1966) first examined the heat transfer of 2 and 3 slot jets arranged in a row impinging on an isothermal plate. They concluded that the smaller jet-to-jet spacing increased the interaction between the adjacent jets and decreased the heat transfer coefficients. Kercher and Tabakoff (1970) studied cooling using a square array of circular air jets perpendicularly impinging on a heated surface with the spent air forming a cross flow interacting with the jets. Their correlation accounted the relevant parameters and was represented in a form similar to single jet impingement heat transfer. They concluded that the heat transfer was dominated by the jet Reynolds number and jet-to-jet spacing and the cross flow resulting from the spent air decreased the heat transfer coefficients. Metzger, *et al.* (1979) and Behbahani, *et al.* (1983) studied heat transfer characteristics for both inline and staggered jets and found that the inline pattern had higher heat transfer coefficients than the staggered pattern. Goldstein and Seol (1991) experimentally investigated heat transfer between a row of impinging jets and a heated flat plate and periodic variation of local heat transfer coefficients was observed with the maximum values occurring in the vicinity of the impingement zone.

The heat transfer characteristic resulting from the interaction between adjacent jets can be related to the flow structure. Saripalli (1983) visualized multiple jet impingement flow using a fluorescent technique, examining the effect of the variation of jet-to-jet spacing on the flow field (Figure 2-6). At small spacing, the adjacent jets interfere with each other before impingement and this interference causes the jet to decelerate, thus decreasing heat transfer of the jet array. A fountain (Figure 2-6) can be formed if the jets are strong and affects the heat transfer due the recirculation and entrainment of spent fluid (San and Lai, 2001).

San and Lai (2001) studied the quantitative effect of jet-to-jet spacing on the heat transfer of a staggered jet array of five jets impinging on a flat plate of constant surface heat flux to identify the optimum jet-to-jet spacing for maximum heat transfer. They reported the stagnation Nusselt number as functions of jet-to-jet spacing, nozzle-to-plate spacing, and jet Reynolds number. Figure 2-7 plotted the Nusselt number for a case in which the dimensionless jet-to-plate spacing was 2.0. For this case, it clearly showed that certain jet-to-jet spacing produced maximized heat transfer coefficients. When the jet-to-jet spacing increased from a very small value, the jet fountain diminished and the heat transfer coefficient increased. While at a large jet-to-jet spacing, the heat transfer coefficient dropped because of the increasing heated area to be cooled. It was also clear that the optimal jet-to-jet spacing when the maximum Nu occurred was the same for all Reynolds numbers. When varying jet-to-plate spacing, different values of optimum jet-to-jet spacing occurred (San and Lai, 2001).

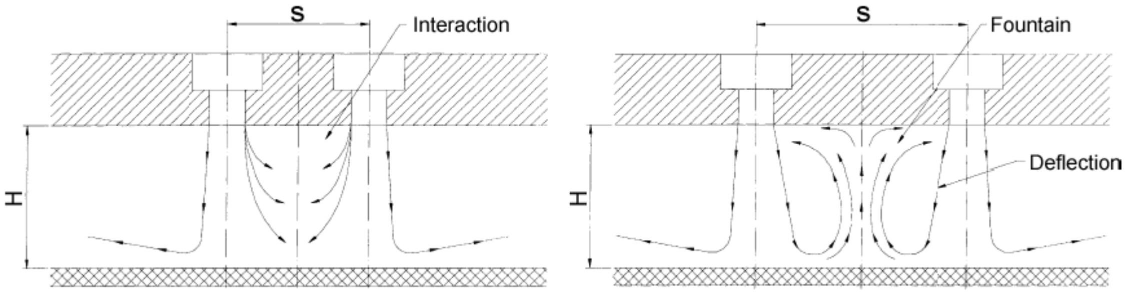

Figure 2-6 Jet interaction between two adjacent jets (San and Lai, 2001)
(Left: interference; Right: fountain forming)

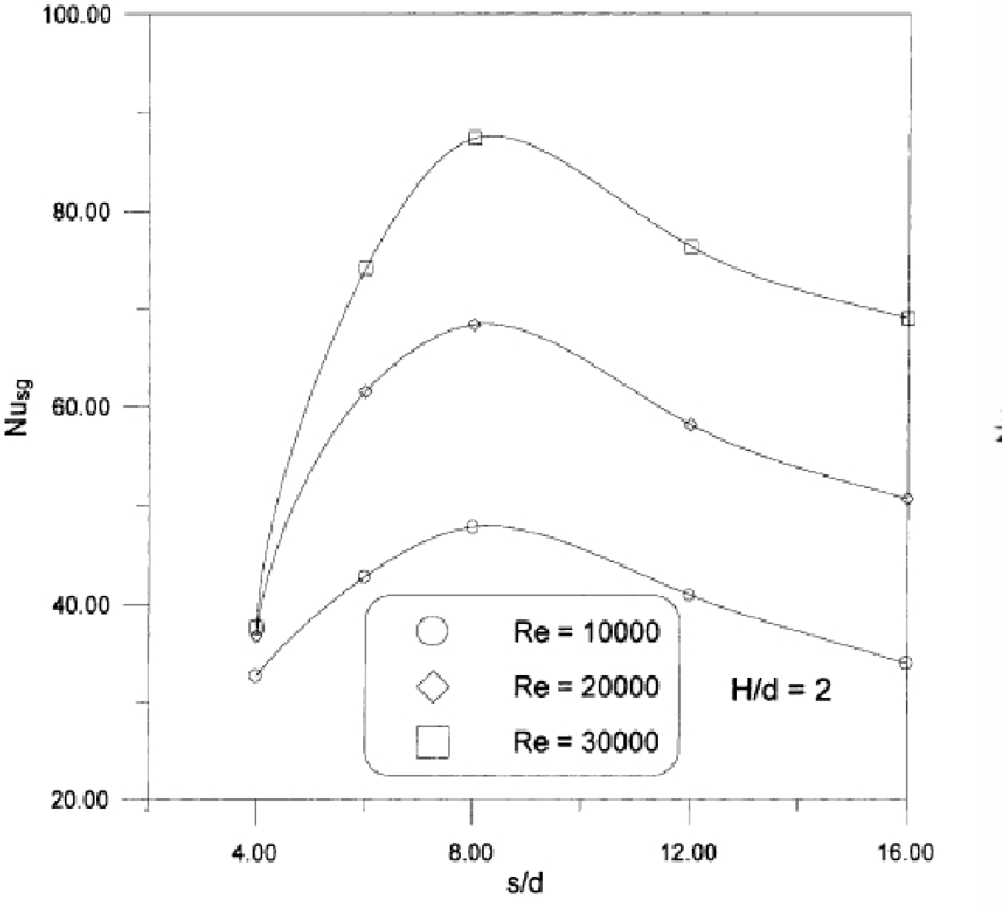

Figure 2-7 Effect of Re and jet-to-jet spacing on stagnation Nu (San and Lai, 2001)

Huber and Viskanta (1994) measured the local heat transfer data for a confined 3×3 square array of isothermal air jets impinging normally to a heated surface with spent air exits located between the adjacent jets and discovered that lower jet-to-surface spacing enhanced the uniformity of heat transfer coefficients. Dano, Liburdy and Kanokjaruvijit (2005) investigated flow structure and heat transfer characteristics of a 7×7 square array of jets impinging on surfaces of isothermal condition or uniform heat flux with the exhaust discharge acting as a cross flow and concluded the cross flow influenced the heat transfer results due to the interaction with jet impingement. San, Tsou and Chen (2007) extended San and Lai's studies by including the effect of the width of and length of the jet plate and found the Nusselt numbers were strongly dependent on the width but only weakly on the length.

2.3.2 Numerical studies of impinging jets

Various numerical studies have been performed to model a single jet or an array of jets, being laminar or turbulent, which impinge on a heated surface for heat transfer enhancement. Al-Sanea (1992) performed a numerical study to model a laminar impinging slot-jet using a control-volume finite-difference method and found the results agreed well with the experiments in the literature. They also included the effect of cross flow on the heat transfer and concluded that the presence of a cross flow degraded the heat transfer capability of a laminar impinging jet. Another study on a laminar impinging jet was done by Lee, *et al.* (1997) for a circular liquid jet having a large Prandtl number (Pr=337). Their results showed good agreement with the experiments for local Nusselt number and they also reported that the large recovery factor predicted was a result of the large Prandtl number used. Chatterjee and Deviprasath (2001) demonstrated the secondary maxima in heat transfer coefficients in the radial direction for a small nozzle-to-plate distance for a laminar jet impinging normally on a heated surface. They argued that the phenomena were solely determined by the upstream flow development due to vorticity diffusion.

For turbulent jet modeling, the well-established k-ε turbulence models were predominantly applied to capture the flow structure and heat transfer characteristics.

El-Gabry and Kaminski (2005) used the standard *k-ε* turbulence model to predict the heat transfer characteristics of an array of angled jets impinging on a smooth heated surface. They compared the results using the *k-ε* model to those using the Yang-Shih model and concluded that these models were able to predict the local and average heat transfer coefficients reasonably well. Salamah and Kaminski (2005) applied the low-Re *k-ε* model for an array of jets impinging on a stationary surface and found reasonably good agreement with the experiments. They found the heat transfer coefficients were maximal at the stagnation point and decayed away from the jet impingement point. Local off-center secondary maxima between two jets were also successfully predicted, which were a consequence of jet-jet interaction.

To address the three-dimensional flow field in a inclined jet impingement problem, Yang and Wang (2005) performed a three-dimensional numerical simulation of fluid flow and heat transfer for an inclined jet impinging on a heated plate with the cross-flow effect included (velocity ratio of 3-7). They used the standard *k-ε* turbulence model and wall function for turbulence modeling and the predictions were validated with the available experimental data. Souris, Liakos and Founti (2004) modeled Choi, *et al.* (2000)'s experiments for a slot jet impinging on a concave surface. They also applied the *k-ε* model together with the Reynolds stress model and concluded that the models were appropriate for the heat transfer enhancement study in impinging jets.

CHAPTER 3

EXPERIMENTAL APPARATUS AND PROCEDURES

3.1 Introduction

The purpose of this dissertation is to quantitatively characterize the cooling effectiveness of near-wall jets for heated thin metal foils experimentally and numerically. As part of the experimental studies, a bench-top experimental apparatus was designed and constructed with the capability of employing both planar tangential and circular impinging jet configurations for both flat and scalloped foil designs (Figure 3-1). For both foil designs, the apparatus allows variation and control of jet diameter, jet flow rate, orientation of the jet, jet-to-foil spacing and jet impingement locations on the foil. These variations in the experimental parameters help identify the optimal configuration, based on the convective heat transfer characteristics obtained from the experiments. Detailed experimental measurements included foil temperature using thermocouples and an infrared thermography camera, jet temperature using thermocouples, pressures using transducers, and flow velocity using an anemometer. This chapter provides a detailed description of the apparatus components and experimental procedures used in this investigation.

3.2 Flow Channel

To simulate the continuous laser gas flow in Electra, a rectangular channel was built from Plexiglas, which is transparent and easy to machine. The vertically-installed channel had a height of ~1.0 m and a square cross section of ~12.0 cm on each side. Two axial fans (Fulltech UF-12A12-L) were installed at the entrance and the exit of the channel to drive a steady flow in the channel. The characteristic curve of the fan is shown in Figure 3-2. With both fans turned on, the average bulk velocity through the channel was ~4.0 m/s. The channel also housed the foil fixture (~40 cm high) that was bolted to the mid-section of the channel.

3.3 Foil Fixture

A foil fixture was designed and constructed to hold the foil strip whose shape represented the actual geometry between two hibachi support ribs in the electron beam pumped gas laser's hibachi structure. Because the foil had a large aspect ratio (~9.0) and the change in the length of the foil due to thermal expansion was significant, a special spring tensioning mechanism was devised to keep the foil shape constant for both the flat and scalloped foil designs (Figure 3-3).

For the flat foil design, two round copper rods were used to both conduct electricity to ohmically heat the foil and to stretch the foil, aided by an external spring. The bottom rod was fixed and when the foil expanded, the spring-actuated rotation of the top copper rod kept the foil stretched.

Similarly, the scalloped foil design also adopted a spring-tensioning method.

The foil was first clamped to two half-moon-shaped copper electrodes both on the top and bottom. To shape the foil into the scalloped form, the foil is then pressed tightly against a pre-machined insulation block made of type-I Marinite. The electrode on the bottom was fixed, while the other one on the top moved when the foil expanded or shrunk. To guide the movement of the top electrode, two round Garolite rods were installed vertically and parallel to the foil. The movement of the top electrode was produced by two compression springs attached to the rods, which helped stretch the foil to form the desired scalloped shape. The thermal insulation block behind the foil was machined to form a concave surface representing the desired foil shape between the two hibachi ribs (see Figure 3.4 for the shape of the scalloped foil).

3.4 Flow in the Channel

Prior to the experiments with jet injection, the flow over the flat foil was basically external flow over a flat plate and heat transfer characteristics could be well characterized using available external flow heat transfer correlations. To verify the flow condition in the channel, forced convection heat transfer experiments were performed. The comparison of experimental and calculated heat transfer coefficients showed good agreement within 10%, which indicated that fully turbulent flow had been established in the channel (Figure 3-5). The plot also shows that the heat transfer coefficients are independent of applied surface heat fluxes, which is expected in forced-convection heat transfer in external flow over a flat surface. The results also show that the instrumentation and data acquisition system are functioning properly.

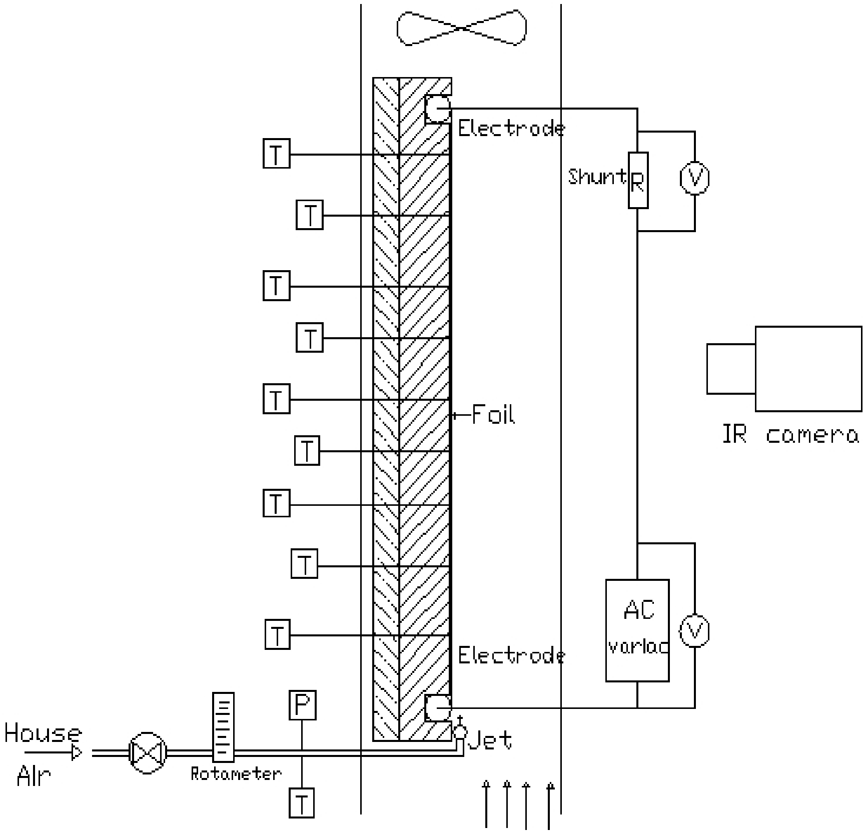

Figure 3-1 Schematic of experimental apparatus for planar jet cooling of a flat foil
(P: pressure transducer; T: thermocouple; R: shunt; V: voltage measurement)

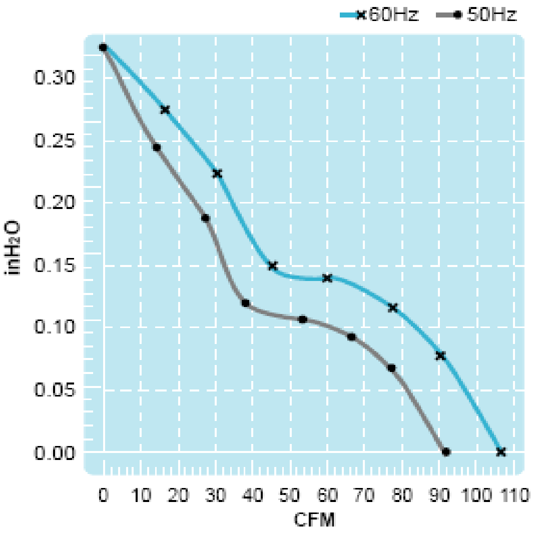

Figure 3-2 Fan characteristic curve (Fulltech UF-12A12-L)

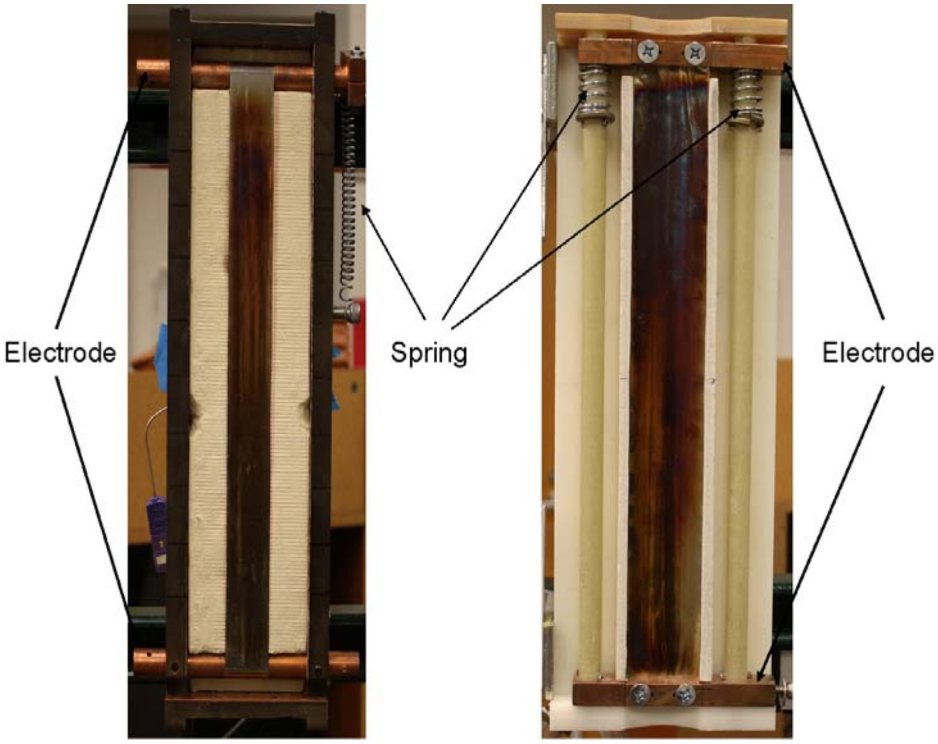

Figure 3-3 Foil fixture for heat transfer experiments
(Left: flat foil; Right: Scalloped foil)

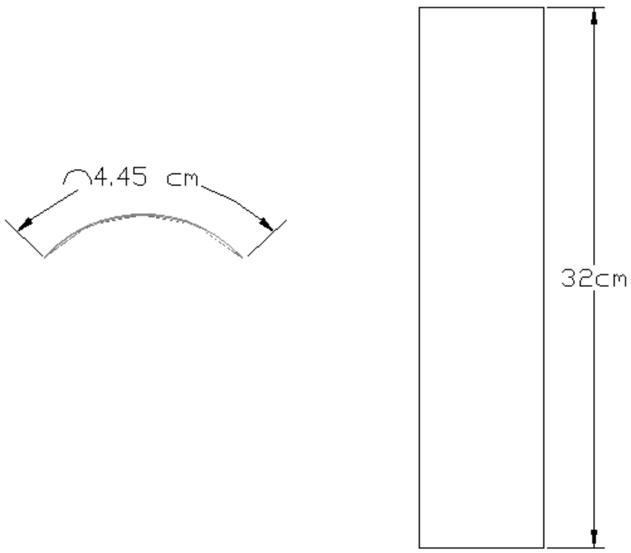

Figure 3-4 Schematic of the scalloped foil used in the heat transfer experiments

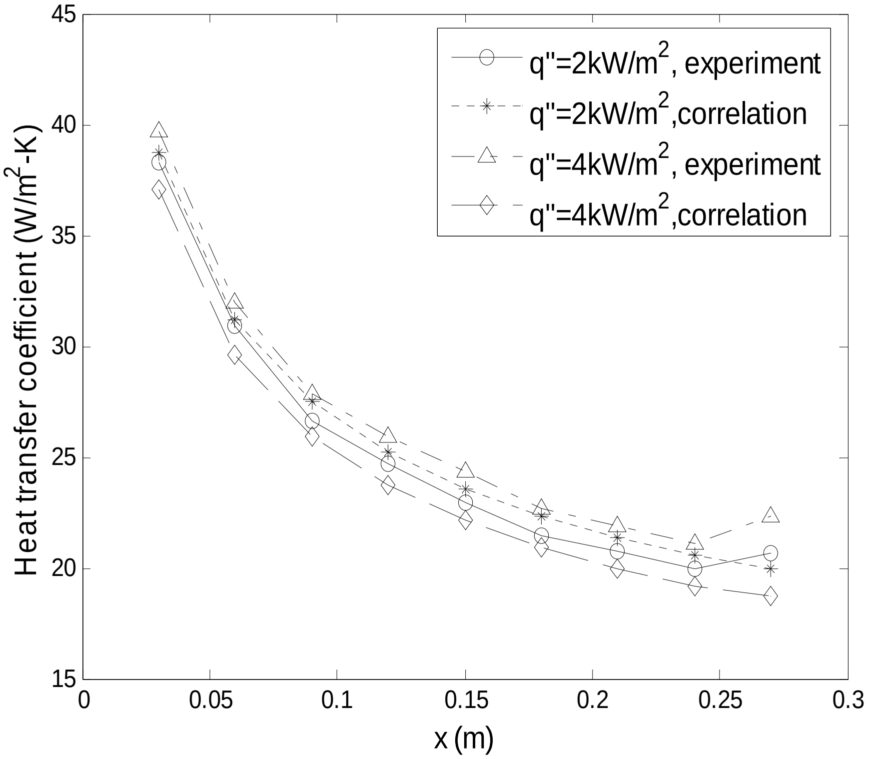

Figure 3-5 Comparison of convection heat transfer coefficient between experiments and correlation results for external flow

3.5 Jet Supply System

In addition to the fan-driven mainstream flow over the ohmically heated thin stainless steel foil, either a planar jet or impinging jets provided additional cooling for the foil in the experiments. The issuing of a jet started with house air first being regulated for depressurization before passing through a needle valve and a gas rotameter for further flow control and flow rate measurement. Air was then supplied to the headers of the jet supply system that was attached to the foil fixture to produce high speed jets, either planar or circular.

3.5.1 Planar jet

A planar jet was formed by forcing air to flow out of a square-edged slot machined into a brass jet tube (40.0 cm long, 1.25 cm OD and 1.0 mm wall thickness). Air was supplied on both ends of the tube through appropriate fittings. The slot was 1.0 mm wide (*W*) and 3.4 cm long (*L*), which was of the same width as the foil strip (Figure 3-6). The orientation of the jet tube was adjusted so that the planar/slab air jet would flow parallel to the foil, starting from the leading edge of the foil strip.

Average jet velocity (U_{avg}) was determined from the measured volumetric flow rate corrected by the operating pressure of the rotameter and the flow area of the jet. The average velocity was used to calculate the slot Reynolds number (Re_s),

$$\mathrm{Re}_s = \frac{\rho U_{avg} s}{\mu} \qquad \text{(Eq. 3-1)}$$

3.5.2 Circular impinging jets

Impinging jets were produced by forcing air through a row of small circular openings on each of two jet tubes that were placed parallel to the two edges of the foil. Each 39.4 cm-long jet tube was made of stainless steel tubing that had an OD of 9.6 mm and wall thickness of 0.5 mm. Circular openings of the desired diameter were carefully drilled, deburred and evenly spaced 1.25 cm apart. The holes were aligned to form a line of jets. Figure 3-7 shows a portion of one jet tube with small openings (1.2 mm diameter). Two jet tubes were used to cool the foil. To provide a better coverage, 51 jets were directed towards the foil, with 25 jets on one side and 26 on the other. These two rows of jets were interlaced so that the effective jet-to-jet spacing was reduced by half (0.63 cm). Several sets of jet tubes were machined with hole diameters ranging from 0.8 mm to 1.6 mm.

Two special rectangular headers were designed to hold the jet tubes on the top and the bottom with ports for air intake (Figure 3-8). The header had a relatively large plenum volume upstream of the jet tubes that served as the reservoir for the tubes. This helped produce a relatively uniform distribution of air velocity issuing from the jet holes.

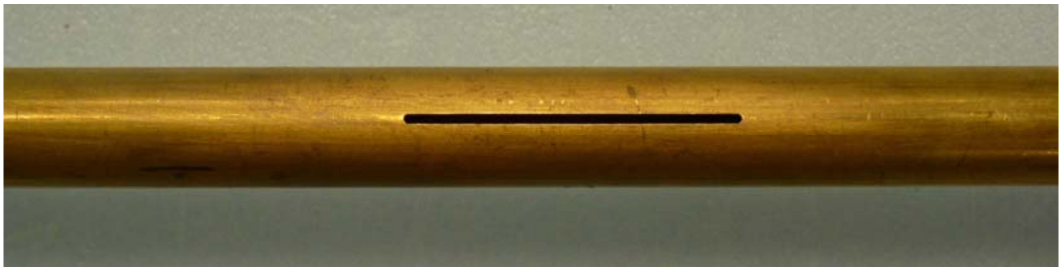

Figure 3-6 Planar jet tube

Figure 3-7 Jet tube for impinging jet issuing

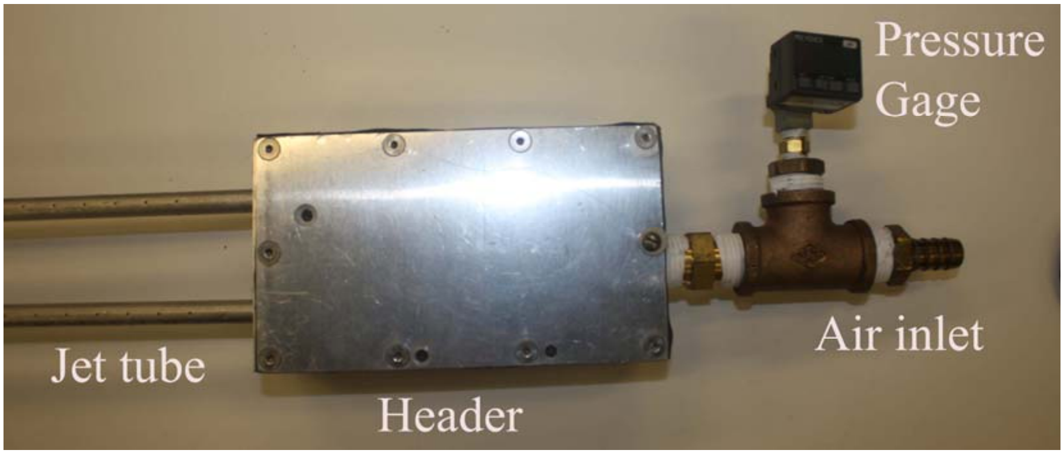

Figure 3-8 Jet tube and an attached header

Figure 3-9 shows a picture of the impinging jet cooling apparatus for the flat foil. Air enters the jet supply system through two headers and jets are produced by the jet tubes. For the scalloped foil, the only difference was in the foil fixture. The double-inlet setup was used in order to produce a relatively uniform jet velocity distribution. A schematic of jets impinging on a flat foil is shown in Figure 3-10, where the two opposite jets were actually offset vertically by 0.63 cm.

3.6 Foil Heating

The stainless steel foil used in the experiments is the same as that used in Electra and was resistively heated by running an AC current through it. The adjustment of the input power was regulated using a Variac power supply to achieve the desired current, which was measured using a shunt. The actual power input was calculated by first determining the resistance of the foil strip according to the temperature-dependent resistivity data of type-304 stainless steel that was provided by the manufacturer. The tabulated data was fitted into a second-order formula as a function of temperature (Figure 3-11).

The average foil temperature was calculated from the experimental measurements and this value was used to determine the resistivity of the foil. Then the resistance of the foil strip was evaluated by the following equation,

$$R = \rho \frac{L}{S} \qquad \text{(Eq. 3-2)}$$

where ρ is the resistivity, L is the foil length and S is the area of the cross section, respectively. Combined with the measured AC current, I, the input power, P, was simply calculated using the relation, $P=I^2R$. Alternatively, the power input was determined from the measured current and the measured voltage drop between the two electrodes at opposite ends of the foil.

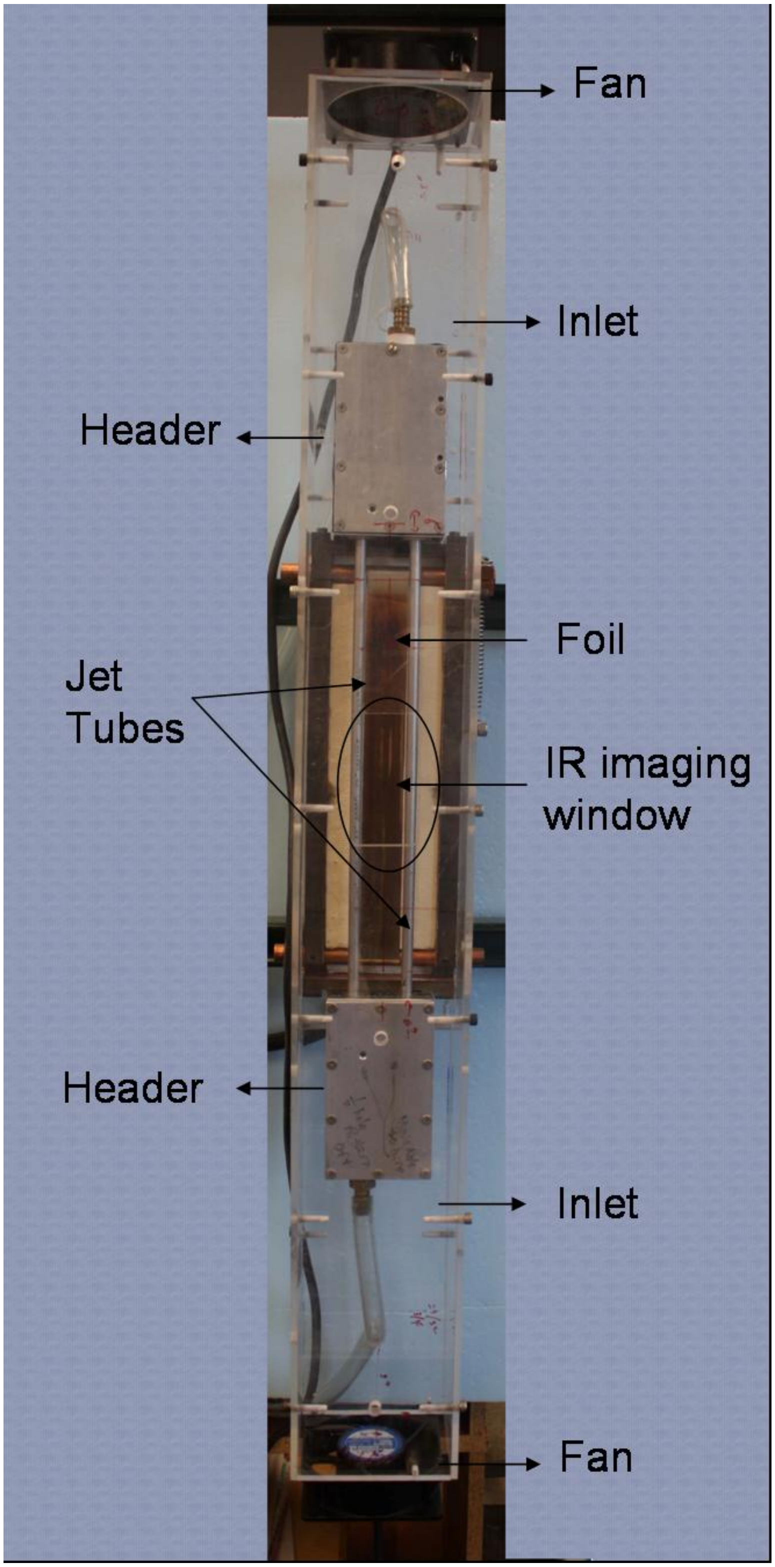

Figure 3-9 Jet cooling setup for the flat foil

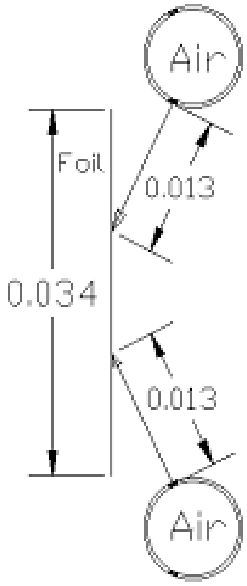

Figure 3-10 Schematic of impinging jet cooling scheme

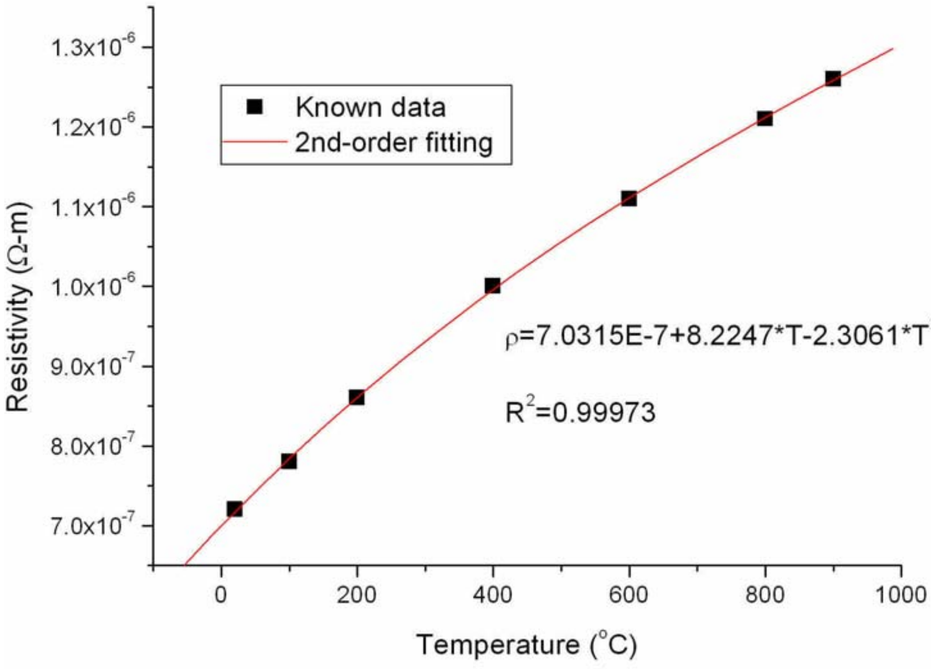

Figure 3-11 Temperature-dependent Resistivity of Type-304 stainless steel

3.7 Experimental Measurement Techniques

Experimental studies involved the measurements of various parameters under different experimental conditions. Measured quantities included AC heating power supplied to the foil, mainstream velocity, the total jet flow rate, and jet and foil temperatures. The heating power was determined by measuring the voltage drop between two electrodes and the current running through the foil strip using an Agilent data acquisition/switch unit (34970A). The total jet flow rate of the parallel planar jet or the 51 impinging jets was measured using a float-type gas rotameter and the average jet exit velocities were evaluated based on the flow rate. The mainstream velocity was measured by a hot-wire anemometer. The air temperature was measured by a type-E thermocouple located at the exit of the rotameter.

For the foil temperature measurement, an infrared (IR) thermography camera was used to provide detailed temperature information over the entire surface of the foil. Additionally, a series of thermocouples attached to the back surface of the foil was used to determine the temperature distribution along the centerline of the flat foil for planar jet cooling experiments. The thermography camera (FLIR PM280) was set to focus at the mid-section of the foil strip that covered about ten impinging jets. The IR thermography imaging technique needed known emissivity values of the foil that were functions of foil temperature. Because the temperature of the foil was not uniform and only one emissivity value could be set on the camera, the relationship between emissivity and temperature was experimentally obtained for the temperature range covering the expected temperature distribution of the foil. For each thermocouple temperature value, emissivity value setting of the camera was adjusted until the camera temperature reading matched the reading from the thermocouple. Figure 3-12 plots the temperature measurements and the corresponding emissivity values used. It was found that the emissivity has an average of 0.31 and standard deviation of 0.04. The average emissivity value of 0.31 was used for all experiments and the uncertainty of emissivity values was accounted for in the error analysis.

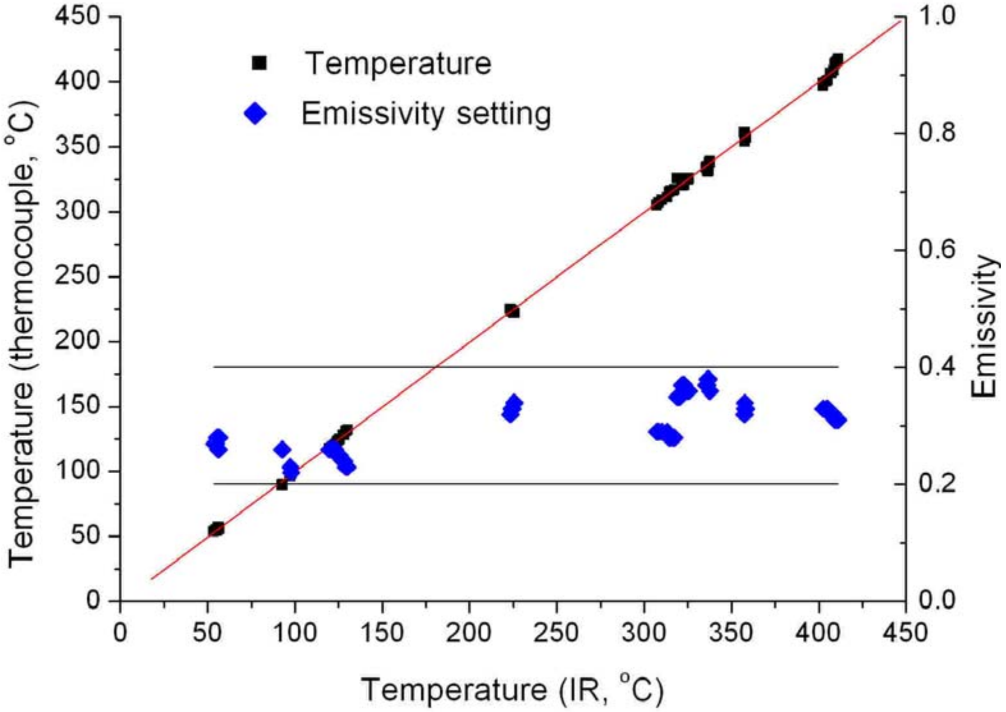

Figure 3-12 Determination of emissivity values for the foil

This process captures the appropriate range of emissivity values to assure that IR temperature measurement matches the actual thermocouple measurement. Observed changes in "measured" emissivity do not only represent actual physical changes in emissivity of the foil. Instead they convey the random fluctuation in the measured temperature by the IR camera.

3.8 Data and Error Analysis

Heat transfer coefficients and Nusselt numbers based on the jet diameter (D) were calculated using the following equations,

$$h = \frac{q"}{T_f - T_j} \qquad \text{(Eq. 3-3)}$$

$$Nu_d = \frac{hd}{k} \qquad \text{(Eq. 3-4)}$$

Computing the heat transfer coefficients and Nusselt numbers required the determination of the surface heat flux removed by convection heat transfer. Although the thin stainless steel foil was efficiently insulated on its backside, it was necessary to account for conduction heat losses through the insulation block and thermal radiation heat losses to the environment through the thermography imaging optical access window particularly at elevated temperatures. These two terms were subtracted from the electric heating power to determine the net convection heat flux.

In addition to the heat transfer coefficients and Nusselt numbers, other important parameters including jet Reynolds numbers (Re_d), jet-foil spacing (L) and jet impingement angles (Φ) were taken into account to fully characterize the heat transfer characteristics associated with the planar jet or impinging jets.

Detailed error analysis has been conducted and is summarized in Appendix A. The uncertainty in Jet flow rate measurement is estimated to be less than 3%. The uncertainty in foil temperature measurement using the infrared thermography camera is less than 5%, which accounts for the dependence of emissivity on temperature. Jet velocity distribution has a relatively large uncertainty of about 20%. The uncertainties in heat transfer coefficients and Nusselt numbers are calculated using error propagation formula and estimated to about 5% and 6%, respectively.

3.9 Experimental Procedures

To investigate the heat transfer enhancement of applying near-wall jets to the foil subjected to relatively high heat fluxes, the procedures for each experiment were as follows,

1. Install the foil strip.
2. Install the jet supply system at the desired spacing and impingement angle.
3. Connect electric heating circuit.
4. Turn on the fans to drive the main stream flow past the foil.
5. Adjust the heating power to the desired value.
6. Issue jets towards the foil.
7. Measure various experimental parameters after the foil temperature reaches steady state.
8. Turn off the heating power.

During each experiment, the control valve at the inlet of the gas rotameter was periodically adjusted to compensate for any fluctuation in house air supply so that the jet flow rate remained relatively constant while the foil temperature reached steady state.

CHAPTER 4

PLANAR JET COOLING OF A HEATED FLAT FOIL

4.1 Introduction

This chapter presents both of the experimental and CFD results obtained from forced convection cooling for a heated flat foil using a near-wall high-speed planar jet. Various jet velocities and heat fluxes were examined. Experimental data were correlated into similar empirical forms as suggested in the literature. The experimental results were also compared to the predictions from two-dimensional CFD simulations using FLUENT®.

4.2 Experimental Studies of Planar Jet Cooling

4.2.1 Summary of experimental results

To investigate the cooling performance of a planar jet that is injected at the leading edge of a heated foil, tests were run at various jet flow rates/velocities and surface heat fluxes. In addition to the mainstream flow field at ~4.0 m/s created by the fans, the planar jet (s=1.0 mm, W=34.0 mm) enhances heat transfer thereby reducing the foil temperatures. The foil temperatures are measured by a row of nine evenly-spaced (3.0 cm apart) thermocouples that are glued to the back of the foil along the centerline of the foil. Experimental parameters used in the various experiments are summarized in Table 4-1.

Heat transfer enhancement as a result of the plane jet injection was examined through a comparison between experimental measurements when the jet was on and those when the jet was off. To accurately determine the convection heat flux transferred to the coolant, heat losses from the foil due to thermal radiation to the atmosphere and heat conduction from the back surface of the foil to the thermal insulation block were taken into account. The amount of heat loss was found to be small because relatively low heat fluxes were used in the experiments, thereby reducing the foil temperature. Figure 4-1 and Figure 4-2 show the foil temperature profiles and corresponding heat transfer coefficient profiles respectively along the centerline of the foil for a surface heat flux of 2.0 kW/m^2.

Table 4-1 Experimental parameters for the planar jet cooling experiments

Bulk flow velocity (m/s)	Jet velocity (m/s)	Surface heat flux (kW/m^2)
4.0	0	2.0
4.0	0	4.0
4.0	25.0	2.0
4.0	25.0	4.0
4.0	50.0	2.0
4.0	50.0	4.0

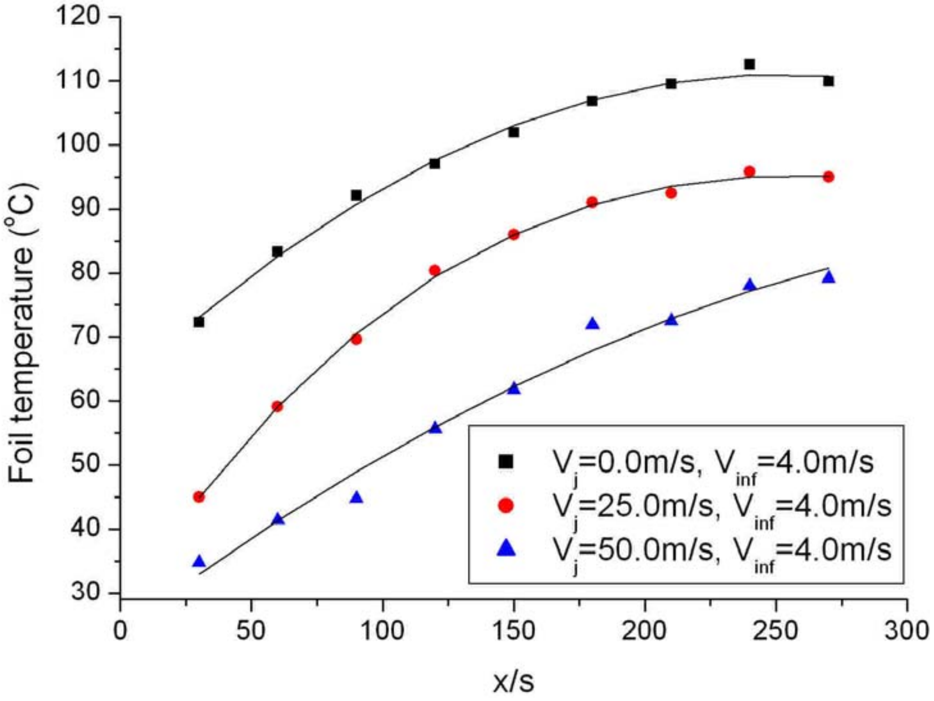

Figure 4-1 Foil temperature profile for various jet velocities (q”= 2.0 kW/m^2)

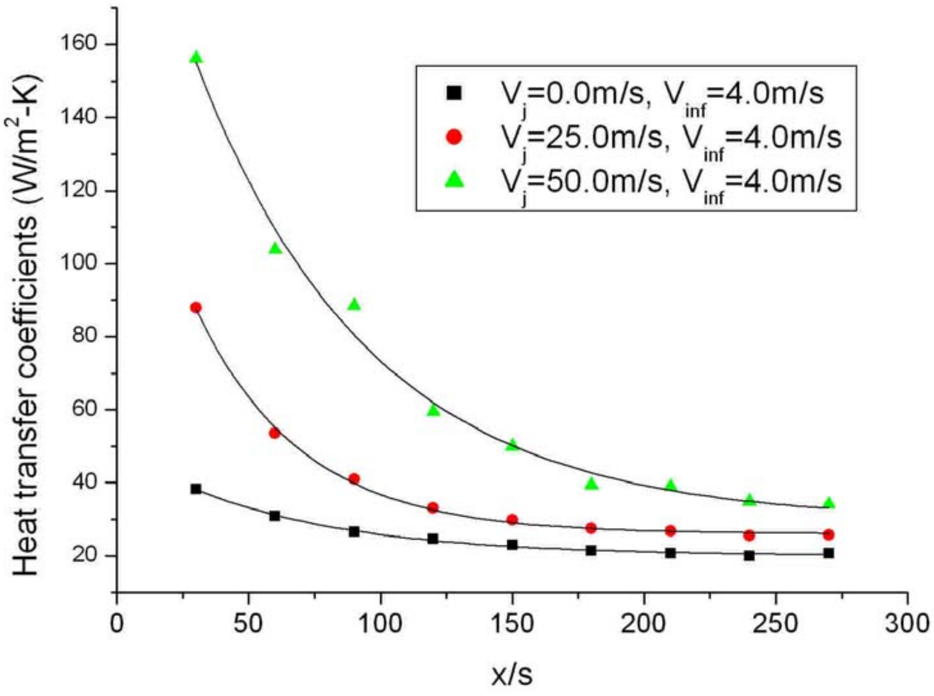

Figure 4-2 Heat transfer coefficient profile for various jet velocities (q”=2.0 kW/m^2)

The results shown in Figure 4-1 and Figure 4-2 indicate that near the leading edge, the heat transfer coefficient for the jet at 50.0 m/s is about twice the value for the jet at 25.0 m/s and four times the value when only the main stream flow of ~4.0 m/s is present and the jet is turned off. Injection of the planar jet decreases the thickness of the thermal boundary layer and thus increases the heat transfer rate from the foil to the main stream. The heat transfer coefficient plot also indicates quickly decaying values downstream from the injection point, which results in much higher foil temperatures in the upper portion of the foil than in the lower portion when a constant surface heat flux is applied. The degradation in the local heat transfer coefficient arises as the jet mixes with the main stream and the boundary layer thickness increases.

The heat transfer enhancement produced by the near-wall planar jet is plotted in Figure 4-3, where the ratio of heat transfer coefficients with the jet turned on to those with the jet turned off is shown as a function of non-dimensional downstream distances for a heat flux of 4.0 kW/m^2. The loss in the jet's momentum as it mixes with the main stream causes the heat transfer enhancement ratio to decrease quickly. For the jet velocity of 50.0 m/s, a ratio greater than 4.2 was obtained at the leading edge of the foil, while the value drops to less than 1.6 near the end of the foil length; for a jet speed of 25.0 m/s, the ratio drops from ~2.5 to ~1.2. The plot also indicates that at a higher jet velocity, the rate at which the decaying of the heat transfer enhancement ratio decreases downstream from the injection point is much faster.

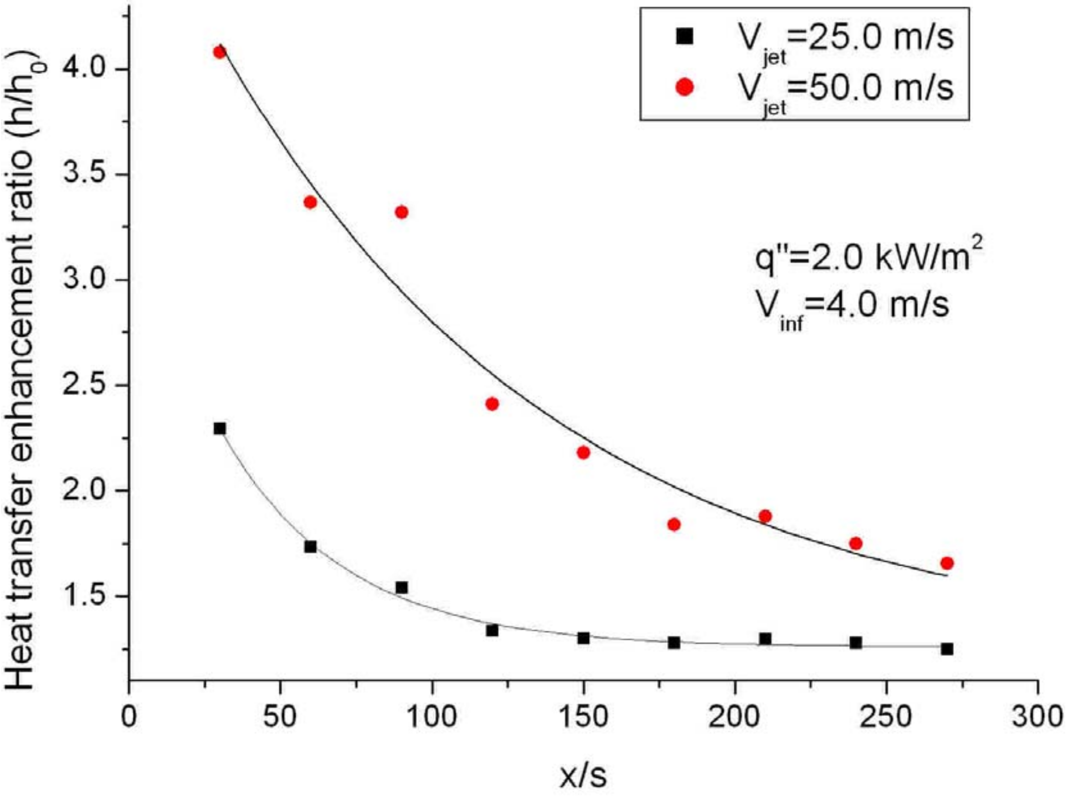

Figure 4-3 Heat transfer enhancement ratio using a near-wall planar jet

Further examination of the experimental results reveals that a higher jet flow rate provides better heat transfer enhancement for the foil. However, higher flow rate demands larger pumping power, which adversely affects the overall efficiency of the gas laser system. Figure 4-4 shows the pressure drop between the outlet of the rotameter and the jet exit, which accounts for the pressure drop in the piping and the planar jet supply system. As expected, the plot shows a nearly second-order growth rate in the pressure drop with increasing jet velocities or jet flow rate.

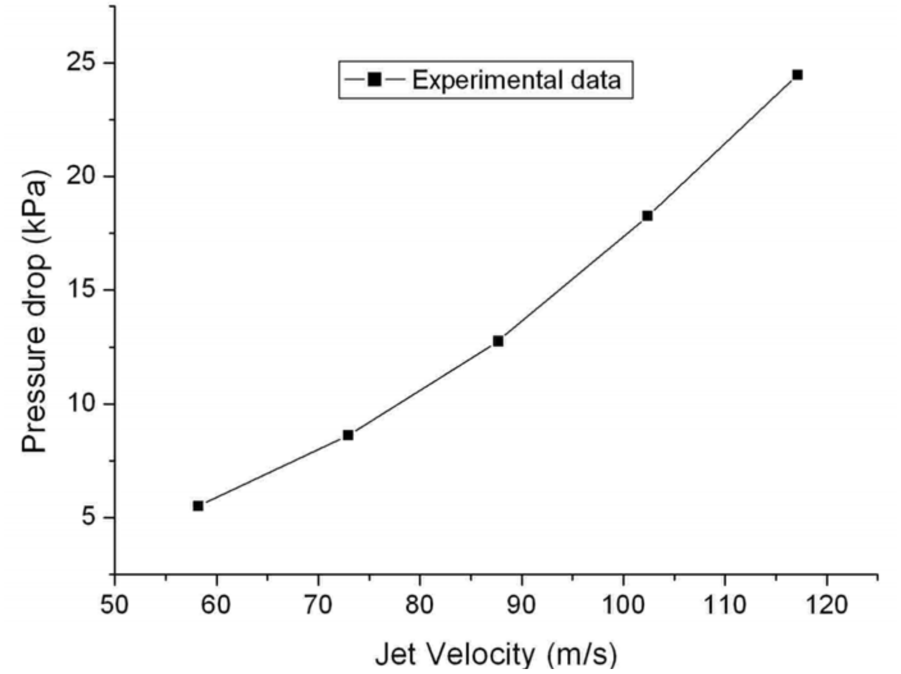

Figure 4-4 Pressure drop between the rotameter and jet exit for various jet velocities

The experimental results also show that with only one planar jet injection point, the foil does not cool down as uniformly as desired. The inefficiency of cooling could be alleviated by adding more injection points downstream from the first point (Goldstein, 1977). However, this method is not feasible for current gas laser systems because it will partially block the pathway of the electron beams and decrease the quality of the laser beam, which consequently compromises the focal profile and efficiency of the laser.

4.2.2 Effect of surface heat flux on heat transfer coefficients

For the single-phase forced external flow without near-wall jet injection, the heat transfer coefficients are independent of the applied surface heat flux. In the current experimental investigations, different surface heat fluxes were applied to check if the heat transfer coefficients were still independent of heat flux when a near-wall jet was used. Figure 4-5, which plots the computed heat transfer coefficients at different surface heat fluxes (2.0 and 4.0 kW/m^2), shows that the heat transfer coefficients are also nearly independent of surface heat fluxes when near-wall jets are added.

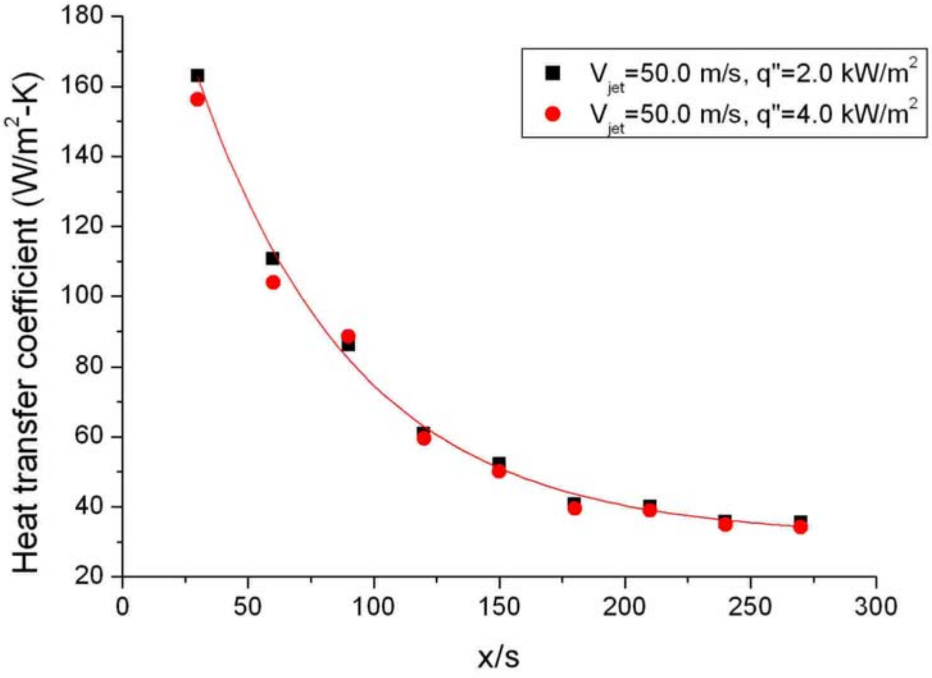

Figure 4-5 Effect of surface heat fluxes on the heat transfer coefficients

4.2.3 Comparison of experimental results with the literature

The experimental results shown in the previous sections presented a consistent trend in the heat transfer coefficients, which indicated that an empirical correlation could be obtained through curve fitting. Lefebvre (1999) introduced a formula for calculating Nusselt numbers as a function of the slot Reynolds number and the normalized distance downstream of the injection slot for film cooling applications. In his correlation, the Nusselt number was based on the downstream distance (x) from the injection point, so the value of Nusselt numbers would increase with the distance despite the decreasing local heat transfer coefficients. To directly show the degrading heat transfer capability in the jet cooling, the definition of Nusselt number was modified to be based on the width of the jet slot; the correlation of Lefebvre was then modified to the following form,

$$Nu_s = C \cdot Re_s^{\alpha} \left(\frac{x}{s} \right)^{\beta} \qquad \text{(Eq. 4-1)}$$

where

$$Nu_s = \frac{hs}{k} \qquad \text{(Eq. 4-2)}$$

$$Re_s = \frac{\rho_{jet} V_{jet} s}{\mu} \qquad \text{(Eq. 4-3)}$$

The constants were determined empirically and different sets of constants were obtained when the blowing ratio (m) varied, which was defined as follows,

$$m = \frac{\rho_{jet} V_{jet}}{\rho_{\infty} V_{\infty}} \qquad \text{(Eq. 4-4)}$$

The constants in the correlation (Eq. 4-1) suggested by Lefebvre (1999) and its parameter range of validity are summarized in Tables 4-2 and 4-3, respectively.

Table 4-2 Constants used in Lefebvre's formula

	$0.5<m<1.3$	$m>1.3$
C	0.069	0.10
α	0.7	0.8
β	-0.3	-0.56

Table 4-3 Parameter range of Lefebvre's correlation

Parameter	Range
m	0.5 - 4.0
ρ_{jet}/ρ_∞	0.8 – 2.5
s	1.9 – 6.4 mm
x/s	0 - 150

Experimental data obtained from the current investigation were based on the experimental parameters beyond those covered by Lefebvre's correlation. The heat transfer characteristic at higher blowing ratios, smaller slot widths, and larger downstream distances were explored. However, it was expected that a correlation with a similar form would exist albeit with different constants. To derive the correlation for the current data, the linear least squares fitting technique was applied after first transforming the data logarithmically. The obtained correlation was as follows.

$$Nu_s = 0.1682 Re_s^{0.7395} \left({}^{x}\!/\!{}_{s} \right)^{-0.7112} \qquad \text{(Eq. 4-5)}$$

This correlation was valid for the experimental parameter ranges summarized in Table 4-4. Figure 4-6 shows the comparison between the correlation and the experimental data, where the correlation was shown to match the data within ±15% for the ranges of parameters used. Different correlation parameters from Lefebvre's correlation were obtained because the study encompassed a very different range of experimental parameters, well beyond those covered by Lefebvre's correlation. A comparison of the current correlation and Lefebvre's correlation under the same experimental conditions also produces some interesting results, especially for the experimental parameters used in the current study. In Figures 4-7 and 4-8, slot Reynolds numbers of 1623 and 3276 were used to compute the corresponding Nusselt numbers using the above two correlations. For these cases, calculations showed Lefebvre's correlation predicted Nu numbers 65% and 71% higher than the current correlation. The difference is due to the fact that the two correlations were based on two very different experimental parameter ranges (slot width, Reynolds number, and blow ratio), resulting in very different coefficients in the correlations.

Table 4-4 Summary of the parameter range for correlation given by Eq. 4-5

Parameter	Range
m	6.25 - 12.5
Re_s	1600 - 3200
x/s	30 - 270
ρ_{jet}/ρ_∞	~ 1.0

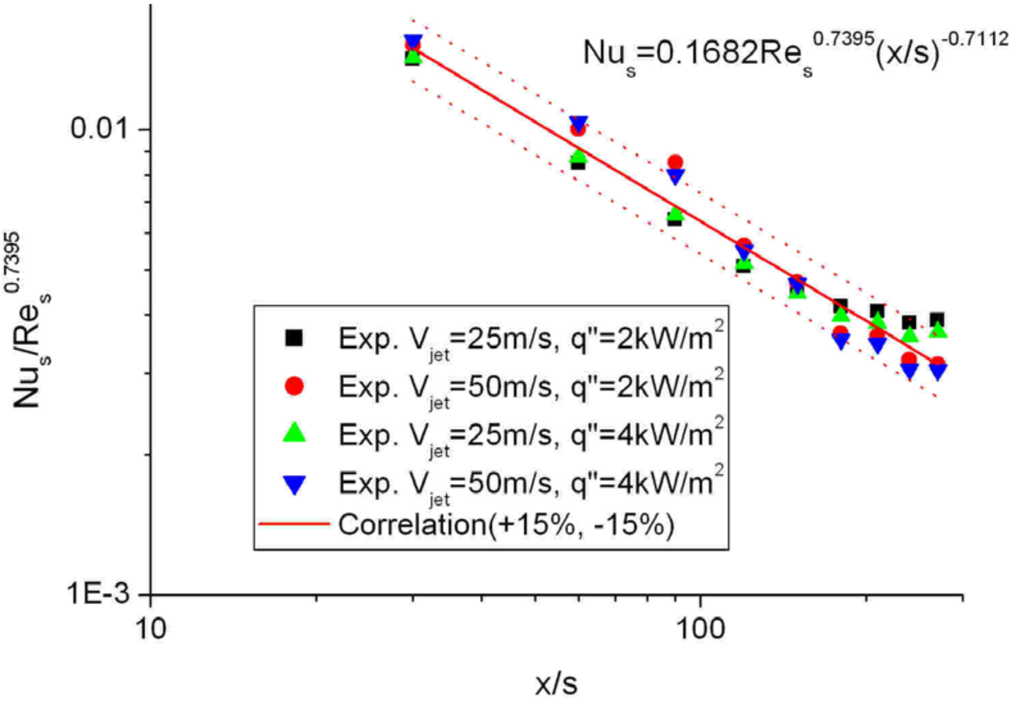

Figure 4-6 Nusselt number correlation for planar jet cooling

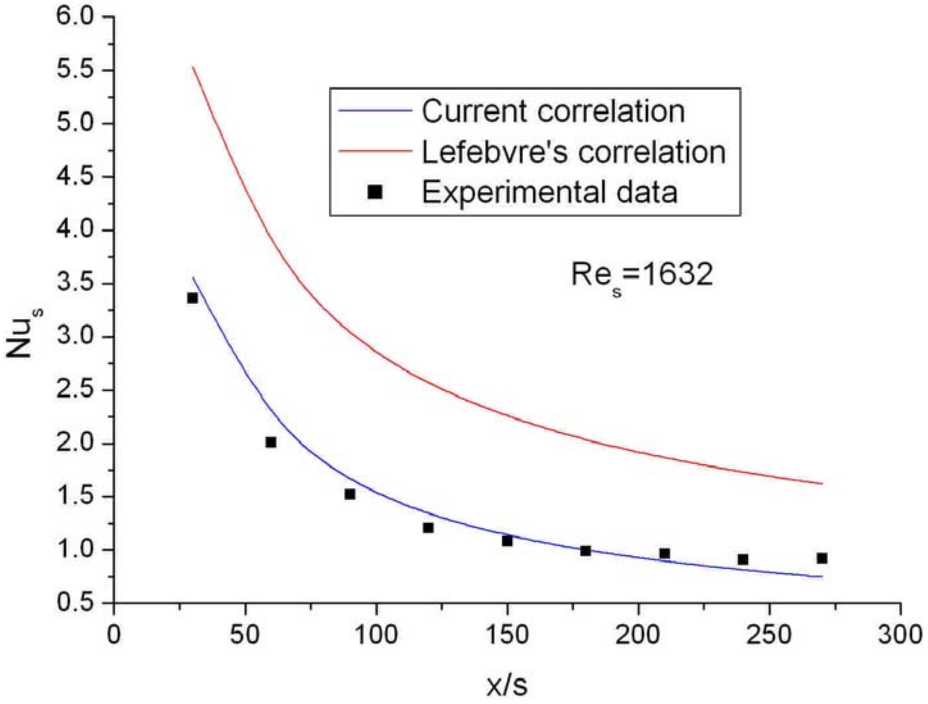

Figure 4-7 Comparison of the Nusselt numbers obtained using Eq. 4-1 and Eq. 4-5 (Re_s=1632)

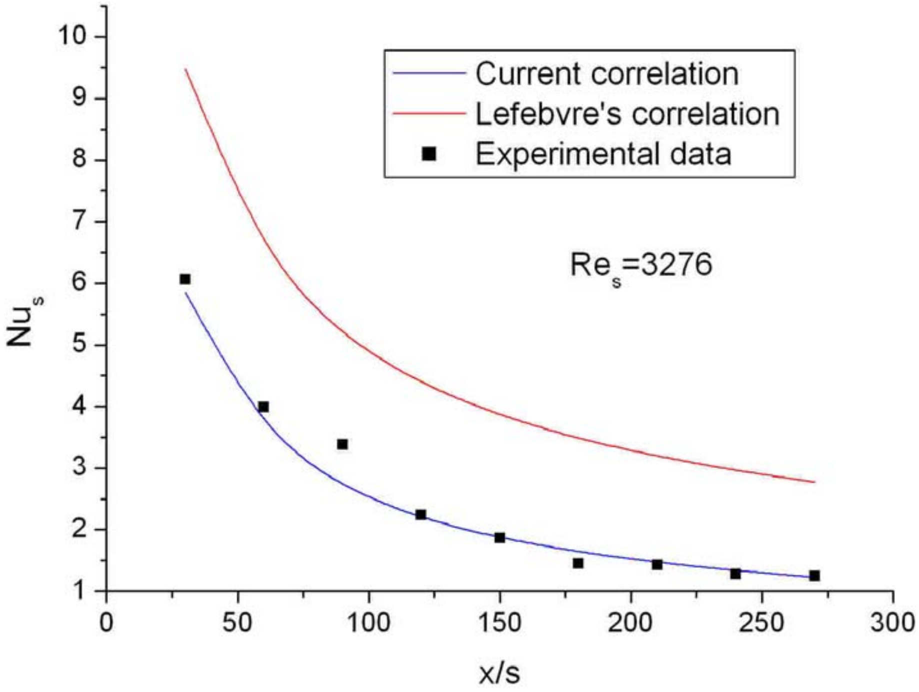

Figure 4-8 Comparison of the Nusselt numbers obtained using Eq. 4-1 and Eq. 4-5 (Re_s=3276)

4.3 CFD Studies of Planar Jet Cooling

4.3.1 Model description and simulation parameters

CFD simulations were performed using the commercial CFD code package, FLUENT®, to predict the fluid mechanics and heat transfer behaviors of planar near-wall jets. The model neglected the lateral temperature variation along the foil width because of the large aspect ratio of both the planar jet and the foil strip, so a simplified two-dimensional grid was proposed and created in GAMBIT®. As shown in Figure 4-9, the flat foil was modeled as a rigid wall of the same length as the actual foil with a thermal insulation block attached to the back. The foil was cooled by the combined convection heat transfer from both the main stream flow at a low speed and the planar jet at a much higher speed, both of which were enclosed in a rectangular area serving as the modeling boundary of the flow field.

In all simulations, boundary conditions were set appropriately to the previously known or experimentally measured values. The volumetric heat generation rate within the foil was specified based on the measured electric power input. Mass flow rate inlet boundary conditions were used for the jet inflow according to the measured flow rate. Other boundary conditions, such as the inlet and outlet of the main stream flow, were set as regular pressure inlet and outlet conditions accordingly. For the surfaces in contact with the ambient, a low convection heat transfer coefficient (~5.0 W/m^2-K) was set to accommodate the natural convection heat transfer to the environment. The meshing of the model incorporated a gradually changing scheme, in which very fine meshes were created near the foil to increase the resolution of the boundary layer, while relatively coarse meshes were applied to the bulk flow to increase the simulation speed. The model employed 160,000 rectangular cells.

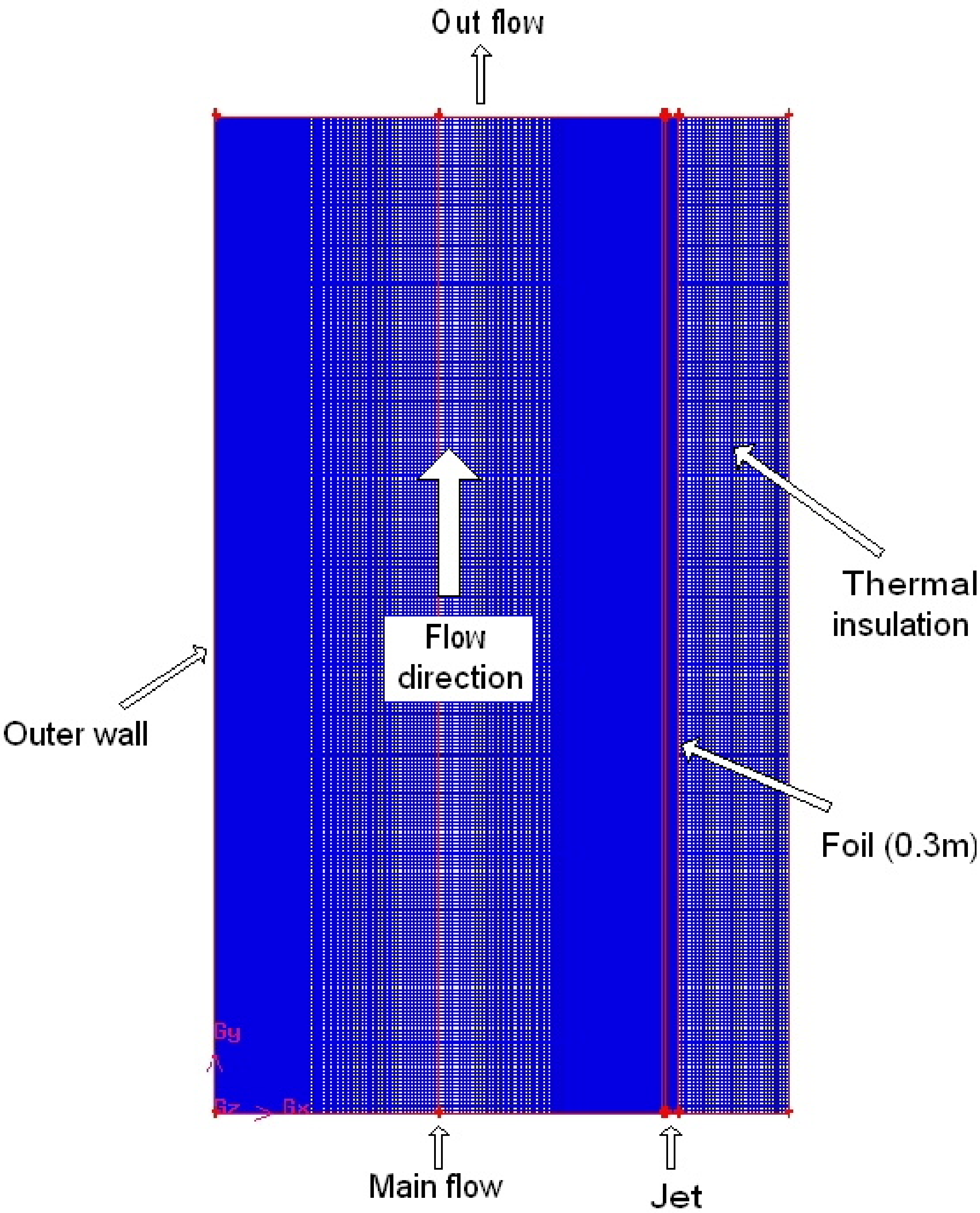

Figure 4-9 FLUENT model for planar jet cooling simulations

Besides setting appropriate boundary conditions, it was also very crucial to apply suitable viscous models for the modeling of turbulence. Steady-state simulations performed in this study adopted both standard and RNG k-ε turbulence models. The RNG k-ε model provides a special formula for the effective viscosity that accounts for low-Reynolds-number effect, which is expected to be suitable for the current study since the jet Reynolds numbers were relatively low (1600 to 3200). The results were compared to those using the standard k-ε model, which is a high-Reynolds-number model. The simulations used the standard wall function for both models and kept the suggested model constants. The simulations ran until the residuals of the continuity equation, the momentum equations and the energy equation decreased below the preset values (1E-3 for the continuity and momentum equations, 1E-6 for the energy equation). The results provided detailed information about both the temperature and flow field distribution, in which the calculated heat transfer coefficients were compared to the experimental results. The numerical results were in good agreement with the experimental measurements and could be used to provide detailed information about the evolution of the jet along the flow direction.

4.3.2 Comparison of simulation results with experimental data

The measured foil temperature and heat transfer coefficients were compared to the CFD predictions for a case with the heat flux set at 2.0 kW/m^2 and the jet velocity at 25.0 m/s. Figure 4-10 compares the foil temperature profile for the experiment and the simulation; good agreement is observed. The standard k-ε turbulence model performed slightly better than the RNG model. Figure 4-11 provides a comparison between the surface heat transfer coefficients obtained in the experiment and the simulation. Both figures showed that for the first half length of the foil, the CFD predictions were very close to the experimental results for both turbulence models, but the difference increased when the jet flow proceeded to the top of the foil and mixed with the free stream.

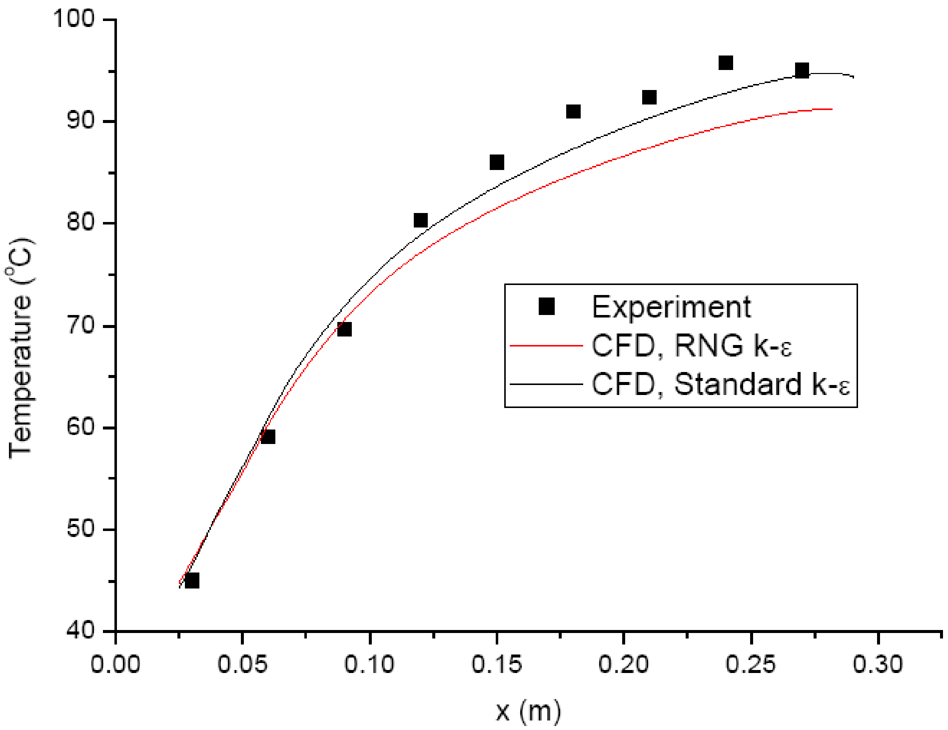

Figure 4-10 Comparison of foil temperature of the experiment and CFD simulations

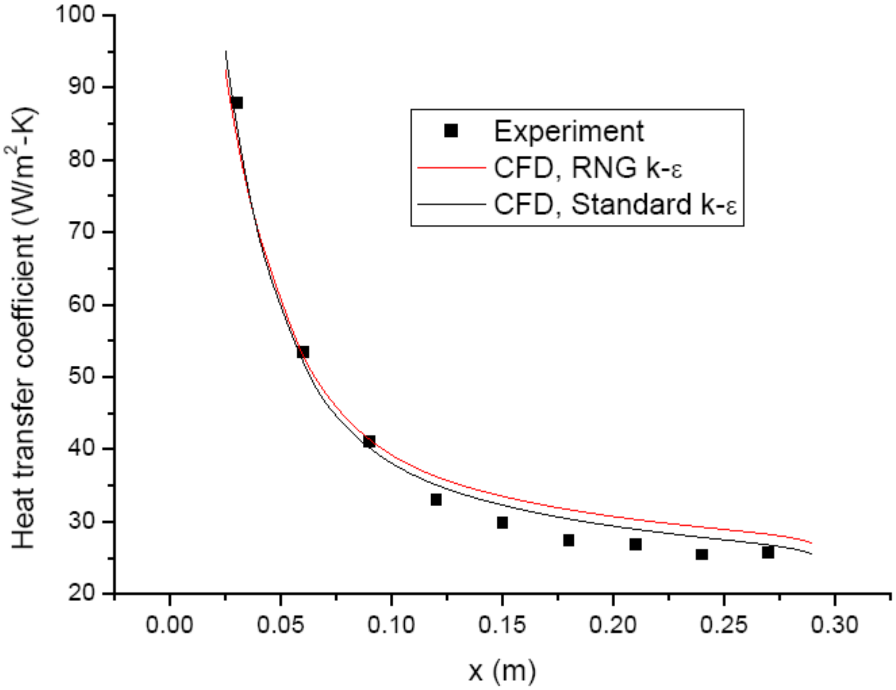

Figure 4-11 Comparison of heat transfer coefficient of the experiment and CFD simulations

The above figures show that the results predicted by the FLUENT model are in reasonable agreement with the experimental data. The agreement suggests that the model used here can be used to predict the behaviors of planar jet cooling experiments. The CFD simulations also contained detailed information about the flow field, in which the change in the velocity component parallel to the foil surface was of most interest. This velocity component, or the related momentum flux, was mainly responsible for convection heat transfer enhancement for the foil in planar jet cooling. The reduction in heat transfer enhancement along the flow direction was closely correlated to the reduction in the parallel momentum flux.

Figures 4-12 and 4-13 show the parallel velocity component profiles at various elevations and the contour of the velocity magnitude. The profiles expand and result in a lower velocity gradient at the wall as the jet proceeded upwards. More importantly, the maximum velocity value decreases and the location of the maximum value moves away from the foil, i.e. the wall shear stress decreases, which indicates the drop in convection heat transfer rate at higher elevations. A further examination of the contour plot shows that at a downstream distance of about 60 times the jet thickness, the maximum velocity is only about 30% of the jet exit velocity. This behavior explains why the heat transfer coefficients decay quickly along the length of the foil.

Near the top of the foil, the velocity profile becomes flatter because the effect of the jet diminishes due to jet deceleration, and the convection heat transfer was much more closely governed by the main stream flow. This was confirmed in the experiments, in which the heat transfer coefficients near the foil top with a jet injection were nearly the same as the values at the same location when no jet was present. The variation of the maximum parallel velocity component was also experimentally measured using a thermal anemometer. The measurements were compared to the CFD predictions in Figure 4-14. The agreement observed here further verifies the rapidly decreasing jet velocity along the flow direction, and confirms the suitability of the FLUENT model for predicting the behavior of planar jets.

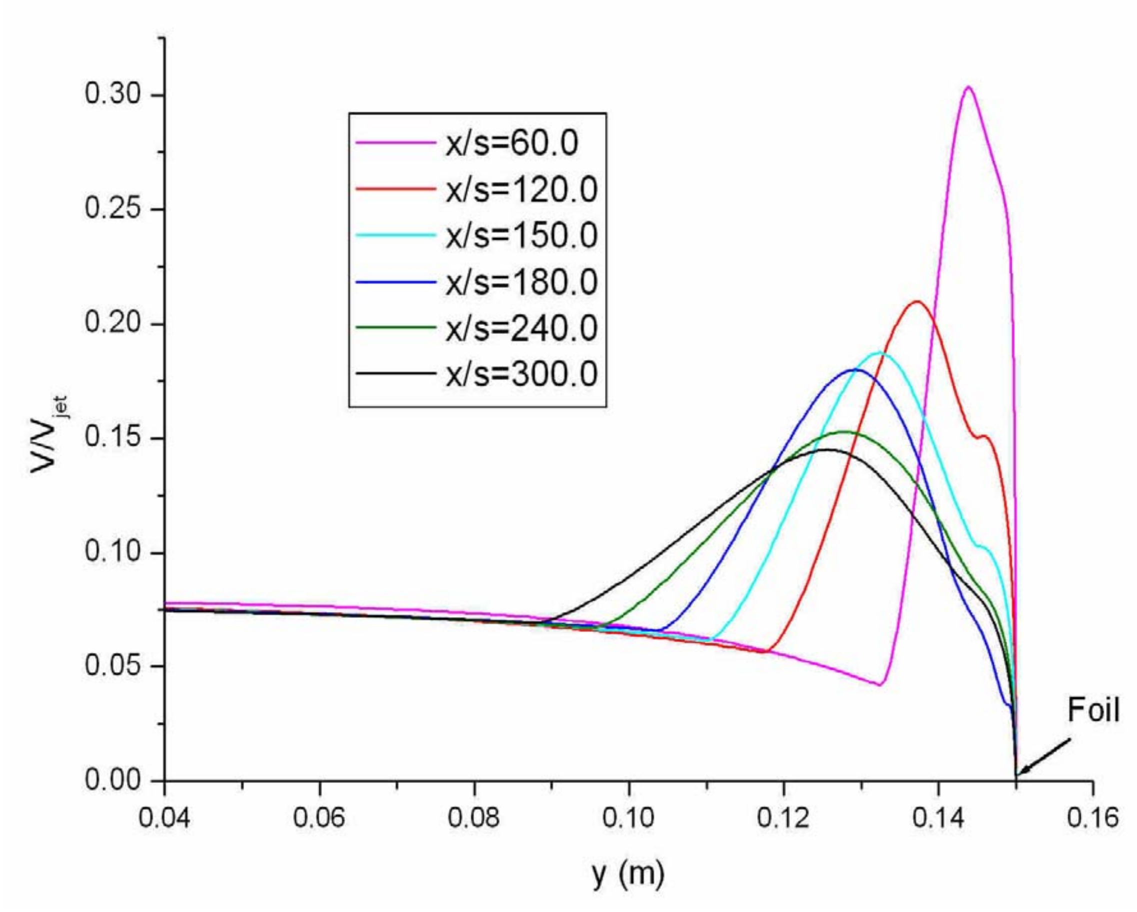

Figure 4-12 Normalized parallel velocity at various elevations

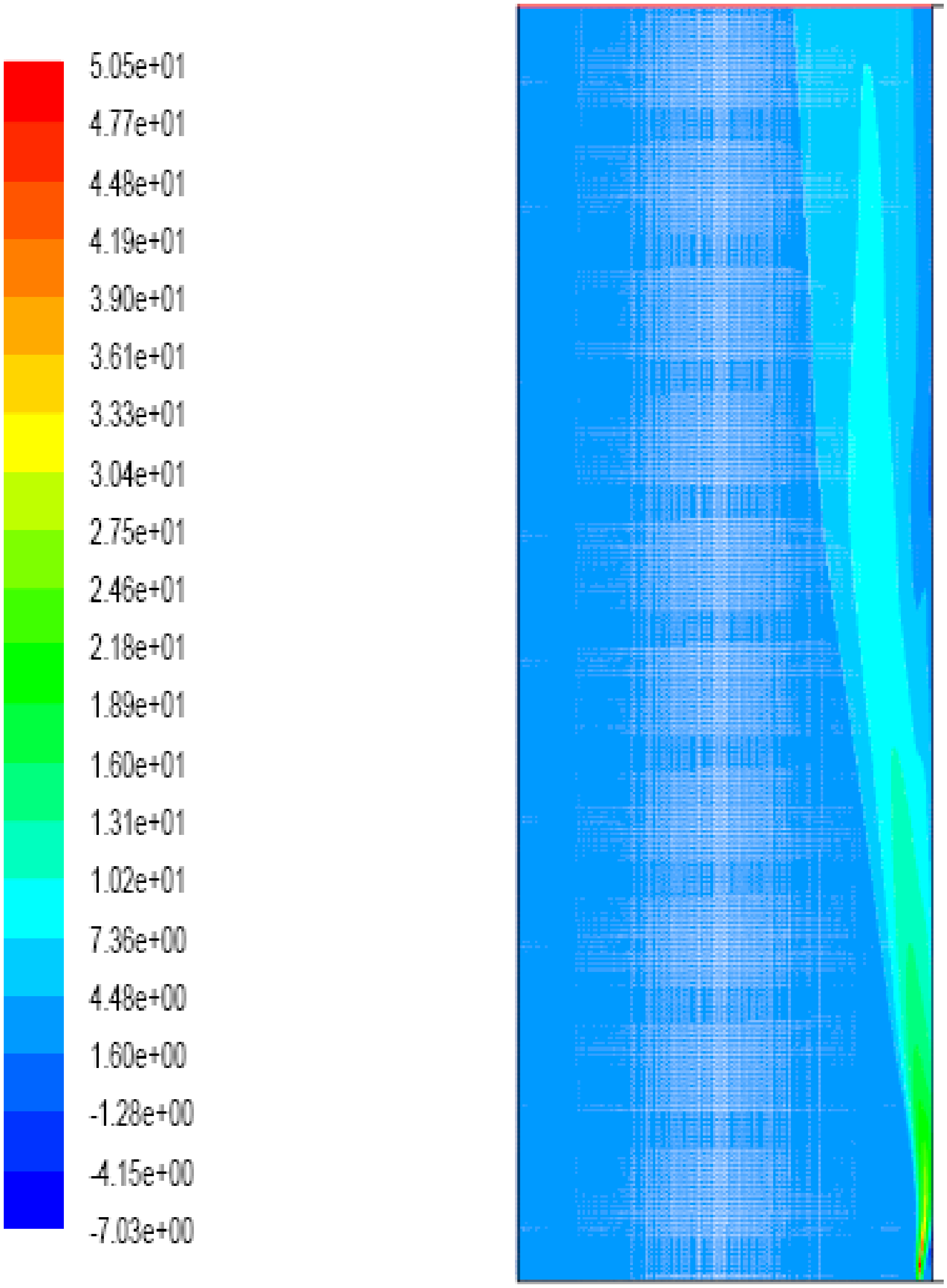

Figure 4-13 Contour of the parallel velocity inside the channel

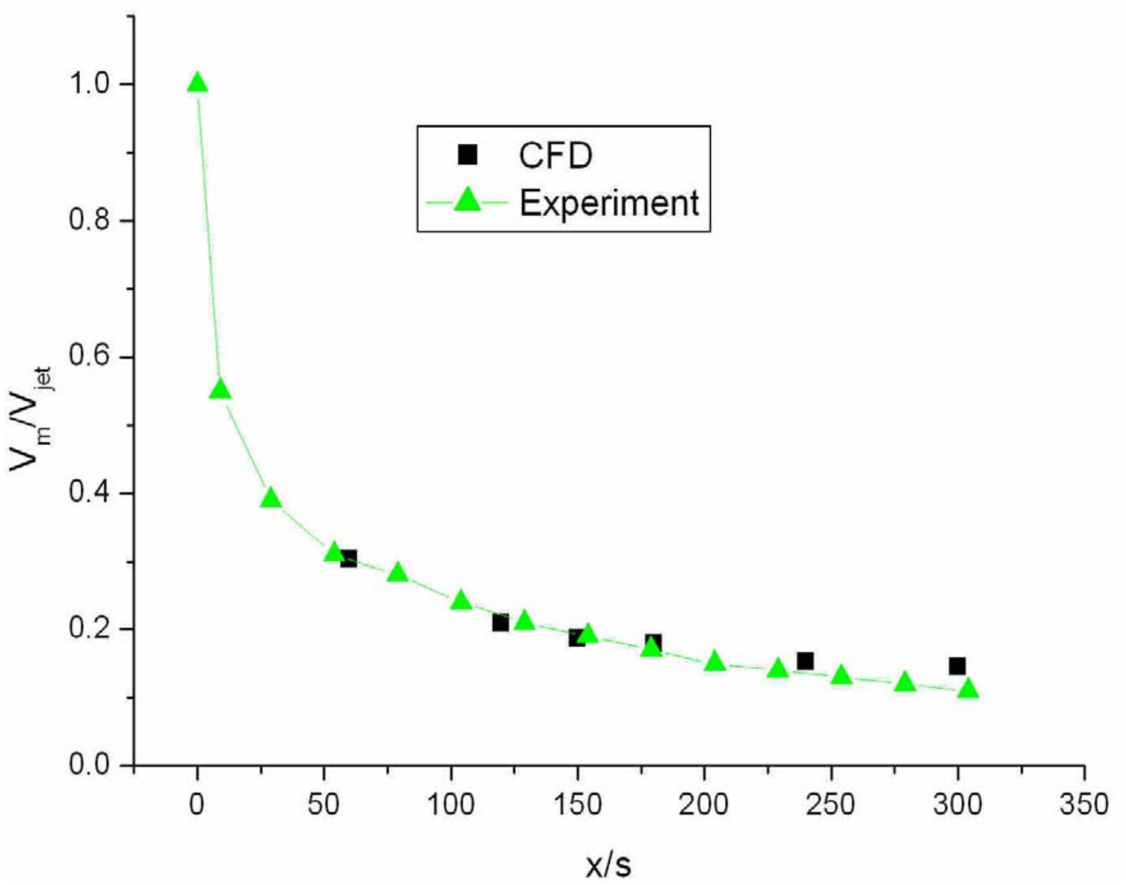

Figure 4-14 Maximum parallel velocity along the flow direction

CHAPTER 5

IMPINGING JET COOLING OF A HEATED FLAT FOIL

5.1 Introduction

To alleviate the shortcomings inherent in the planar jet cooling scheme, namely the inadequacy of cooling the top half of the hibachi foil, the concept of impinging jet cooling was proposed and investigated as an alternative effective cooling scheme. Convection heat transfer rate from the entire surface was elevated when rows or arrays of jets were arranged in a fashion such that the surface was uniformly covered. The heat transfer enhancement depended on jet Reynolds number, jet-to-jet pitch, jet-to-foil spacing, and jet impingement angles on the foil. This chapter summarizes both experimental and numerical investigations of impinging jet cooling of a flat foil.

5.2 Experimental Studies of Impinging Jet Cooling of a Flat Foil

5.2.1 Experimental parameters

The performance of impingement jet cooling was affected by various experimental parameters. In order to identify the essential factors that controlled heat transfer enhancement involved in impinging jet cooling, the jet-to-jet spacing on the jet tube in the current investigations was fixed at 1.25 cm in order to reduce the degree of freedom in the experimental parameters. This spacing was based upon earlier tests to maximize foil coverage and produce relatively uniform jet velocities along the length of the tube. Experiments were performed while varying jet flow rate, jet-to-foil spacing, jet diameters and jet impingement angles, with the impingement locations determined by the spacing and impinging angles. Surface heat flux values higher than 20.0 kW/m^2 were used in the experiments. Detailed experimental parameters are summarized in Table 5-1, where the impingement distance column refers to the distance of jet impingement location on the foil from the foil edge shown as a fraction of the foil width (*W*). Three jet headers with different jet diameters were used. Jet flow rates were chosen so that the jet Reynolds numbers overlapped for the different jet diameters. A large number of experiments were carried out to cover the ranges of the parameters.

Table 5-1 Experimental matrix of impinging jet cooling for a flat foil

Jet diameter (mm)	Spacer thickness (mm)	Impingement distance	Jet velocity (m/s)	Re_d
0.8	5.0-9.0	1/2W, 1/8W	10	518
			20	1035
			30	1552
			40	2070
1.2	5.0-9.0	1/2W, 1/8W	10	1552
			20	2329
			30	2717
			40	3105
1.6	5.0-9.0	1/2W,1/8W	10	1035
			20	2070
			30	3105
			40	4140

To characterize the heat transfer enhancement from the impinging jets, data analysis was performed for only one portion of the cooled foil that covered approximately four jets impinging on the foil. A typical experimental IR image is shown in Figure 5-1, for which both minimum and average temperatures were determined and the corresponding maximum and average heat transfer coefficients were calculated.

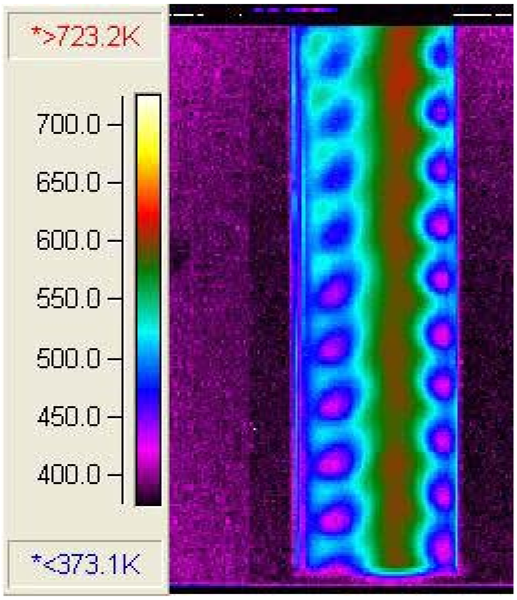

Figure 5-1 A typical IR image with the highlighted analysis box (shaded rectangle) (V_{jet}=10.0 m/s, d_{jet}=1.2 mm, impinging location: 1/8W, spacer thickness=5.0 mm)

The temperature and heat transfer coefficients were characterized as functions of jet-to-foil spacing, and impinging angles. These two variables, in addition to the jet Reynolds number, completely dictated the heat transfer rate of impinging jets in the current investigation, where the jet-to-jet spacing was fixed. Figure 5-2 shows the schematic of impinging jet cooling scheme, where *L* is the distance traveled by the jet before impingement, Φ is the impingement angle, and *S* is the thickness of the spacer separating the foil from the jet tubes where the jets are issued. The impinging angle and jet-to-foil spacing was adjusted by the combined effect of the spacer thickness and the rotation of the jet tube. Since the main objective of this study was to investigate the extent to which the heat transfer was enhanced with impinging jet impingement, experiments were run and IR images were recorded with each image corresponding to a distinctive case. Heat transfer characteristics including maximum and average heat transfer coefficients and Nusselt numbers were calculated and analyzed as functions of jet Reynolds numbers, jet impingement angles, and jet-exit-to-foil spacing.

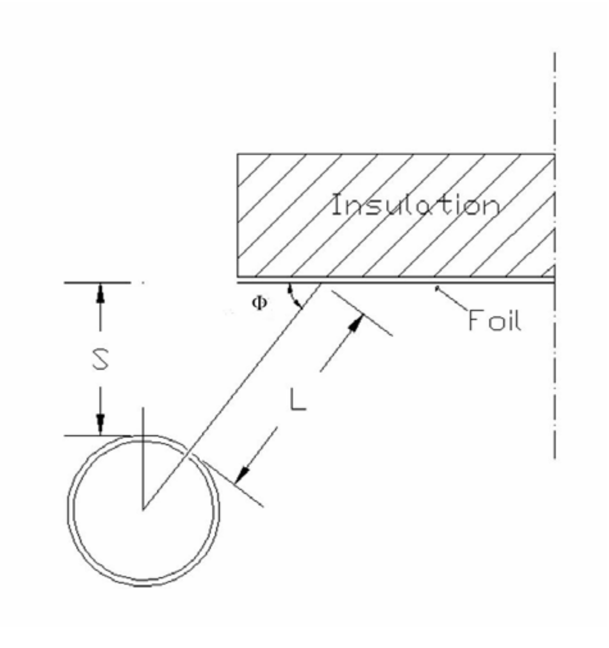

Figure 5-2 Schematic of impinging jet cooling of a flat foil

5.2.2 Summary of experimental results

A total of 96 experiments were run and 96 distinct IR images were generated. Each IR image corresponded to a set of experimental parameters, for each of which the maximum and average heat transfer coefficients and corresponding Nusselt numbers in the analysis box were computed. Before the jet was turned on, the average heat transfer coefficient resulting from the fan-driven bulk flow was first determined to be 59.3 W/m^2-K in the analysis box. Smirnov, *et al.* (1961) proposed that for $0.5<L/d<10.0$ and at a fixed impinging angle, the Nusselt number at the stagnation point is a function of Reynolds number and jet-to-foil spacing, and takes the following form,

$$Nu_{d,\max} = C_1 Re_d^{C_2} Pr^{1/3} \exp\left(C_3 L/d\right) \qquad \text{(Eq. 5-1)}$$

where,

$$Nu_{d,\max} = \frac{h_{\max} d}{k} \qquad \text{(Eq. 5-2)}$$

$$Re_d = \frac{\rho V_{jet} d}{\mu} \qquad \text{(Eq. 5-3)}$$

The correlation indicated that the Nusselt numbers were a power function of Reynolds number and also very sensitive to the jet-to-foil distance due to its exponential dependence. The correlation was shown to be in good agreement with the experiments of Smirnov, *et al*. (1961).

Experimental results from the current study were expected to follow a similar form when correlating the Nusselt numbers. For the current study, at a fixed impinging angle of 47°, a multivariate linear regression analysis rendered the following equation for experimental Nusselt numbers at the stagnation point as a function of jet Reynolds numbers and jet-to-foil spacing,

$$Nu_{d,\max} = 0.0839 \exp\left(-0.0994 L/d\right) Re_d^{0.8403} Pr^{1/3} \qquad \text{(Eq. 5-4)}$$

The above correlation accounted for both the effects of jet-to-foil spacing and Reynolds number at a given impact angle. Figures 5-3 and 5-4 show the correlation predictions along with the experimental data in a collapsed form. Most of the experimental data points fall within ±10% of the correlation predictions. The comparison again confirms that the Nusselt number was very sensitive to the jet-to-foil spacing due to its exponential dependence.

It is also very important to determine the overall and average heat transfer enhancement for the entire foil surface. For this purpose, average heat transfer coefficients and Nusselt numbers were obtained. Figures 5-5 and 5-6 show the average Nusselt number as a function of jet Reynolds number and jet-to-foil spacing in collapsed forms. The results were also correlated into the same form as that used for the maximum Nusselt number. The resulting correlation is given in Eq. 5-5:

$$Nu_{d,avg} = 0.0583 \exp\left(-0.0691 L/d\right) Re_d^{0.7786} Pr^{1/3} \qquad \text{(Eq. 5-5)}$$

The figures show that the correlation predicted the experimental data reasonably well, which indicated the correlation could be used to estimate the average heat transfer enhancement for the hibachi foil cooling in the gas lasers.

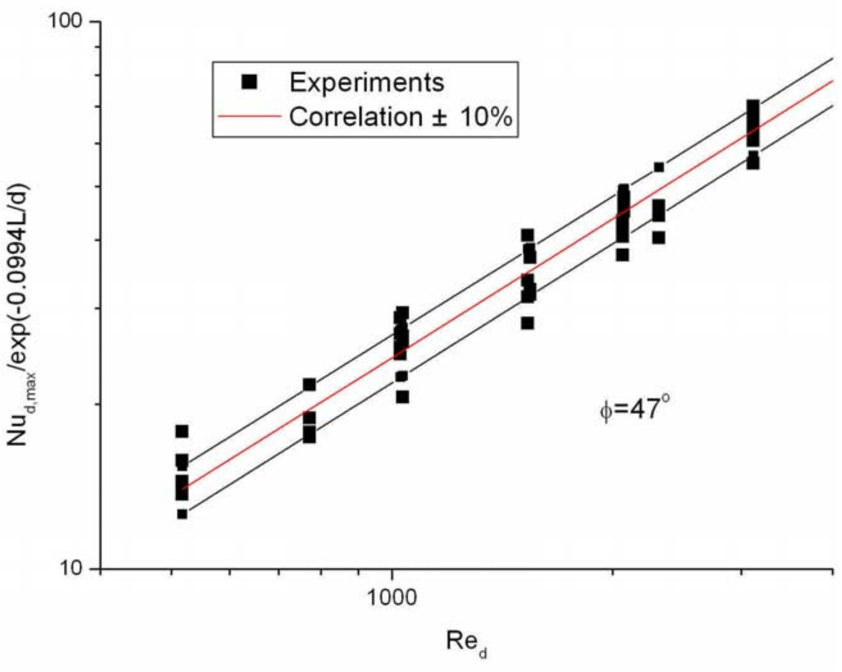

Figure 5-3 Comparison of maximum Nusselt numbers between correlation and experiments (Reynolds number as the independent variable)

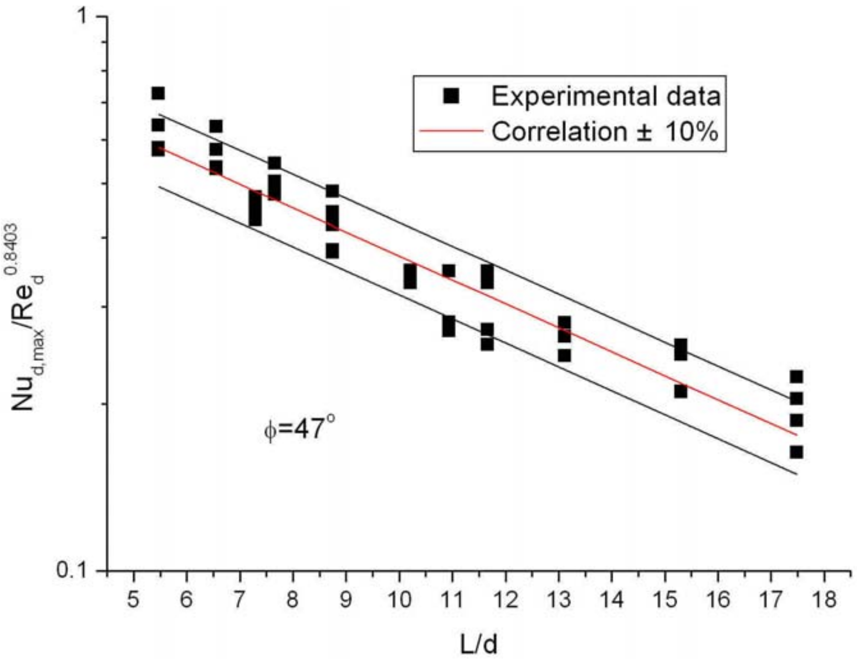

Figure 5-4 Comparison for maximum Nusselt numbers between correlation and experiments (Normalized Jet-to-foil spacing as the independent variable)

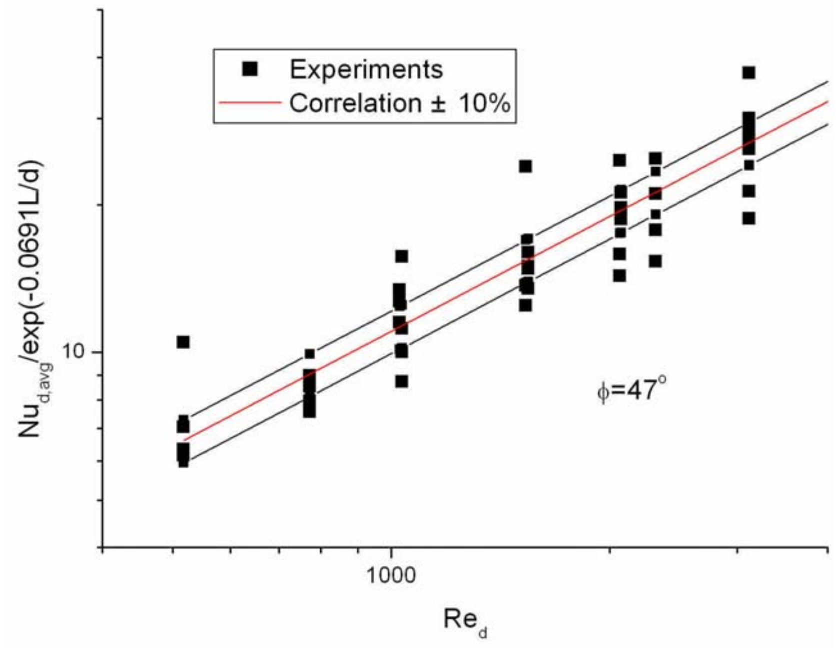

Figure 5-5 Comparison of average Nusselt numbers between correlation and experiments (Reynolds number as the independent variable)

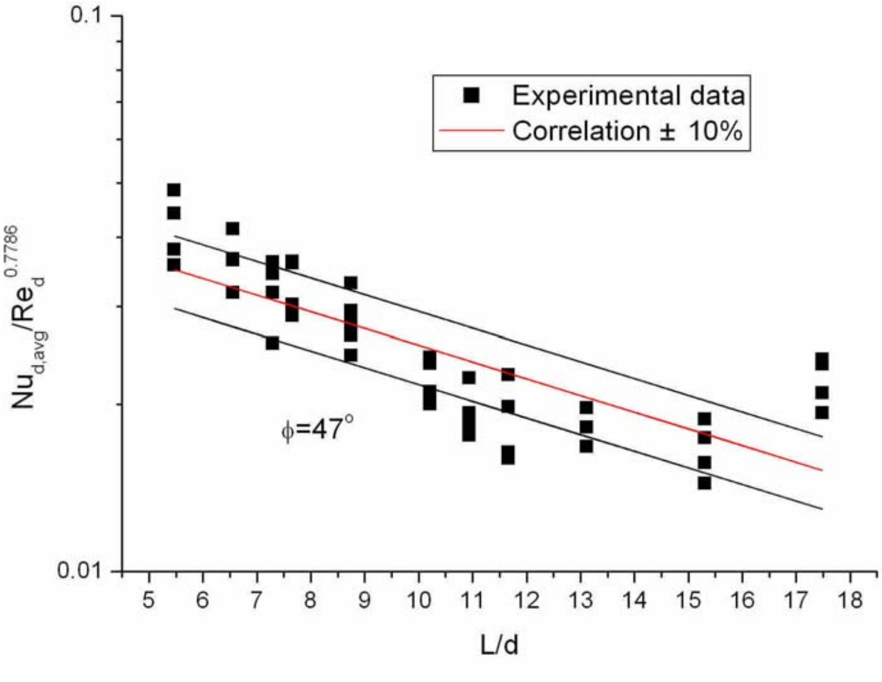

Figure 5-6 Comparison for maximum Nusselt numbers between correlation and experiments (Normalized jet-to-foil spacing as the independent variable)

5.2.3 Effect of jet Reynolds numbers

The experimental results obtained in this investigation will help determine the required total jet flow rate for the actual laser foil to meet the imposed constraint on the foil's maximum temperatures. However, the requirement of laser efficiency puts a limit on the available power of foil cooling, which in turn restricts the allowable pumping power.

Figures 5-7 and 5-8 show the maximum heat transfer coefficients and corresponding maximum Nusselt numbers as functions of jet Reynolds numbers for the case where the jets were issued towards the foil at a distance of 8.7 mm and an impinging angle of 47^{o}, i.e. the distance between the impingement point and the foil edge is 1/8 of the foil width.

The plots above show that higher jet Reynolds numbers result in higher heat transfer coefficients. It is also interesting to note that heat transfer coefficients for different jet diameters are nearly identical for the same jet Reynolds number. Figure 5-9 shows comparison between the experimental data and the correlation obtained in Eq. 5-4. The correlation was able to predict most of the experimental data points for this special case within an agreement of ±10%.

The average heat transfer coefficients for the analysis box were also computed for the same case to provide the detailed information about the overall heat transfer enhancement. Figures 5-10 and 5-11 show the average heat transfer coefficients and Nusselt numbers as functions of Reynolds number at various jet diameters. Compared with the maximum plots above, the average showed a slower rate of increase with Reynolds numbers. When implementing the actual foil cooling practice in the gas laser, the knowledge on average heat transfer coefficients will provide the information as to determine the desired jet flow rate under the constraint of pumping power assigned for foil cooling to preserve the required laser efficiency.

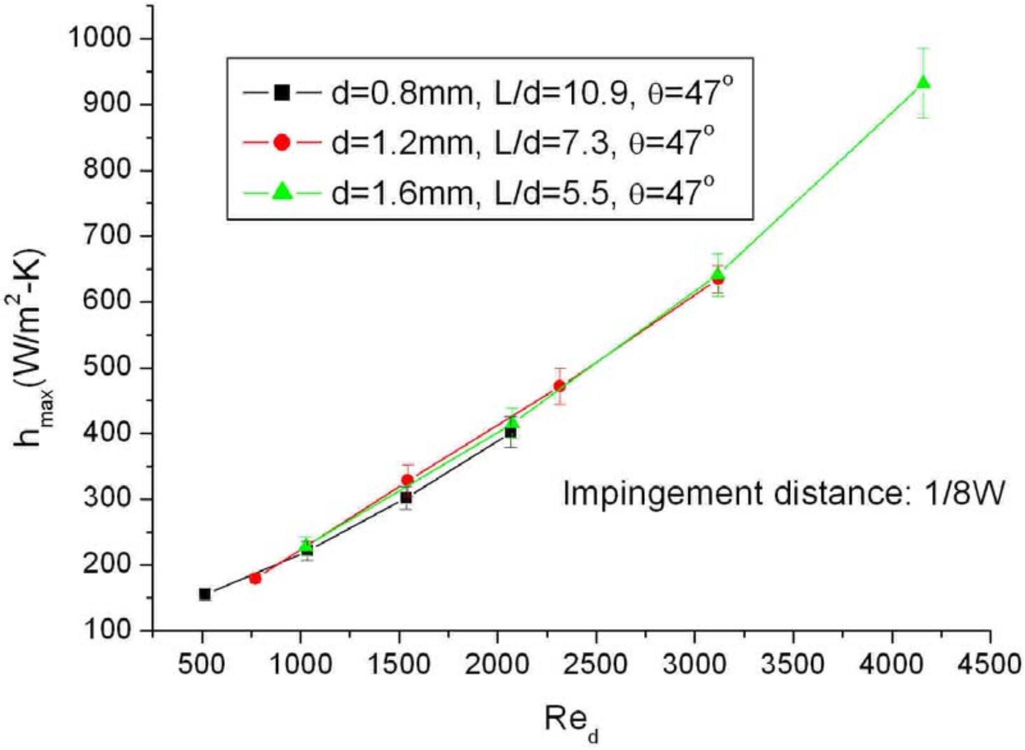

Figure 5-7 Maximum heat transfer coefficients at various Reynolds numbers

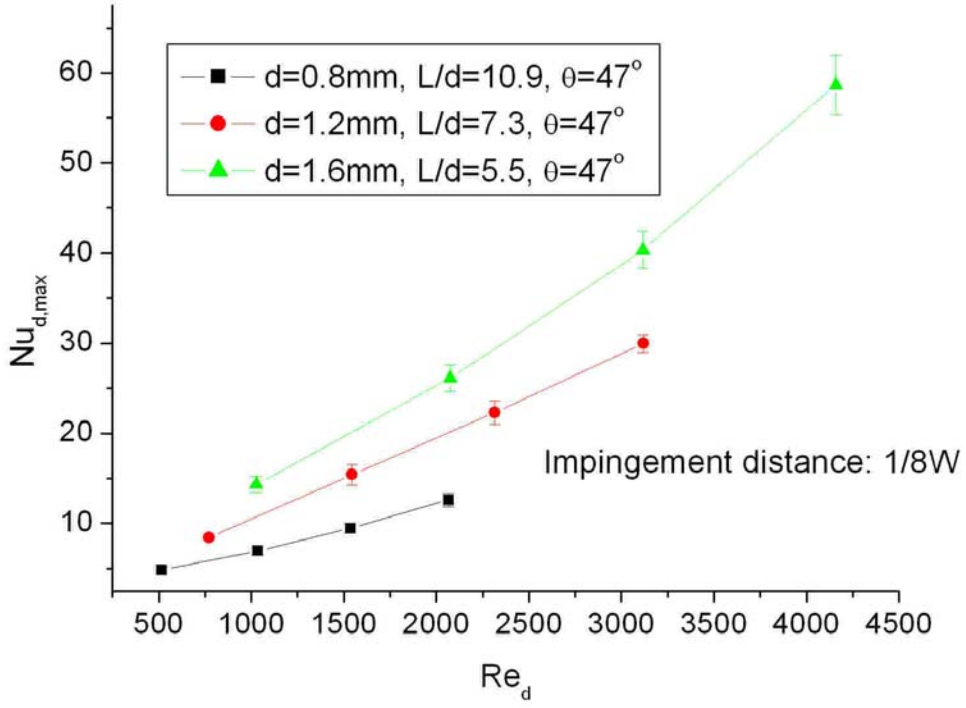

Figure 5-8 Maximum Nusselt numbers at various Reynolds numbers

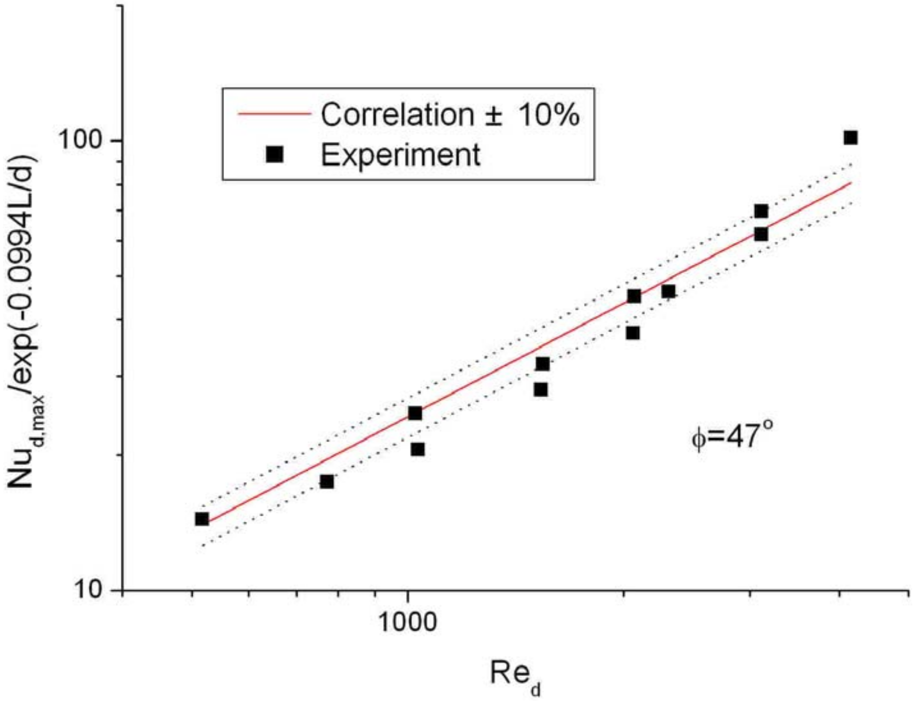

Figure 5-9 Comparison between experimental data and correlation

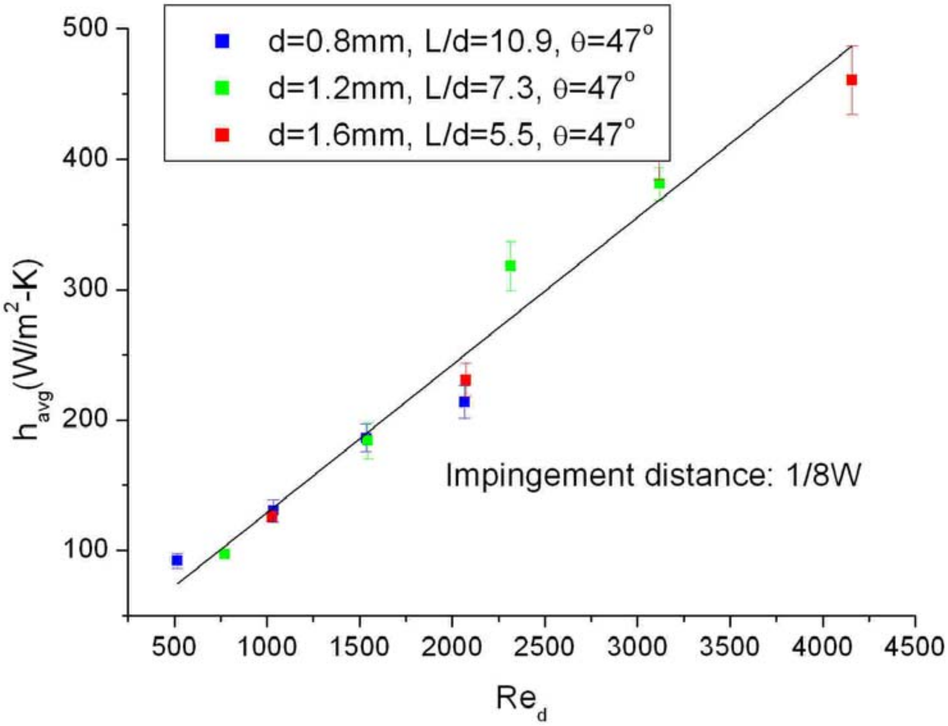

Figure 5-10 Average heat transfer coefficients as a function of Reynolds number

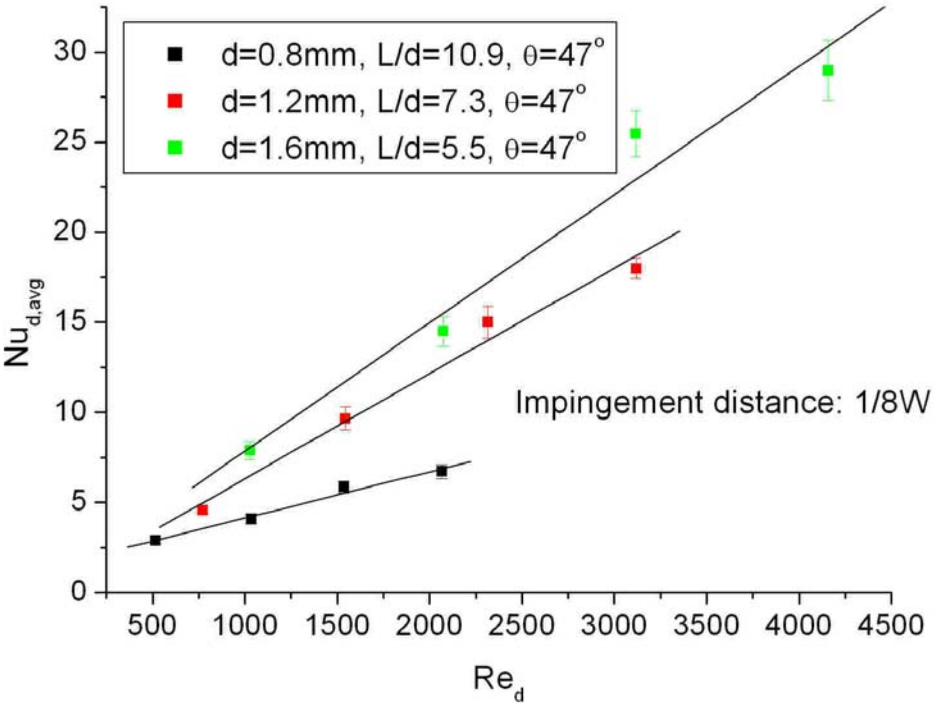

Figure 5-11 Average Nusselt number as a function of Reynolds numbers

Figure 5-12 also provides a comparison between the experimental results and the correlation (Eq. 5-5) of the average Nusselt numbers. The correlation is able to predict the experimental data within ±20%, which indicates that the correlation is suitable for predicting the cooling performance for the actual foil cooling for the gas laser. The selection of jet flow rate is limited by the available pumping power allocated for foil cooling, which is proportional to the product of jet flow rate and the pressure drop. The pressure drop between the exit of the rotameter and jet exits in the apparatus was measured for various jet Reynolds numbers for different sizes of jets for one set of two jet tubes that contain a total of 51 jets. Figure 5-13 and Figure 5-14 show the pressure drop and the pumping power for various jet Reynolds numbers and jet diameters, respectively. The figures show that the pressure drop increases significantly with jet Reynolds number. The figures also show that at the same jet Reynolds number, jets of a smaller diameter have a much higher pressure drop due to higher jet velocity.

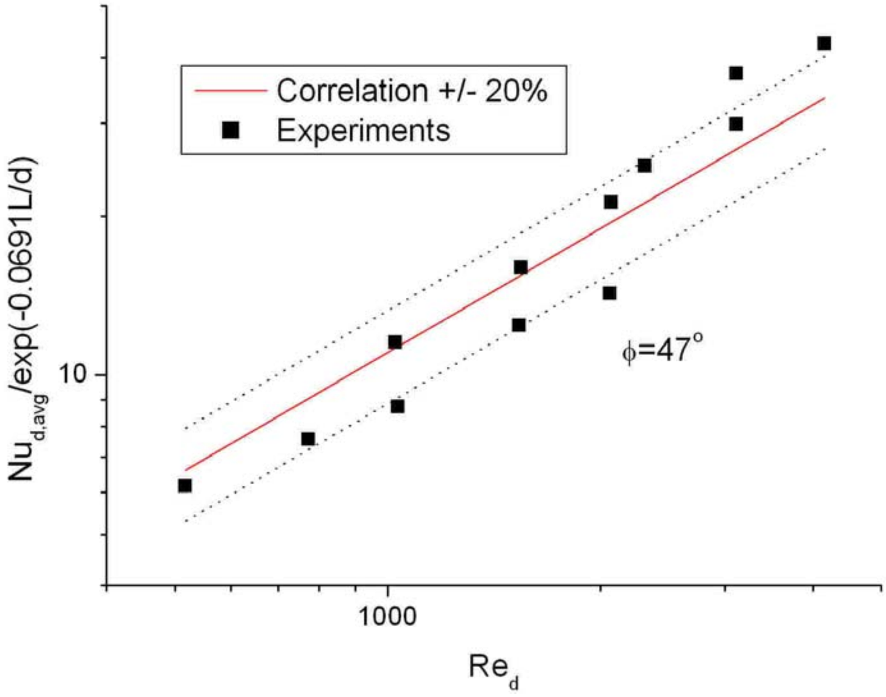

Figure 5-12 Comparison of experiments and the correlation for average Nusselt numbers

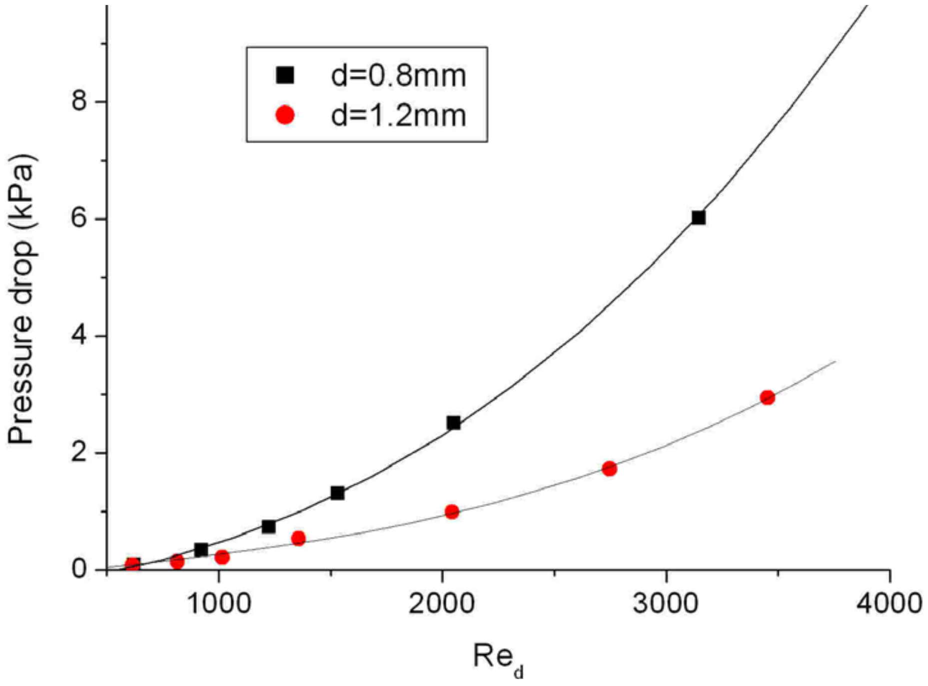

Figure 5-13 Pressure drop in the jet supply system at various jet Reynolds numbers

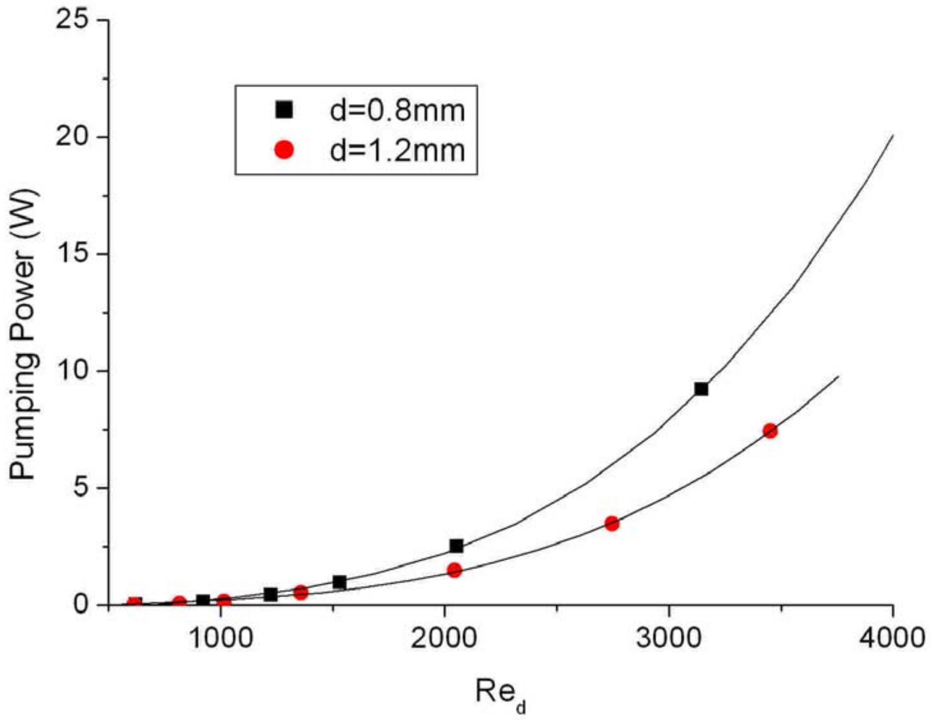

Figure 5-14 Pumping power for the jet supply system at various jet Reynolds numbers

5.2.4 Effect of jet-to-foil spacing

The distance between the jet exit and its impingement point on the foil is one of the dominant factors that govern the heat transfer characteristics in impinging jets. Nusselt numbers were shown to be strongly dependent on the normalized jet-to-foil spacing. Increasing the jet-to-foil spacing significantly reduces the convection heat transfer rate for cooling the heated surface. Experimental data were obtained at various values of jet-to-foil spacing that covered the desired operating parameter range for the actual foil cooling in Electra. Figure 5-15 and Figure 5-16 show the effect of jet-to-foil spacing on the heat transfer coefficients and Nusselt number at the stagnation point for different jet Reynolds numbers for jet diameter at 1.2 mm.

The plots show that the heat transfer coefficient decreases when the jet-to-foil spacing increases for all Reynolds numbers. Also the heat transfer coefficient decays at a faster rate at higher Reynolds numbers than at smaller Reynolds numbers. This is because the jet at higher Reynolds numbers has a longer potential core (i.e. the region downstream from the exit within which the uniform exit velocity is preserved) and its impingement heat transfer is more sensitive to the change in jet-to-foil spacing than the jet at lower Reynolds numbers. To achieve high heat transfer rate, smaller jet-to-foil spacing is desired in Electra.

Figure 5-17 and Figure 5-18 also plot the average heat transfer coefficients and associated Nusselt numbers for various Reynolds numbers. The plots show that the average quantities also decrease with jet-to-foil spacing but at a lower rate of decreasing. The results indicate that for the actual hibachi foil cooling in Electra it is desirable to issues the jets as closely as possible to the foil to achieve the maximum heat transfer enhancement for the foil.

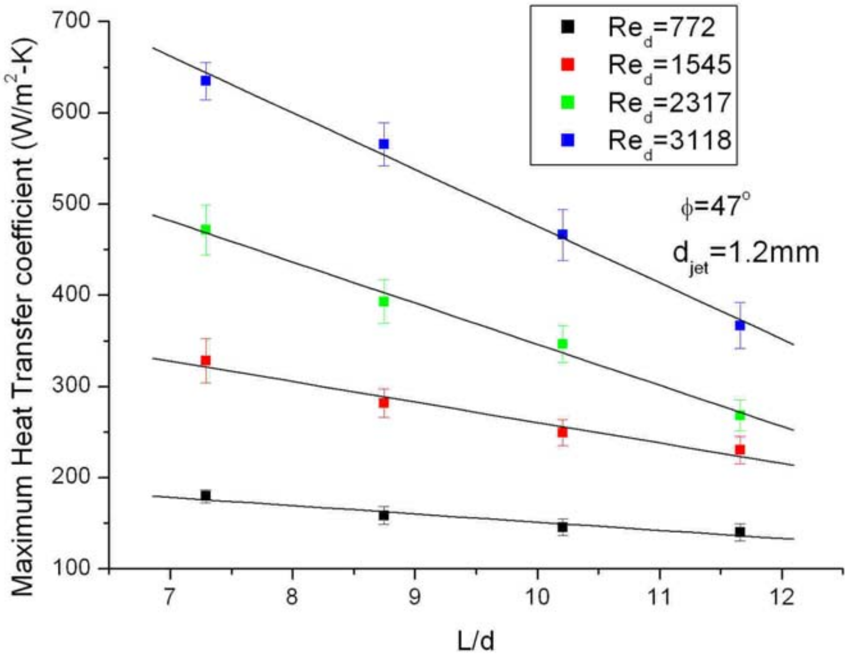

Figure 5-15 Maximum heat transfer coefficients vs. jet-to foil spacing at different Reynolds number

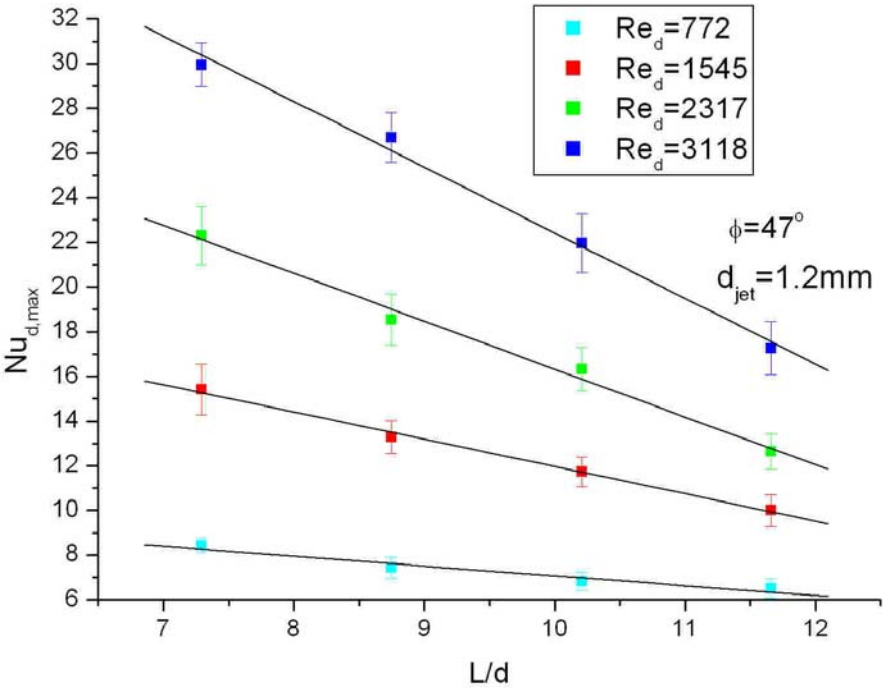

Figure 5-16 Maximum Nusselt numbers vs. jet-to foil spacing at different Reynolds numbers

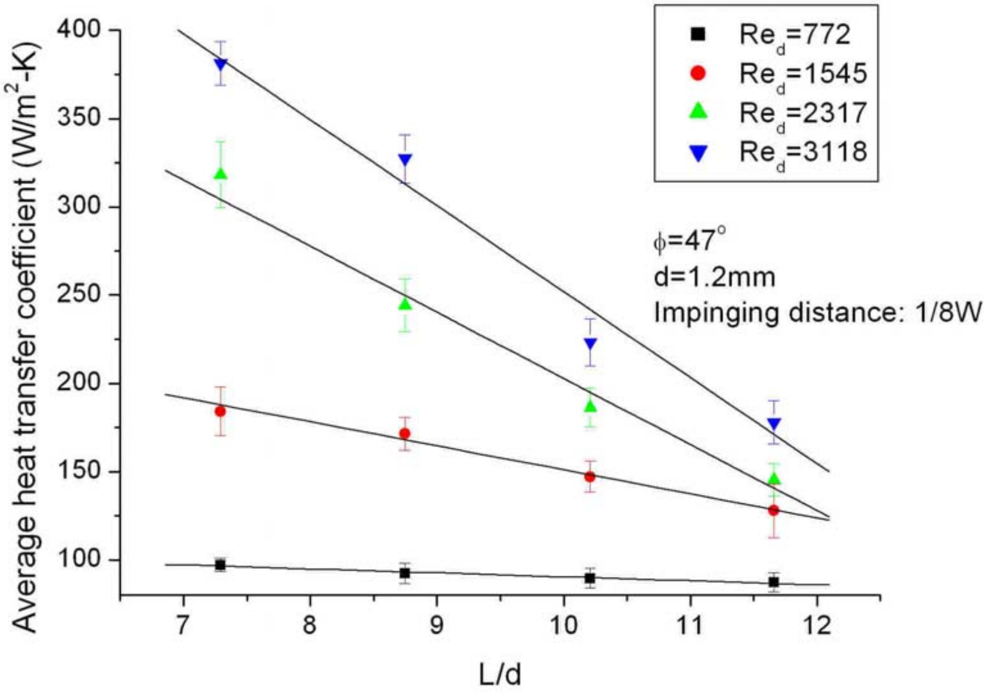

Figure 5-17 Average heat transfer coefficients vs. jet-to foil spacing at different Reynolds numbers

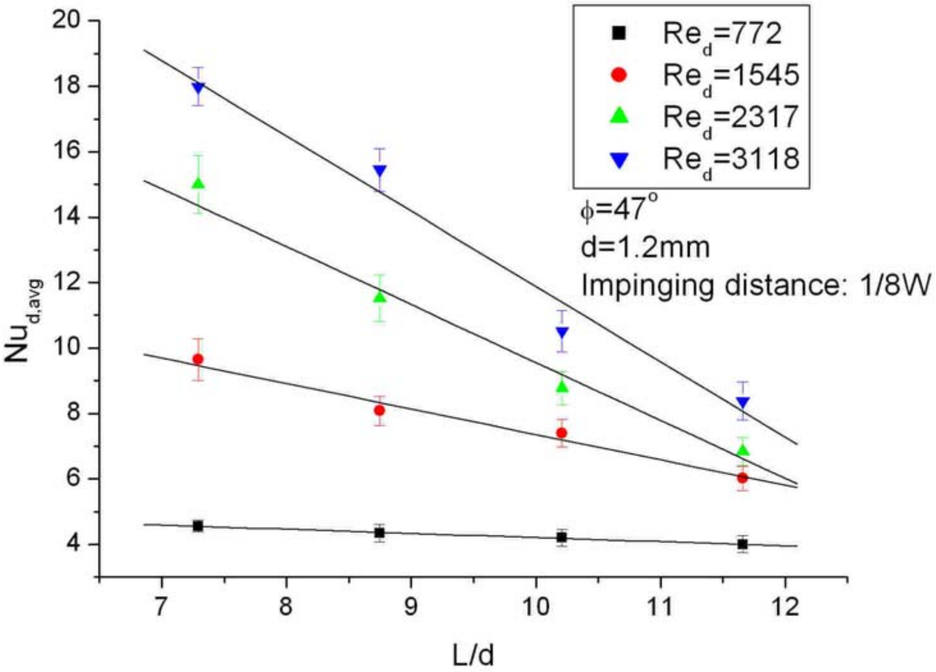

Figure 5-18 Average Nusselt numbers vs. jet-to foil spacing at different Reynolds numbers

5.2.5 Effect of jet impingement angles

Previous experimental studies indicated that maximum heat transfer rate was attained when the jet impinges on the surface perpendicularly. At other obliquely impinging angles, the heat transfer rate was reduced; the extent of reduction was dependent on the actual impact angle. For the specific application of gas laser's hibachi foil cooling, jets have to be issued obliquely from two parallel jet tubes that are located on the two foil's edges to minimize the blockage of electron beam. Also the diameter of the jet tube has be less than or equal to the rib width in order not to affect the pathway of electron beams. In the current investigation, where the foil has a large aspect ratio, two different impact angles (47^o and 24^o) were investigated. At these two angles, the jets on each side of the foil were aligned to impinge on two vertical lines. The first one was 1/8 of the foil width from the edge, while the other corresponded to jet impinging at the centerline between two adjacent ribs. These two configurations offered a direct comparison of the effect of impinging angles on the heat transfer capability.

When the impact angle changed from 47^o to 24^o, the experimental data were correlated in a different form due to the dependence of Nusselt number on the impinging angle. The previous correlation accounted for both jet-to-foil spacing and jet Reynolds number. When the impact angle changes, the dependence on jet Reynolds number is not expected to change since jet Reynolds number is independent of the impact angle. However, the jet-to-foil spacing was affected by the impact angle; hence a change in the coefficient was expected for the jet-to-foil spacing.

The multivariate linear regression technique was applied to the experimental data with an impingement angle of 24^o and a correlation was obtained,

$$Nu_{d,max} = 0.0422 Re_d^{\,0.8472} \exp\left(-0.0492\, {}^{L}\!/_{d}\right) \qquad \text{(Eq. 5-6)}$$

Figure 5-19 shows the above correlation and the experimental data in a collapsed form. The correlation was shown to be able to predict most experimental points with an accuracy of ±10%. Compared to the correlation for the impact angle at 47°, changes in the constants were observed as expected. The exponent for jet Reynolds number was nearly unchanged (0.8472 vs. 0.8403), while the constant in the exponential function for the jet-to-foil spacing increased from -0.0994 to -0.0492, and the proportional constant decreased from 0.0734 to 0.0422.

It is interesting to graphically show the variation of these two correlations over the spacing at a fixed jet Reynolds number. Figure 5-20 shows the change of Nusselt number as a function of normalized jet-to-foil spacing at a fixed Reynolds number of 3000 for the two impingement angles. For the larger angle, Nusselt number decreased exponentially at a faster rate than at the smaller angle. When the normalized jet-to-foil spacing was less than 10.0, Nusselt numbers were larger at the bigger impact angles. For normalized jet-to-foil spacing greater from 10.0, Nusselt numbers at the smaller impact angle became larger than those with the larger impact angle. For the cooling of the hibachi foil, the impinging jets were restricted to issue from two jet rows that sit parallel to the two edges of the vertically-installed foil. By this configuration and at a fixed spacer thickness, the actual jet-to-foil spacing was much larger at a smaller impact angle, which resulted in much lower heat transfer coefficients. The jet-to-foil spacing can be adjusted by placing “spacers” between the header tube and the foil plane (see Figure 5-2). Figure 5-21 shows the normalized Nusselt number as a function of the spacer thickness used in the experiments for a jet diameter of 1.2 mm. The figure shows that the normalized Nusselt number at 47^o was about twice the values at 24^o, which implied that it was desirable to issue the jets at large angles and near the edges of the foil to effectively cool the gas laser's hibachi foil. The figure also shows that the Nusselt number gradually decreases as the spacer thickness increases. Hence, the hibachi cooling system design should minimize the distance between the header tubes and the foil plane (i.e. the ribs).

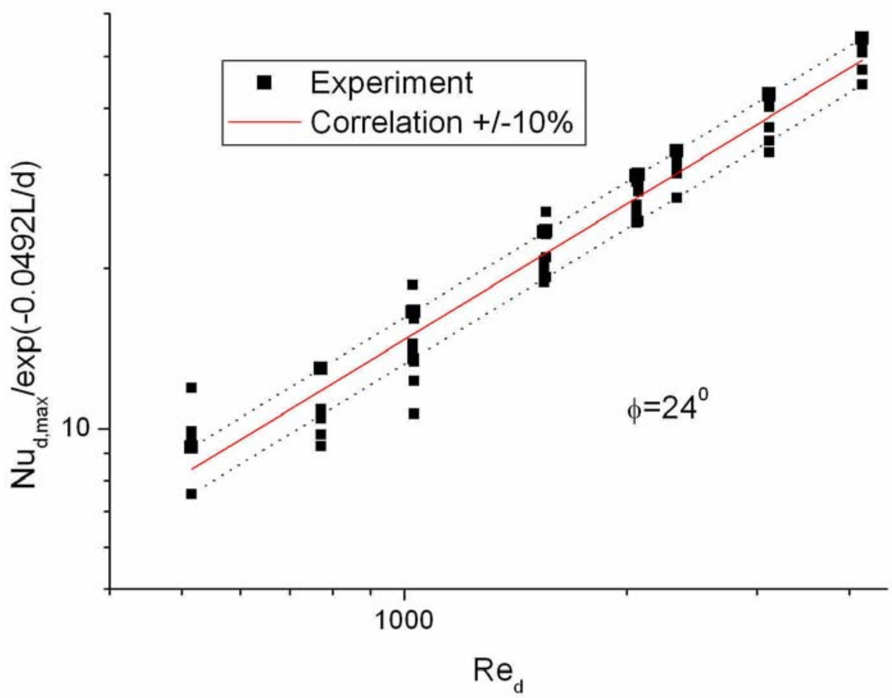

Figure 5-19 Comparison between experimental data and the correlation for $Nu_{d, max}$

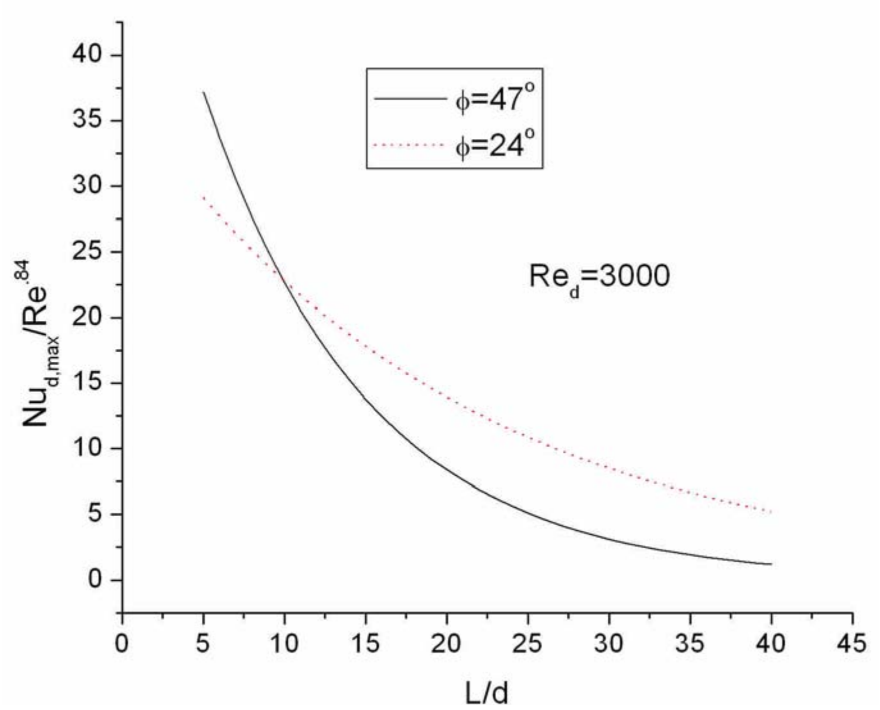

Figure 5-20 Comparison of Nusselt number variation at different impingement angles

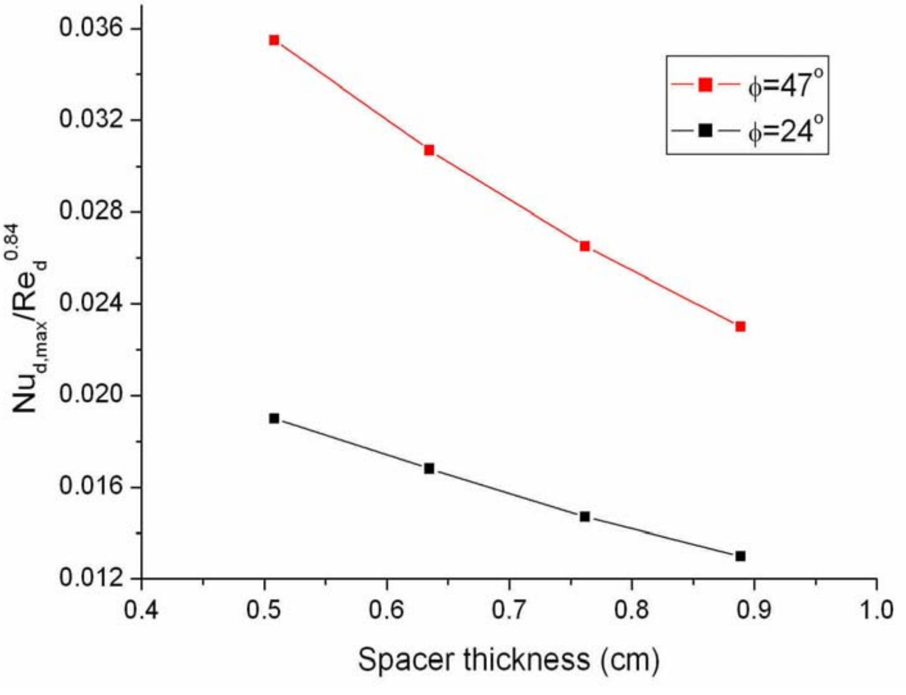

Figure 5-21 Comparison of Nusselt number at different impinging angles

5.2.6 Effect of impingement location on average heat transfer rates

The proposed impinging jet cooling scheme issues small-diameter circular jets obliquely towards the foil from two parallel jet tubes that are attached to the edges of the foil. Jets impinge on the foil at locations either very close to the edges or near the centerline, which have very different flow path and impact angles before impingement. At a fixed jet Reynolds number, these two configurations presented very different heat transfer characteristics due to their different flow path and impact angles. It was shown in the previous section that at the same spacer thickness and jet Reynolds number, jets that impinge near the foil edge produced larger stagnation Nusselt numbers than those impinging on the centerline of the foil due to the dominance of the jet-to-foil spacing. It was also shown that when the jet-to-foil spacing increases, Nusselt numbers at large impact angles decayed exponentially at a faster rate than those at a smaller angle. This may affect the average cooling effectiveness when it comes to the consideration of overall cooling performance.

Average Nusselt numbers at these two different impinging locations were computed at various Reynolds numbers. Figure 5-22 shows the average Nusselt numbers over the analysis box as a function of jet Reynolds numbers with jet diameter of 1.2 mm and the same spacer thickness of 0.5 cm for both impingement locations. Due to the shorter flow path, jets impinging near the edge of the foil produced much higher average heat transfer coefficients (i.e. Nusselt numbers) than jets issued towards the centerline of the foil. It again confirms that for the application of foil cooling in gas lasers it is desirable to issue the jets that impinge very close to the foil edge, which offers better overall heat transfer enhancement for the hibachi foil.

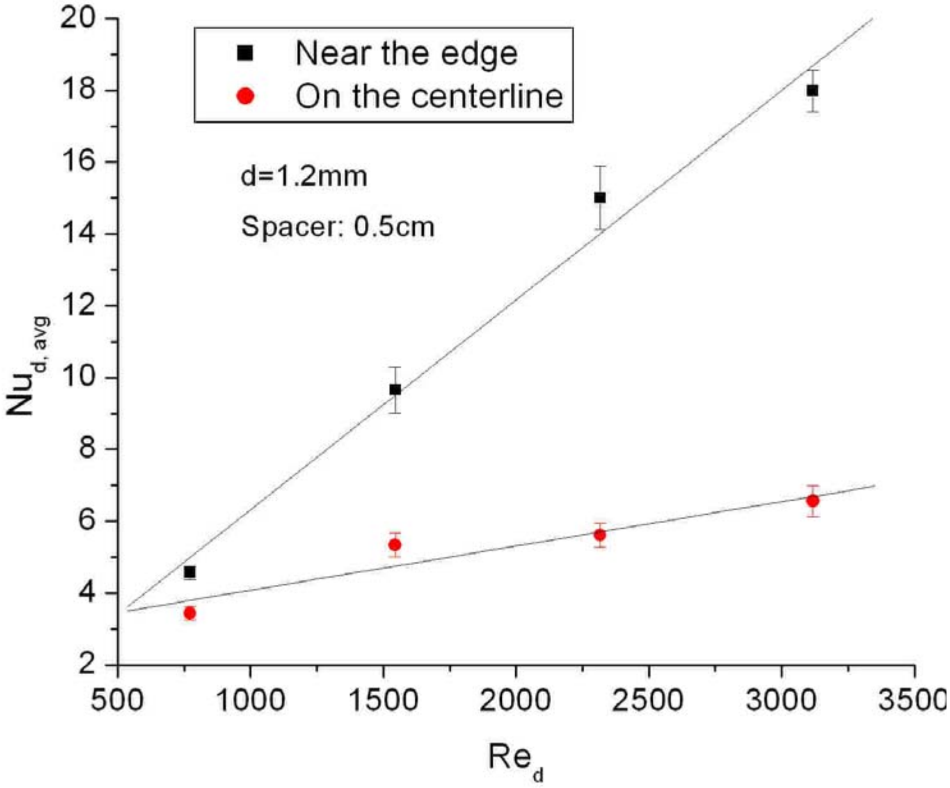

Figure 5-22 Average Nusselt number at different impingement locations

5.3 CFD Studies of Impinging Jet Cooling for the Flat Foil

5.3.1 Model geometry

CFD simulations of impinging jet cooling for a flat foil require a three-dimensional model due to its three-dimensional flow field. The large ratio between the bulk flow area and the small jet area presents a big challenge in the nodalization of the model to avoid generating many highly skewed cells. A three-dimensional model was created in GAMBIT® for CFD simulations in FLUENT®, which included the following simplifications:

- The geometry of the model had a smaller bulk flow area and a shorter foil length than the actual flow channel to decrease computational demands;
- A total of 20 interlacing jets were modeled with ten jets on each side;
- The impinging jets were modeled as issuing all at the same velocities from circular openings on two vertical side surfaces, with the specified mass flow rate and at the specified orientations;
- The foil was modeled as a wall under constant surface heat flux that was set at the estimated value from the measured power input;
- The bulk flow was simulated by imposing an inflow with a uniform velocity profile.

Figure 5-23 shows the rectangular parallelepiped model created using GAMBIT® for CFD simulations in FLUENT®. The model is 12.5 *cm* high, 3.4 *cm* wide and 4.1 cm deep. Jets are evenly spaced along the length of the two sides at intervals of 1.25 cm. Each jet diameter is 0.8 mm and is separated from the foil by a horizontal distance of 0.5 cm. These parameters are fixed for the simulation performed here. The Reynolds numbers and jet impingement angles are the variables. Since the model geometry is smaller than the actual geometry of the test section, the boundary conditions at the side surfaces (except the foil surface) are set such that there is gas entering and leaving. This is a reasonable approximation for the phenomena occurring in the experiments.

The meshing of the model needs to resolve the jets that are of very small area, which requires a large number of nodes to be used. A total of 408,400 cells are generated for the 3D model. A close-up view of the meshing nearing the jet is shown in Figure 5-24. An unstructured mesh was generated for the jet surface to provide good resolution for the area in the vicinity of the jet inlet. The meshing of the 3D model is performed by sweeping horizontally between two side walls and generating a regular grid of hexahedral elements, which helps improve the speed of convergence in the simulations.

5.3.2 Boundary conditions

The main boundary conditions used in the steady-state CFD simulations in FLUENT® are specified as follows:

- q'': The uniform surface heat flux specified at the foil surface (W/m^2).
- $\dot{m}_{in}$: The mass flow rate at the jet exit with appropriate orientations (kg/s). For turbulence modeling, the turbulence intensity at the inlet is calculated using an empirical correlation suggested in the FLUENT® user manual: $I = 0.16Re^{0.125}$.
- T_{in}: The air temperature at the inlet (^{o}C).
- h_{conv}: The convection heat transfer coefficient at the side walls to account for the heat loss to the surroundings due to natural convection (W/m^2-K).
- *Pressure outlet*: This boundary condition is set at the top and three side surfaces to allow the spent air resulting from jet impingement to leave and enter.

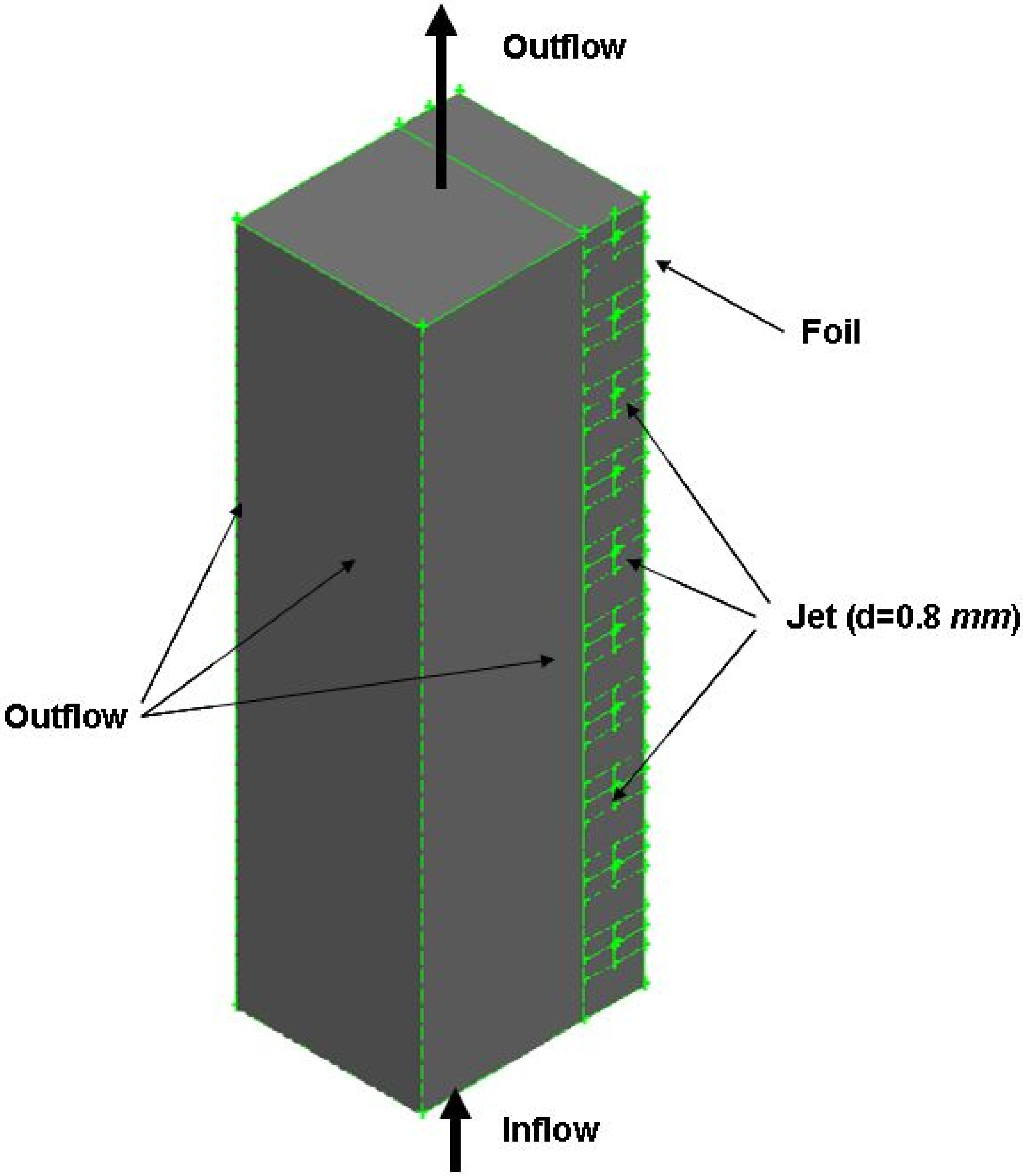

Figure 5-23 CFD model for impinging jet cooling for the flat foil

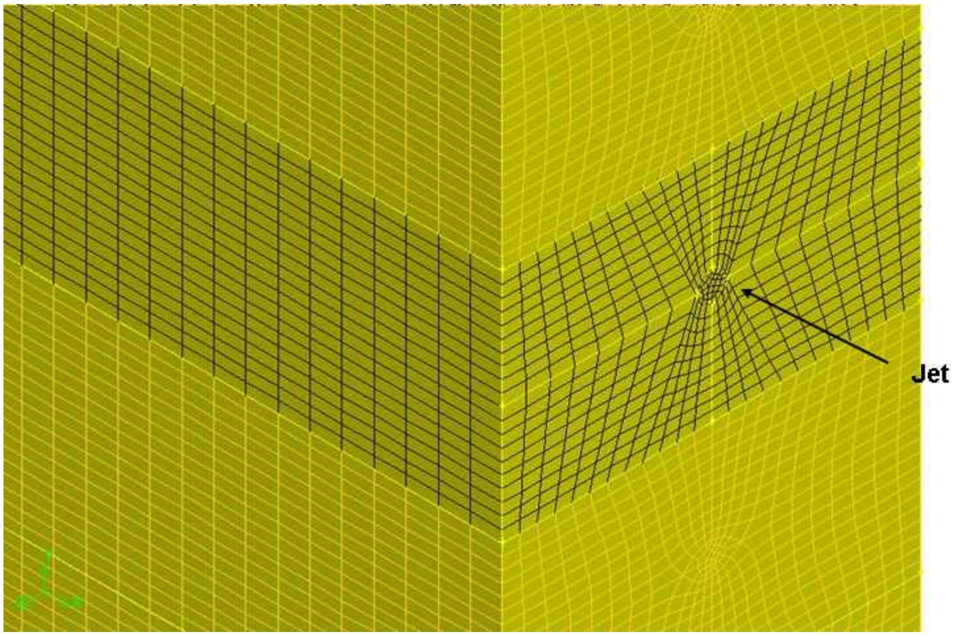

Figure 5-24 Close-up of the computation grid for impinging jet cooling for the flat foil
(29 unstructured elements were generated for the jet for good resolution)

In addition to the boundary conditions, air is used in all the simulations and is regarded as an ideal gas for the compressible flow.

5.3.3 Simulation parameters and results

CFD simulations performed in the current investigations use a simplified 3D model plus simplified boundary conditions, so it is not surprising that the results from these simulations deviate from the current experimental results. The purpose of the CFD simulations is to show that CFD tools can predict the heat transfer characteristics of impinging jet cooling. In the simulations, the jet orientation is adjusted so that the impingement locations are the same as in the experiments. The mass flow rates of the jets, the bulk flow, and the surface heat flux of the foil are set to the corresponding experimental values. Also, the second-order upwind differencing scheme is applied for solving continuity, momentum energy, turbulence kinetic energy, and turbulent dissipation rate equations for a more accurate solution. The convergence criteria for all the variables, i.e. the residual limits, are set at 1e-6 for the energy equation and 1e-3 for all the other equations.

Realizable *k-ε* turbulence model with non-equilibrium wall function was used in the simulation, which was suggested by FLUENT® manuals for impinging jet modeling (Shih, et. al., 1995). This modified turbulence model incorporates a new formulation for the turbulent viscosity and a new transport equation for the turbulent kinetic energy dissipation rate (*ε*) that was derived from the exact formulation for the transport modeling of the mean-square vorticity fluctuation. This model offers an immediate benefit in more accurately predicting the spreading of the impinging jets. For near-wall treatment in the simulations, the non-equilibrium wall functions were invoked, which is based on a two-layer concept to compute turbulent kinetic energy in the near-wall cells and can partly account for the non-equilibrium effect that is neglected in the standard wall function (Kim and Choudhury, 1995). The non-equilibrium wall functions are suggested to be used in complex flows where the mean flow and turbulence changes rapidly, such as in the impingement zone of an impinging jet.

In the simulation, air jets of 0.8 mm diameter and 30.0 m/s (Re_d=1552) are aimed to impinge on the foil at an impinging distance of 1/8W with a spacer thickness of 0.5 cm, which corresponds to the non-dimensional jet-to-foil spacing of 8.8. The bulk flow was imposed at the inlet of the model. The surface heat flux at the foil is set at

20.0 kW/m^2, which is a typical experimental value.

Figure 5-25 shows the contour of the foil temperature for the above case. It is obvious that there is a strong periodic behavior in the distribution of foil temperature. However, the area near the channel inlet is strongly affected by the boundary condition and model geometry (the bottom and top jets are very close to the inlet and outlet). To illustrate the jet impinging cooling characteristic, the analysis was restricted to four jets located on the jet row on each side to reduce the entrance effects on the simulation results, which corresponded to a smaller foil area for analysis (3.4 cm wide and 5 cm high, black dotted area in Figure 5-25).

Figure 5-26 and 5-27 show the contours of foil temperature and heat transfer coefficients of the analysis rectangle, respectively. Areas of hot spots are found to be near the centerline of the foil due to the limited spread of the jet. The maximum and average heat transfer coefficients are 98.1 and 73.1 W/m^2-K, respectively. However, the contours do not show the normal elliptic shape of spread, but shows a distorted shape, indicating the irregular jet spread predicted by the turbulence model. The predicted heat transfer characteristics are closely related to the jet flow distribution upon impingement. Figure 5-28 shows the pathlines of the jets coming out of the left row of holes before and upon impingement. It clearly shows that the jet first spreads out before impingement and a split in the jet is formed that causes the distortion in the heat transfer characteristics upon impingement.

An experimentally obtained IR image with similar parameters as the simulated case is shown in Figure 5-29. Comparing it to the simulated temperature contour, the CFD model is able to predict the similar pattern of temperature distribution, though it predicts higher foil temperature. This is because this model is much smaller in size than the actual experimental setup and less heat can be dissipated or transferred to the ambient, which produces higher foil temperatures even though the same surface heat flux is used in the simulations.

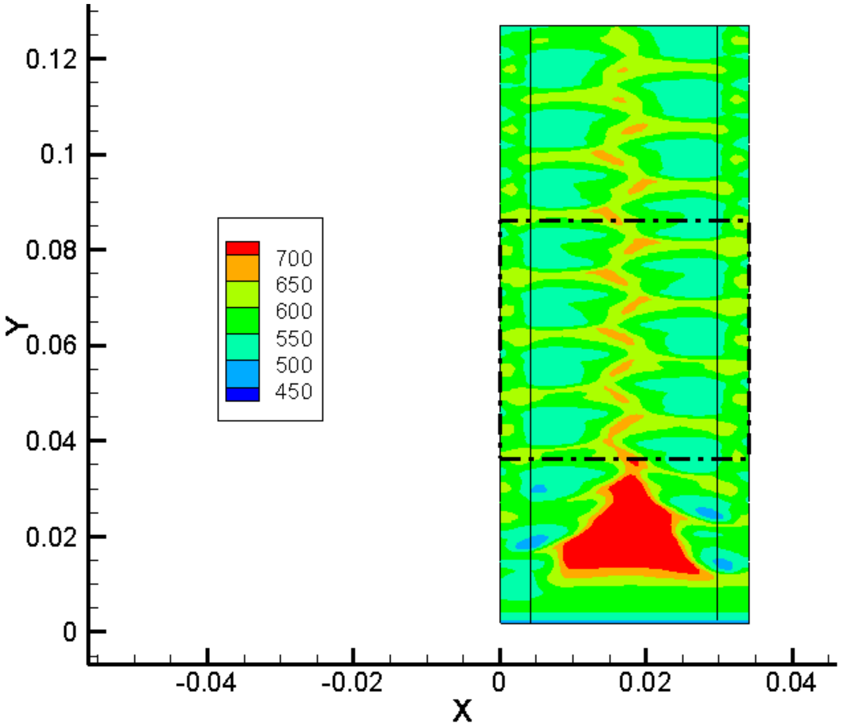

Figure 5-25 Simulated foil temperature contour (K)

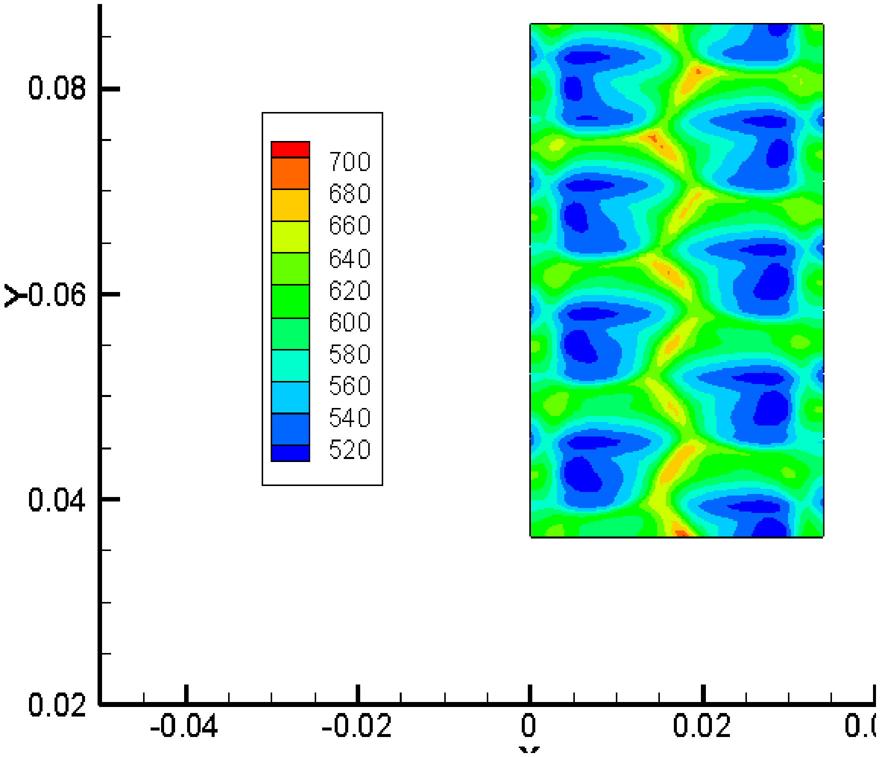

Figure 5-26 Contour of foil temperature (K) of the analysis rectangle

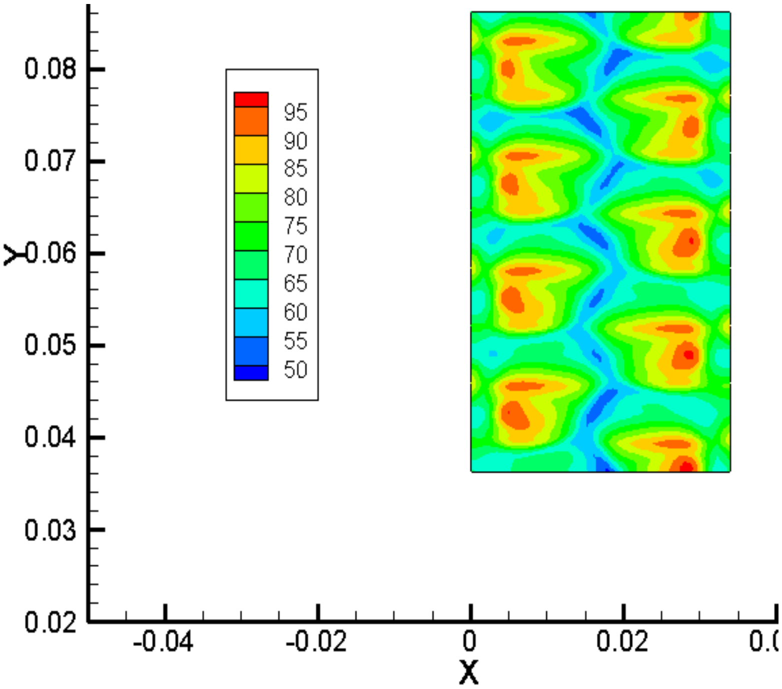

Figure 5-27 Contour of heat transfer coefficients (W/m^2-K) of the analysis box

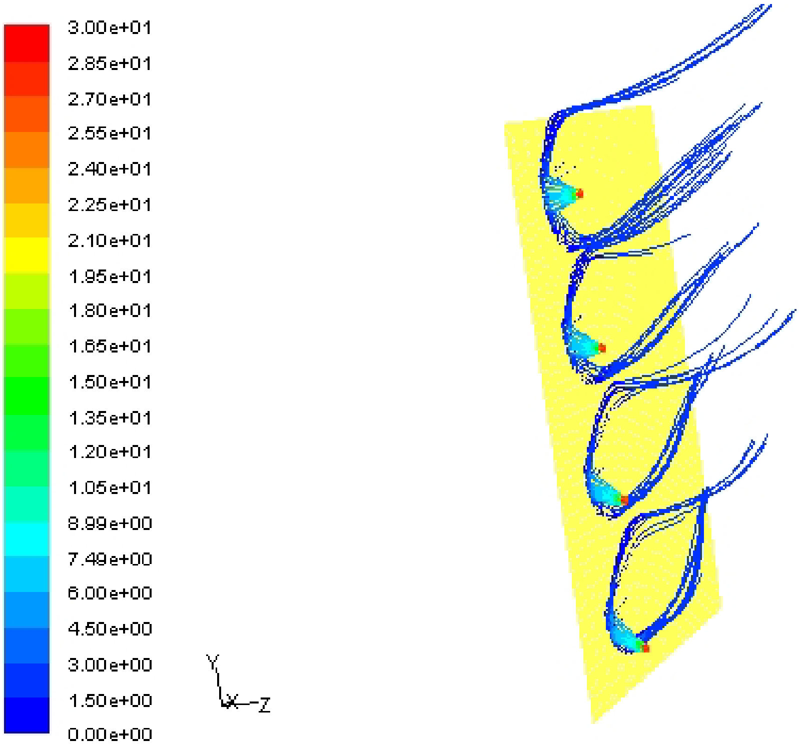

Figure 5-28 Predicted pathlines (colored by velocity magnitude) of the impinging jets

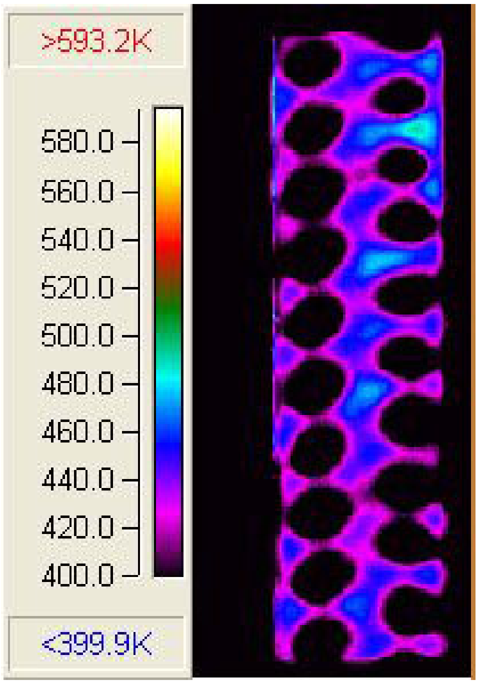

Figure 5-29 Experimental IR image

(ε=0.31, d=0.8 *mm*, V_{jet}=30.0 m/s, impinging distance: 1/8W)

CHAPTER 6

IMPINGING JET COOLING OF A HEATED SCALLOPED FOIL

6.1 Introduction

A new hibachi foil design was proposed and developed by the Naval Research Laboratory that utilized a scalloped-shape foil to improve the performance of the hibachi foil by minimizing the thermal and mechanical stresses resulting from rep-rate operation. Compared to the flat foil, the concave foil was pre-stressed during the installation and could better accommodate both the large pressure force applied on the foil by the laser gas and the thermal stress resulting from the large temperature rise in the foil due to e-beam attenuation. Numerical stress analysis showed reduced thermal and mechanical stress for the scalloped design under the projected rep-rate operating conditions (Aoyama, *et al.*, 2008). However, even with this improved design, the heating of the foil due to electron beam attenuation still raises the foil temperature above the allowable temperature limits. Hence, it is anticipated that an external cooling scheme would be necessary to effectively control the foil temperature during e-beam firing.

Impinging jet cooling has been shown to be able to effectively enhance convection heat transfer for the flat foil. Preliminary experiments also indicated that impinging jets also substantially reduced the temperature of a heated scalloped foil. This chapter summarized the experimental studies of impinging jet cooling for the scalloped hibachi foil under the simulated operating conditions of the Electra gas laser.

CFD simulations of impinging jet cooling for the scalloped foil are also summarized and discussed.

6.2 Experimental Studies of Impinging Jet Cooling of a Scalloped Foil

6.2.1 Experimental parameters

Similar to the impinging jet cooling for the flat foil, the heat transfer performance of cooling a scalloped foil is governed by those common parameters, mainly jet Reynolds number, jet-to-foil spacing, and impingement angles. The only difference lies in the shape of the foil: curved versus flat. To understand the extent of heat transfer enhancement resulting from the impinging jets, experiments were carried out by varying jet flow rate, jet-to-foil spacing, jet diameters and jet impingement locations. Detailed experimental parameters are summarized in Table 6-1, where the number shown in the impingement column represents the fraction of the foil width corresponding to the distance between the jet impingement location and the edge of the foil. As indicated by the numbers, two impingement locations were used so that jets were issued towards either the centerline of the foil or the edges of the foil. Three sets of jet tubes of different jet diameters were used with 51 holes on each set. Jet flow rates were chosen so that the jet Reynolds numbers overlapped for different jet diameters. A large number of experiments were carried out to cover the entire parameter range described in Table 6-1.

To characterize the heat transfer enhancement, the same data analysis was performed for only one portion of the cooled foil that covered about four impinging jets on the foil. Figure 6-1 shows the detailed impinging jet cooling scheme for the scalloped foil, where *L* is the distance traveled by the jet before impingement and *S* is the thickness of the spacer used in the experiments. The impingement locations and jet-to-foil spacing were adjusted by the combined effect of the spacer thickness and the rotation of the jet tube, with the angle of rotation pre-calculated and marked on the jet tube. A sample IR image is shown in Figure 6-2 for data analysis. For the analysis box, both minimum and average temperatures were extracted and the corresponding maximum and average heat transfer coefficients were calculated. The temperature and heat transfer coefficients were characterized as the functions of jet Reynolds numbers, jet-to-foil spacing, and impingement locations. These three variables completely characterized the heat transfer capability of impinging jets. .

Table 6-1 Experimental matrix of flat foil jet cooling

Jet diameter (mm.)	Spacer thickness (cm.)	Impingement distance	Jet velocity (m/s)	Re_d
0.8	0.13-0.50	1/2W, 1/8W	10	518
			20	1035
			30	1552
			40	2070
1.2	0.13-0.50	1/2W, 1/8W	10	1552
			20	2329
			30	2717
			40	3105
1.6	0.13-0.50	1/2W, 1/8W	10	1035
			20	2070
			30	3105
			40	4140

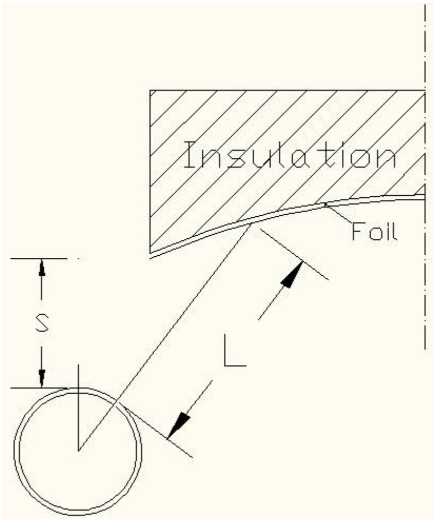

Figure 6-1 Schematic of impinging jet cooling for the scalloped foil

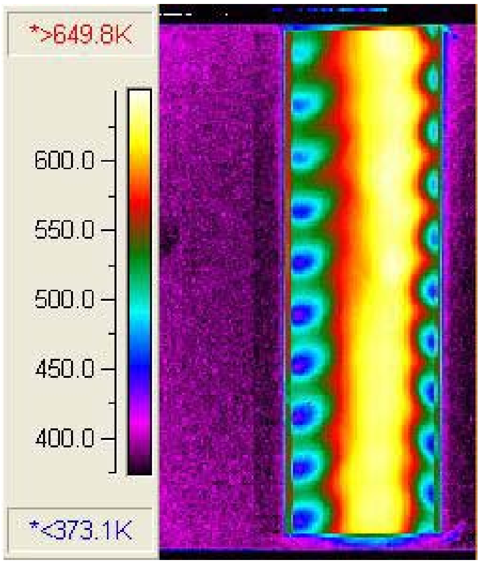

Figure 6-2 A typical IR thermal image for data analysis (white rectangular box)
(V_{jet}=10.0 m/s, d=1.2 mm, Impinging distance: 1/8W, Spacer thickness= 1.27 mm)

6.2.2 Summary of experimental results

A total of 96 experiments were carried out which produced 96 distinctive IR thermal images, each of which represented a separate set of experimental parameters. For each image, the maximum and average heat transfer coefficients and corresponding Nusselt numbers in the analysis box were calculated. It was shown previously in Chapter 5 that for a flat foil, the Nusselt numbers depend only on the Reynolds numbers, jet-to-foil spacing, and jet impingement locations. However, the scalloped foil has a curved shape, which in turn affects the performance of impinging jet cooling. Before the jet was turned on, average heat transfer coefficient resulted from the fan-driven flow was first determined to be 61.5 W/m^2-K in the analysis box serving as the reference value for heat transfer enhancement from impinging jet.

The same method was applied to correlate the experimental data as the one for the flat foil cooling. At the impingement distance of 1/8W with an impingement angle at 33.5°, the stagnation Nusselt number was correlated using multi-variate regression fitting and took the following form,

$$Nu_{d,\max} = 0.0553\exp\left(-0.0631 L/d\right) Re_d^{0.8818} Pr^{1/3} \qquad \text{(Eq. 6-1)}$$

where

$$Nu_{d,\max} = \frac{h_{\max} d}{k} \qquad \text{(Eq. 6-2)}$$

$$Re_d = \frac{\rho_{jet} V_{jet} d}{\mu} \qquad \text{(Eq. 6-3)}$$

The correlation took into account both the effects of jet-to-foil spacing and

Reynolds numbers. Figures 6-3 and 6-4 compare the correlation and the experimental data in collapsed forms, with jet Reynolds number and jet-to-foil spacing as the independent variables, respectively. The correlation is shown to be capable of predicting most of the experimental data within ±20% agreement.

Besides the stagnation Nusselt numbers that are useful for the validation of the experiments, the average heat transfer enhancement of the scalloped foil is also very important to the designers of electron-beam pumped gas lasers, which helps prolong the lifetime of the hibachi foil. The average Nusselt numbers from the experiments were also correlated into the same form as a function of jet Reynolds number and jet-to-foil spacing. By applying the same multivariate regression fitting method, a correlation for the average Nusselt number was obtained for jets impinging near the edge (1/8 foil width),

$$Nu_{d,avg} = 0.0196\exp\left(-0.0571L/d\right)Re_d^{0.9351}Pr^{1/3} \qquad \text{(Eq. 6-4)}$$

Figures 6-5 and 6-6 plot the correlations together with the experimental data in collapsed forms as functions of jet Reynolds number and jet-to-foil spacing, respectively. The plots indicate that the correlation is able to predict the experimental results within reasonable agreement. The correlations for maximum and average Nusselt numbers both show that Nusselt numbers are very sensitive to the jet-to-foil spacing due to its exponential dependence, with the average Nusselt number decreases at a slower rate with increasing jet-to-foil spacing.

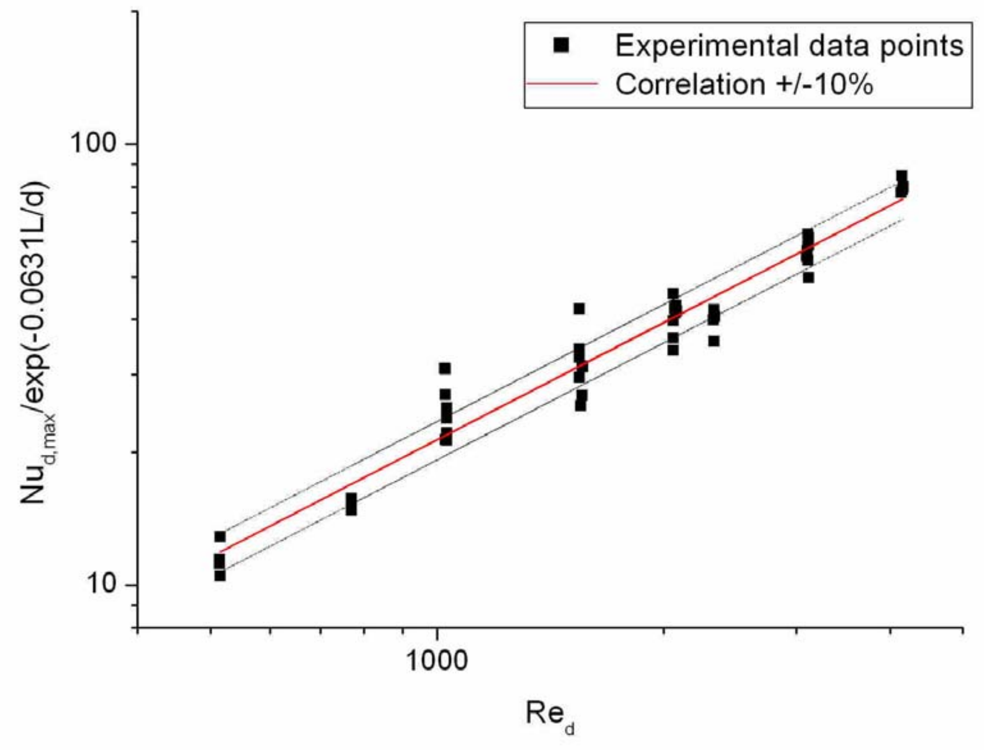

Figure 6-3 Comparison between experiments and the correlation for Nusselt numbers

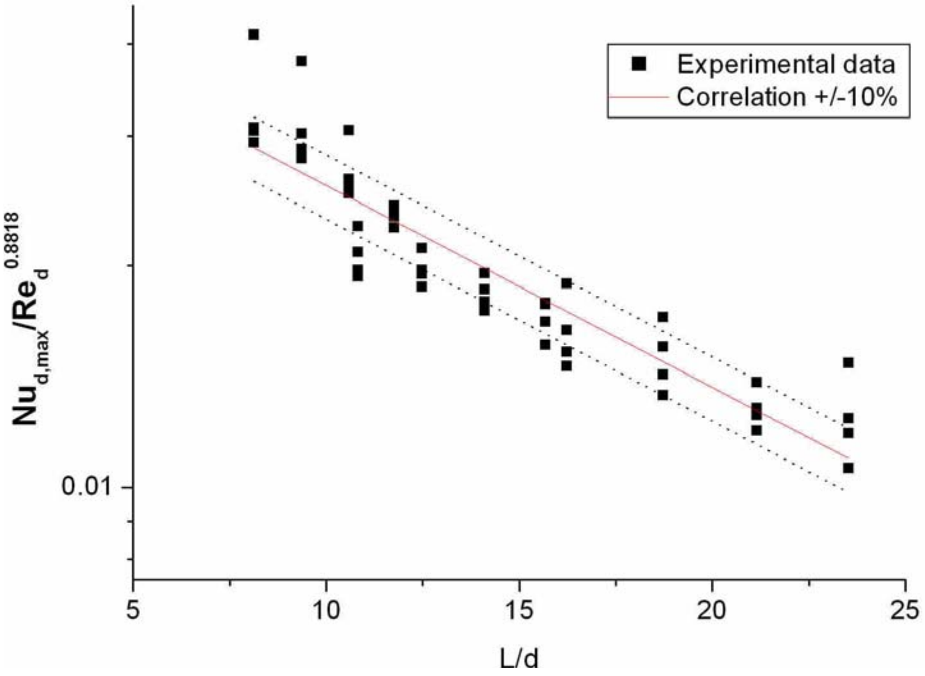

Figure 6-4 Comparison between experiments and the correlation for maximum Nusselt numbers

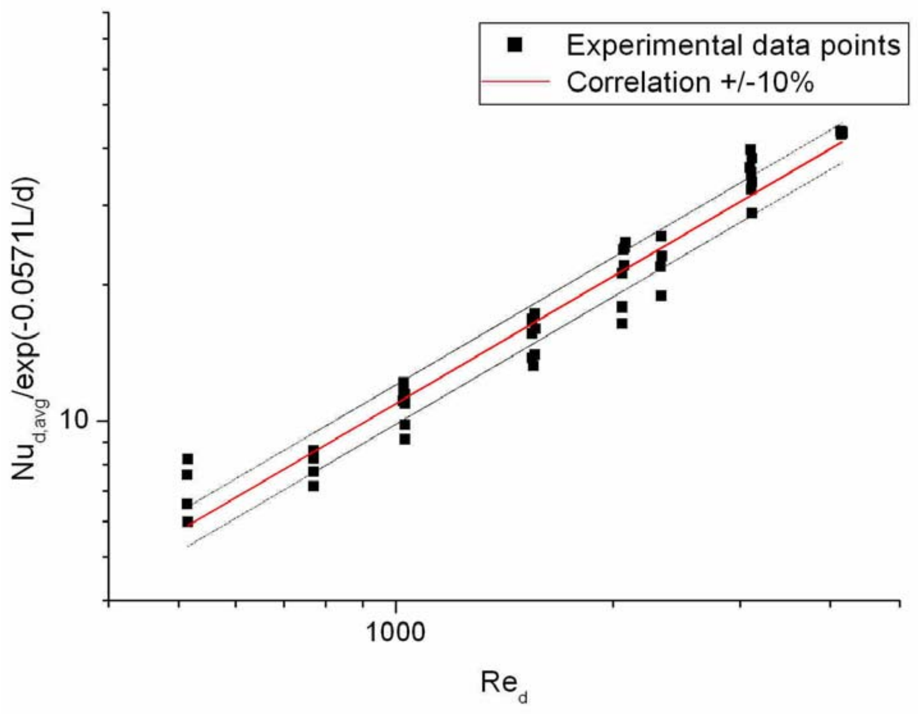

Figure 6-5 Empirical correlation of average Nusselt numbers

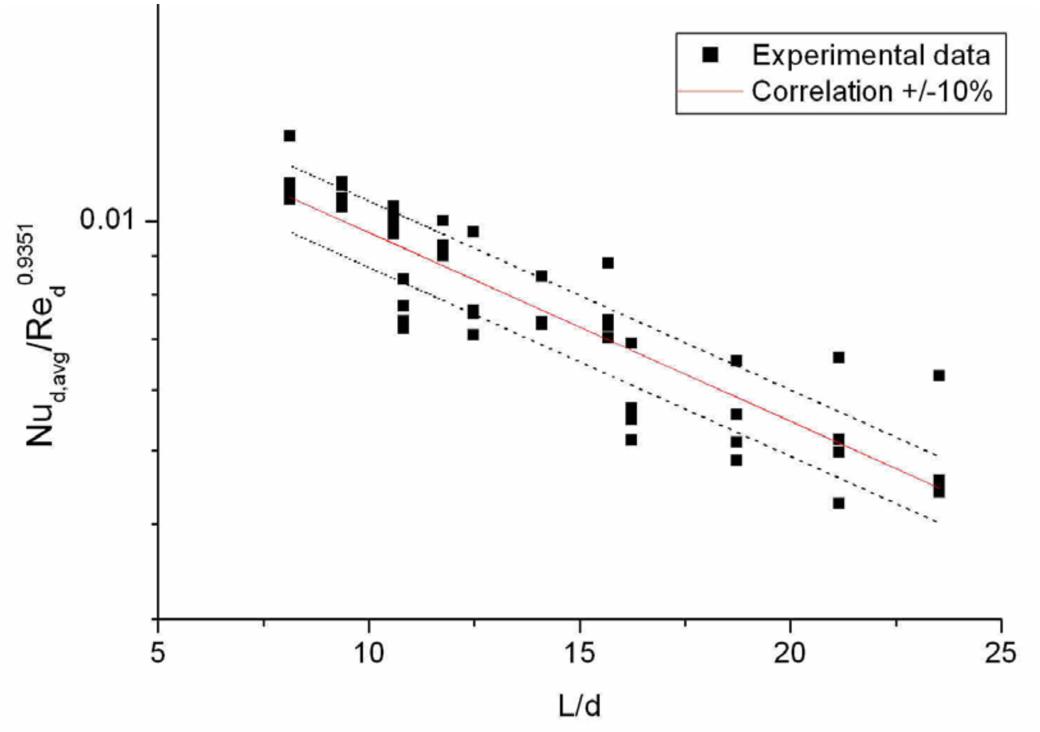

Figure 6-6 Empirical correlation of average Nusselt numbers

6.2.3 Effect of the foil curvature

The scalloped foil design was proposed in an aim to reduce both the mechanical and thermal stress within the foil resulting from the rep-rate operation of the gas laser. With the application of impinging jet cooling, the scalloped foil was better protected from the e-beam attenuation. The same jet supply system as the one for the flat foil, including the jet tubes and the jet configuration, was used. The only difference is that at the same spacer thickness, the jet-to-foil spacing for the scalloped foil is larger than the one for the flat foil due to the concave shape of the scalloped foil. The different shape also makes the impact angle larger for the flat foil than for the scalloped foil when the jets impinge on the same locations. The change in the experimental parameters resulted in different heat transfer coefficients in the two different schemes of impinging jet cooling.

Figure 6-7 compares the experimental average Nusselt numbers for the jets of 1.2 mm diameter impinging on the vertical lines 1/8 width of the foil from the edges for both the flat foil and the scalloped foil. The data indicate that the Nusselt numbers were much larger for the flat foil than the scalloped foil at the same jet flow rate (or Reynolds number). This was due to the fact that the actual jet-to-foil spacing for the scalloped foil was larger than the flat foil resulting from the concave surface of the scalloped foil and the exponential dependence of Nusselt numbers on the jet-to-foil spacing. The comparison indicates that it is desirable to reduce the jet-to-foil spacing in the actual hibachi foil cooling in e-beam pumped gas lasers to achieve high heat transfer enhancement for the foil.

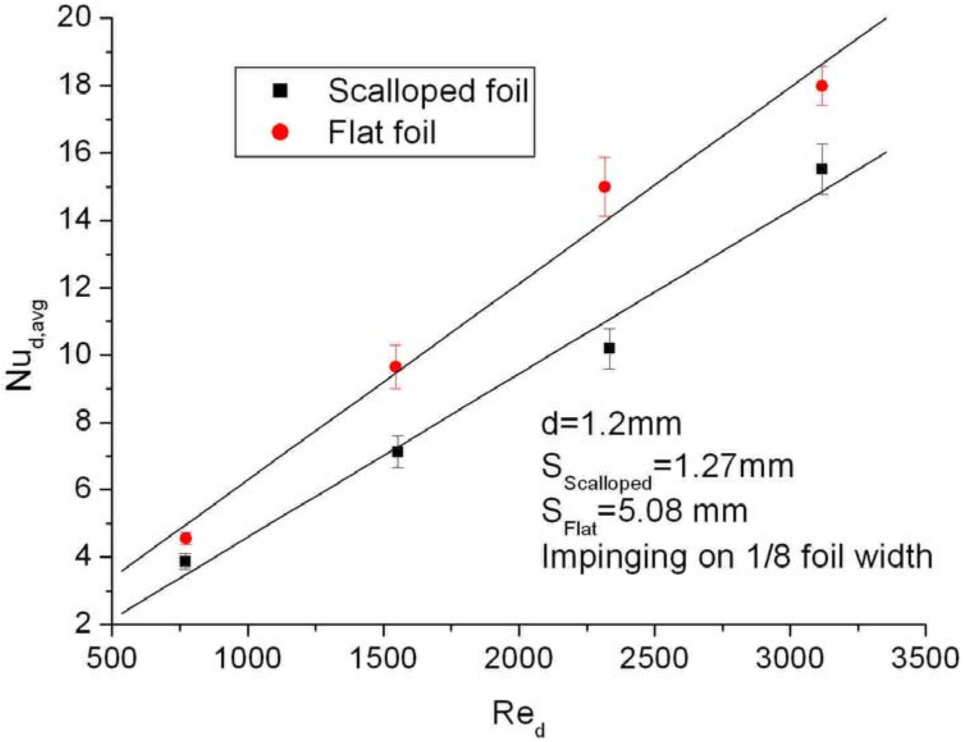

Figure 6-7 Effect of the curvature of the foil on heat transfer capability of impinging jets

6.2.3 Effect of jet Reynolds number

One of the purposes of this investigation was to identify the appropriate jet flow rate required for the foil cooling during the nominal rep-rate operation of the gas laser. The experimental results helped reveal the minimum jet flow rate required to control the foil temperature under the imposed temperature constraints. On the other hand, the requirement of laser efficiency also sets a limit on the available power for foil cooling, which in turn restricts the allowable pumping power for the jets.

Figure 6-8 shows the stagnation Nusselt numbers for three different jet diameters as a function of jet Reynolds numbers, which show that higher jet Reynolds numbers result in higher heat transfer coefficients in a linear trend for the range of Reynolds number involved.

The average heat transfer coefficients for the foil provide the detailed information about the overall heat transfer enhancement. Figure 6-9 shows the average Nusselt number as a function of Reynolds number for the same cases as above. Compared to the maximum plots above, the average plot shows a slower rate of increase with Reynolds numbers and lower Nusselt numbers. The results will suggest the selection of appropriate jet flow rate for the actual foil cooling on Electra under the constraint of available pumping power. As indicated in Figures 5-13 and 5-14, pressure drop in the jet supply system increases as a second-order function of Reynolds number. For smaller jet diameters, the rate of increase is much higher than the one for large jet diameters.

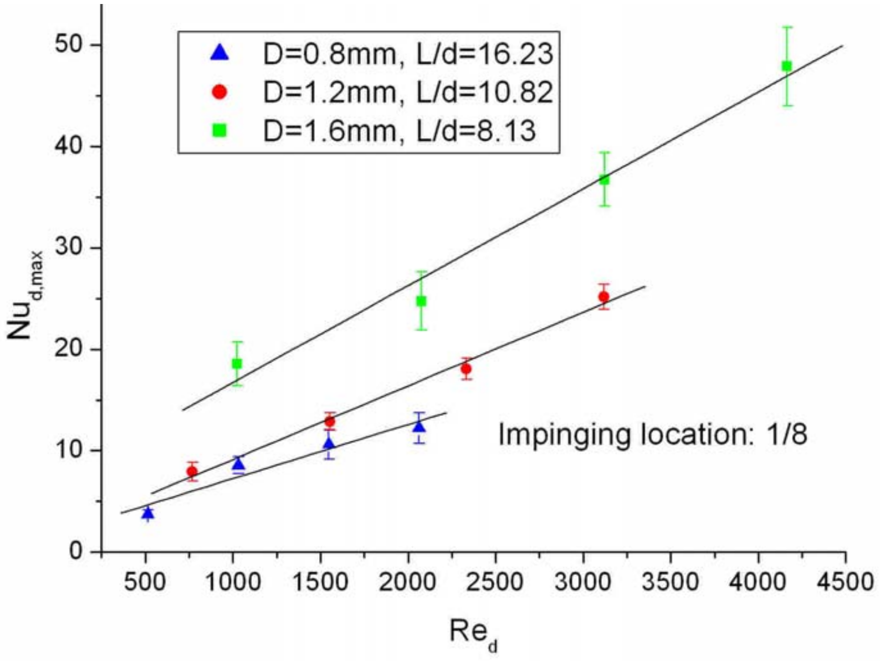

Figure 6-8 Maximum Nusselt number of impinging jet cooling for the scalloped foil

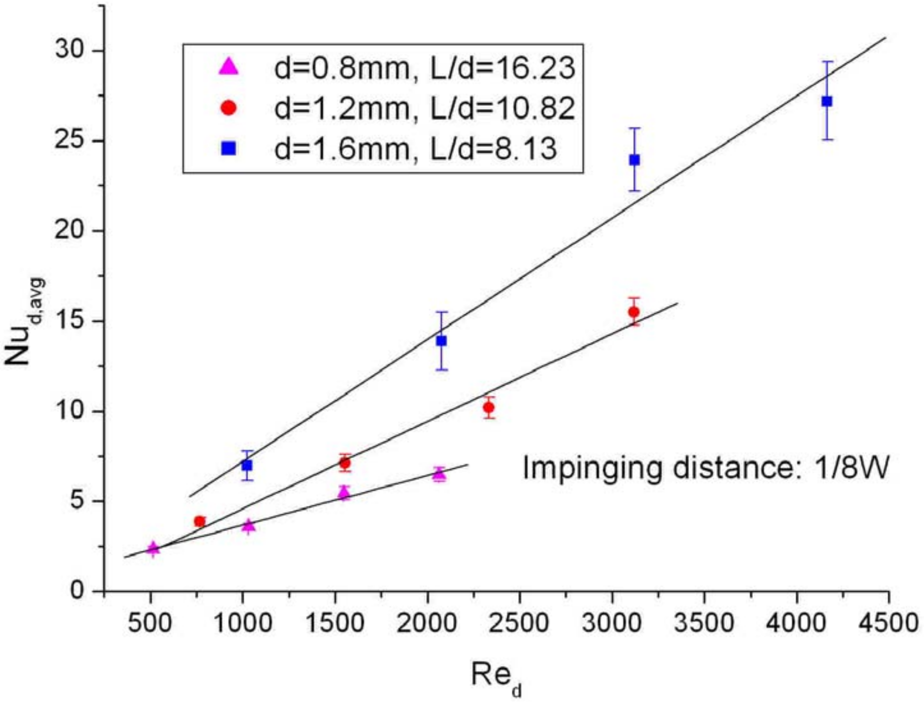

Figure 6-9 Average Nusselt number of impinging jet cooling for the scalloped foil

6.2.4 Effect of jet-to-foil spacing

As shown in the correlation (Eqs. 6-1 and 6-4), both the maximum and average Nusselt numbers were exponentially dependent on the normalized jet-to-foil spacing with negative coefficients, which indicated that increasing the spacing would significantly decrease the heat transfer coefficients. Figure 6-10 shows the stagnation Nusselt number at various jet-to-foil spacing values for the jet diameter of 1.2 mm and jets impinging on the 1/8*W* location. It was interesting to note that the Nusselt numbers decreased at a much slower rate than the one for the flat foil. This might be explained by examining the range of jet-to-foil spacing in these two cases. The range of *L/d* was 7.3-11.7 for the flat foil and 10.8-15.7 for the scalloped when the same jet diameter and the same spacer thickness were considered. At the smaller values of jet-to-foil spacing, Nusselt number was more sensitive to the spacing than at the larger values. This was also apparent in the exponential coefficient, where the correlation for the flat foil had a more negative value (-0.0994) than the one for the scalloped foil (-0.0631).

Figure 6-11 also shows the average Nusselt number at various jet-to-foil spacing and jet Reynolds numbers for the jet of 1.2 mm. Compared to the plot of the stagnation Nusselt number, the average plot showed a much smaller rate of change as the jet-to-foil spacing increased, with the smallest value producing the best overall cooling performance.

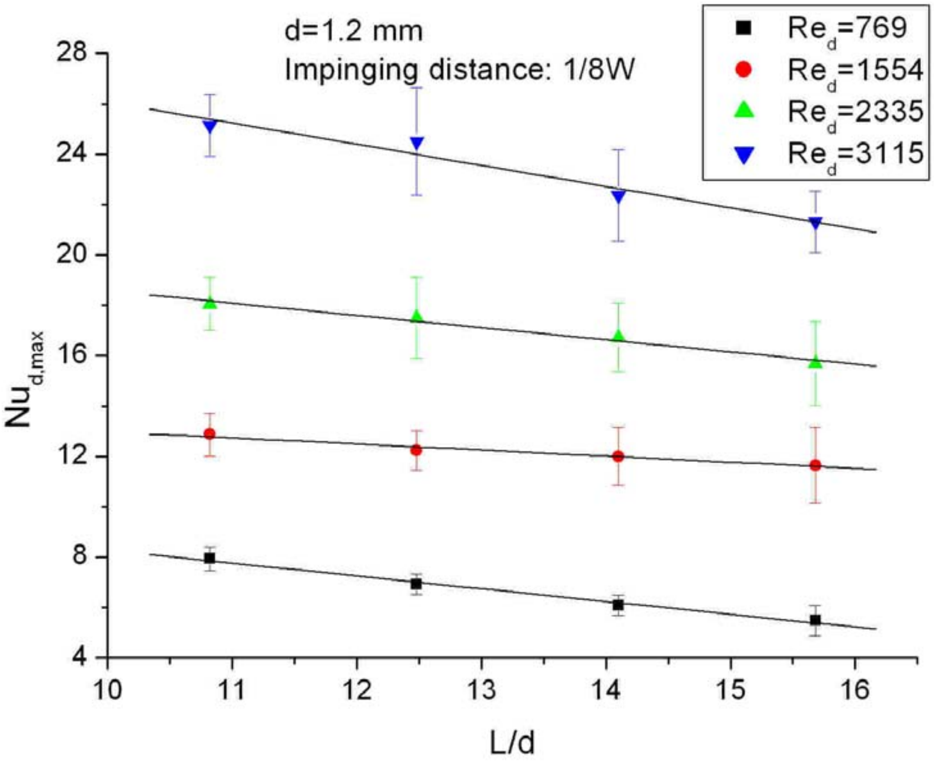

Figure 6-10 Maximum Nusselt number at different jet-to-foil spacing (d=1.2 mm)

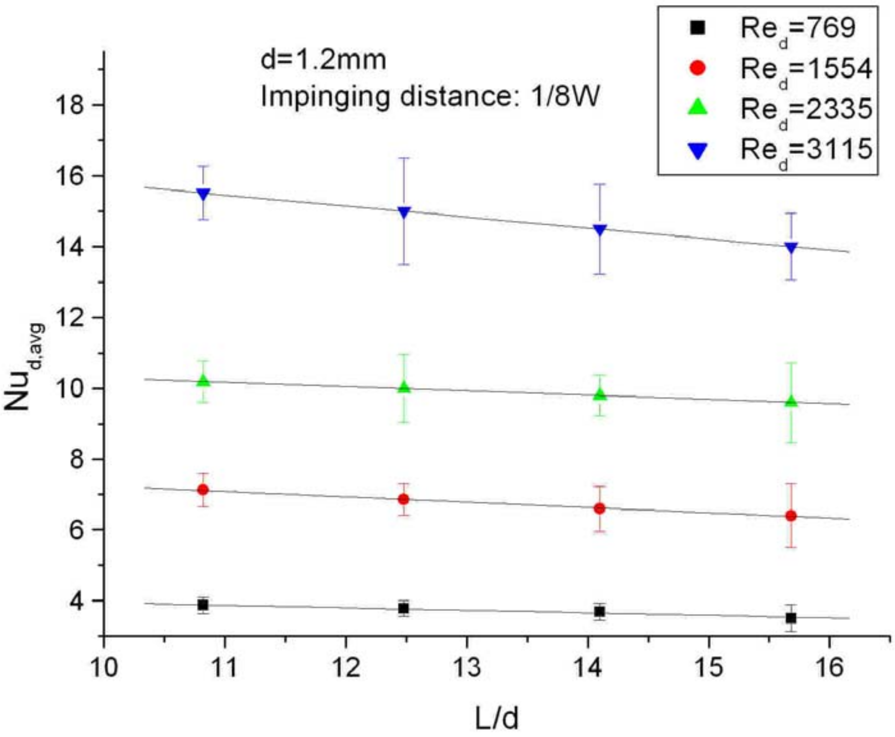

Figure 6-11 Average Nusselt number at different jet-to-foil spacing (d=1.2 mm)

6.2.5 Effect of jet impinging location on the foil

Experiments were performed to investigate the effect of different impinging locations on the performance of foil cooling to identify the best configuration for foil cooling. Jets were aligned to impinge on the foil either very close to the edges or the centerline of the foil. These cases offered a direct comparison of the cooling performance for the two limiting jet issuing configurations. The configuration with jets impinging on the edges of the foil had shorter flow path before impingement than the one with jets directed to the centerline of the foil, while the latter was expected to have bigger spread due to the expansion of the jets after exiting the jet tubes. The average heat transfer characteristics for the above cases would help to identity the better configuration for the actual foil cooling in the gas lasers.

Figure 6-12 shows the average Nusselt number for two different impinging locations for the jet diameter of 1.2 mm and the same spacer thickness of 1.27 mm. The case with jets impinging on the edges produced higher heat transfer enhancement than the one with jets aimed at the foil centerline at the same jet Reynolds number. This was because of the dominance of jet-to-foil spacing in determining the heat transfer capability. The average Nusselt numbers for jets impinging on the edges increased by approximately 300% when jet Reynolds number increased from ~770 to ~3100, while the average Nusselt numbers increased only ~200% for the same jet Reynolds number range.

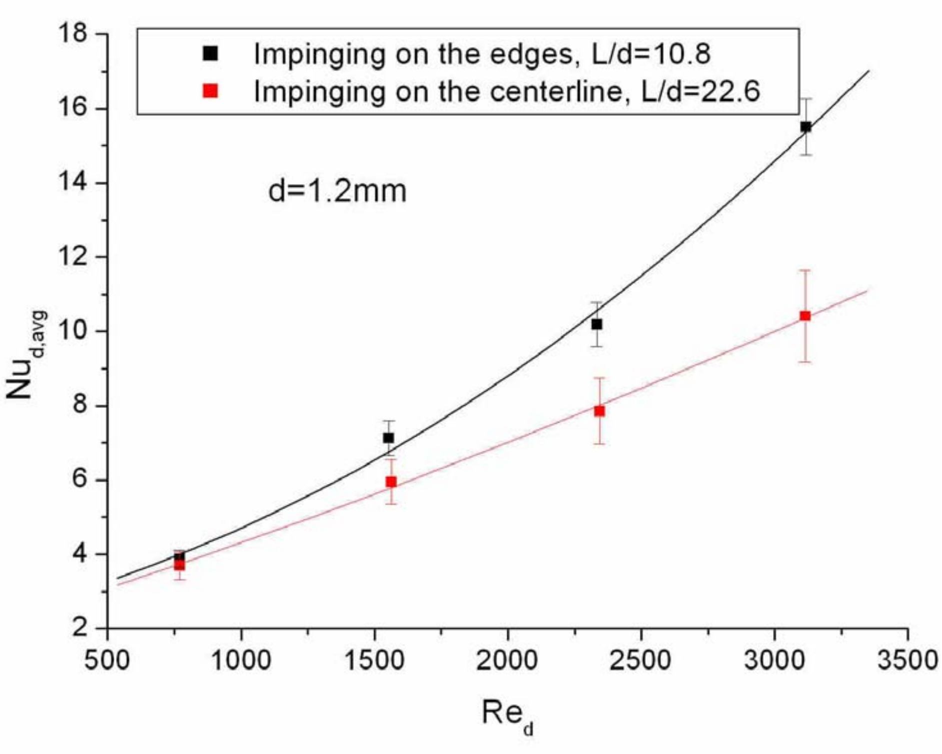

Figure 6-12 Comparison of average Nusselt number at different impinging locations

6.3 CFD Studies of Impinging Jet Cooling for a Scalloped Foil

6.3.1 Model geometry

CFD simulation of impinging jet cooling for a scalloped foil also requires a three-dimensional model due to its three-dimensional flow distribution. The large ratio between the bulk flow area and the small jet area also presents a challenge in the modeling to generate as few highly skewed cells as possible.

A simplified three-dimensional model was created in GAMBIT® for CFD simulations using FLUENT®, which included the following simplifications similar to those applied for modeling the flat foil,

- The geometry of the model had a smaller bulk flow area and a shorter foil length than the actual flow channel to decrease computational demands;
- A total of 20 interlacing jets were modeled with ten jets on each side;
- The impinging jets were modeled as issuing in specified orientations at the same velocities from circular openings on two vertical side surfaces at the specified mass flow rate;
- The foil was modeled as a concave wall under constant surface heat flux set at the estimated value removed by convection heat transfer;
- The bulk flow was simulated by imposing an inflow with a uniform velocity profile.

Figure 6-13 shows the parallelepiped model created using GAMBIT® that is used for CFD simulations in FLUENT®. The model is 12.5 cm high, 4.1 cm long and

4.0 cm deep. Jets are evenly spaced at 1.25 cm on two sides.

The meshing of the model needs to resolve the definition of a jet of very small area, which requires a relatively large number of nodes to be used. A total of 721,600 cells are generated for the reduced 3D model. A close-up of the meshing near the jet is shown in Figure 6-14. An unstructured mesh similar to the one for flat foil cooling was generated for the jet surface to provide good resolution for the area in the vicinity of the jet exit. The meshing of the 3D model is performed by sweeping horizontally between two side walls and generating a regular grid of hexahedral elements, which helps improve the speed of convergence in the simulations.

6.3.2 Boundary conditions

The main boundary conditions used in the steady-state CFD simulations in FLUENT® are specified as follows,

- q'': The uniform surface heat flux specified at the foil surface (determined from the heat input, kW/m^2).
- $\dot{m}_{in}$: The mass flow inlet at the jet exit with appropriate orientations (kg/s).
- T_{in}: The air temperature in the inlet flow (^{o}C).
- h_{conv}: The convection heat transfer coefficient for the heat loss from the model to the surroundings due to natural convection (W/m^2-K).

Most of the boundary conditions are based on their respective experimentally measured typical values, with the convection heat transfer coefficient estimated from natural convection correlations for vertical walls. In addition to the boundary conditions, air is used in all the simulations and is regarded as an ideal gas for compressible flow simulations.

6.3.3 Simulation results and discussions

CFD simulations performed in the current investigations use a simplified 3D model plus simplified boundary conditions, so it is not surprising that the results from these simulations deviate substantially from the current experimental results. The purpose of the CFD simulations is to show that CFD tools can predict the essential heat transfer characteristics of impinging jet cooling. In the simulations, the jet orientation is adjusted so that the impingement locations are the same as in the experiments. The mass flow rates of the jets, the bulk flow, and the surface heat flux of the foil are set to the corresponding experimental values. Also, the second-order upwind differencing scheme is applied for solving continuity, momentum energy, turbulence kinetic energy, and turbulent dissipation rate equations for a more accurate solution. The convergence criteria for all the variables, i.e. the residual limits, are set at 1e-6 for the energy equation and 1e-3 for all the other equations.

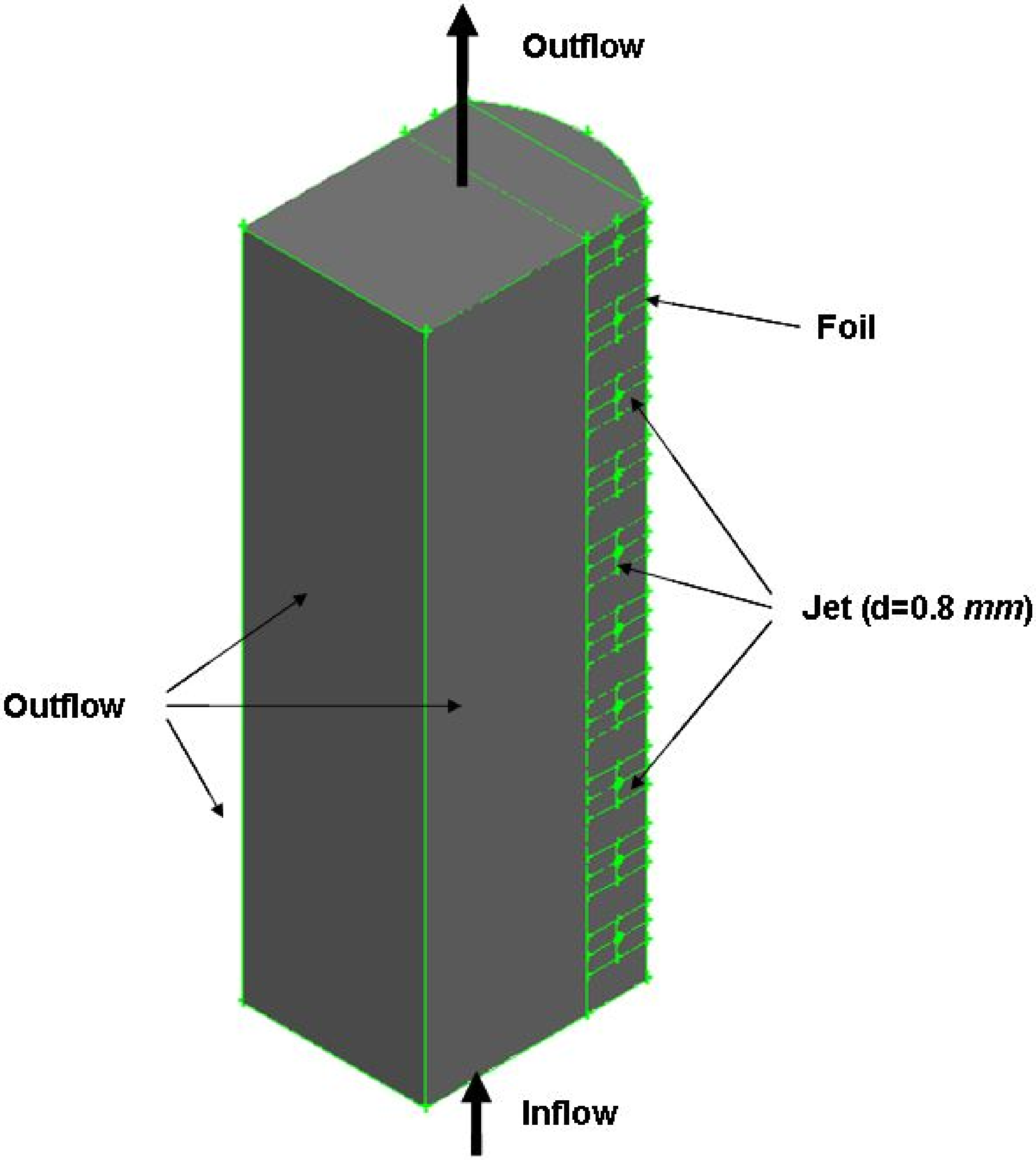

Figure 6-13 CFD model for impinging jet cooling for the flat foil

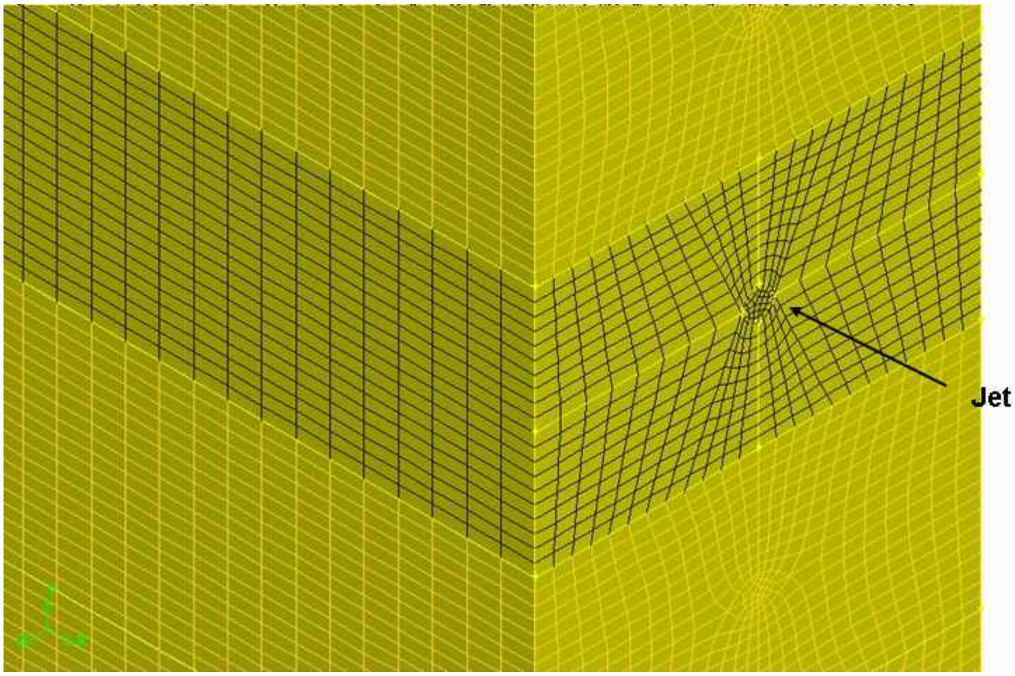

Figure 6-14 Close-up of the computation grid for impinging jet cooling for the flat foil (29 unstructured elements were generated for the jet for a good resolution)

In the simulation, air jets of 0.8 mm diameter and 30.0 m/s are aimed to impinge on the foil at an impinging distance of 1/8W and a spacer thickness of 0.5cm, which corresponds to the non-dimensional jet-to-foil spacing of 8.8. The bulk flow was imposed at the inlet of the model. The surface heat flux at the foil is set at 20.0 kW/m^2, which is a typical experimental value used.

As for the modeling of impinging jet cooling of a flat foil, the realizable *k*-*ε* turbulence model with non-equilibrium wall function was used in the simulation, which was suggested in the FLUENT® manuals for impinging jet modeling (Shih, et. al., 1995). This modified turbulence model incorporates a new formulation for the turbulent viscosity and a new transport equation for the turbulent kinetic energy dissipation rate (*ε*) that was derived from the exact formulation for the transport modeling of the mean-square vorticity fluctuation. This model offers an immediate benefit in more accurately predicting the spreading of the impinging jets. For near-wall treatment in the simulations, the non-equilibrium wall functions were invoked, which is based on a two-layer concept to compute turbulent kinetic energy in the near-wall cells and can partly account for the non-equilibrium effect that is neglected in the standard wall function (Kim and Choudhury, 1995). The non-equilibrium wall functions are suggested to be used in complex flows where the mean flow and turbulence changes rapidly, such as in the impingement zone of an impinging jet.

In the simulation, jets of 0.8 mm diameter are issued to impinge on the foil at the impinging distance of 1/8W, which correspond to the non-dimensional jet-to-foil spacing of 11.7. Figure 6-15 shows the contour of the foil temperature, in which there is a strong periodic behavior in the distribution of foil temperature. However, the area near the channel inlet is strongly affected by the boundary condition and model geometry (the bottom and top jets are too close to the inlet and outlet). To illustrate the jet impinging cooling characteristic, the plot was restricted to four jets located on the jet row on each side to reduce the entrance effects on the simulation results, which corresponded to a smaller foil area for analysis (3.4 cm wide and 5 cm high, black dotted area in Figure 6-15).

Figures 6-17 and 6-18 show the contours of foil temperature and heat transfer coefficients of the analysis rectangle, respectively. Areas of hot spots are found to be near the centerline of the foil. The maximum and average heat transfer coefficients are 151.3 and 55.8 W/m^2-K, respectively. However, the contours do not show the regular elliptic shape of spread, but shows a distorted shape. The predicted heat transfer characteristics are closely related to the jet flow distribution upon impingement. Figure 6-18 shows the pathlines of the jets coming out of the left row of holes before and upon impingement. It clearly shows that the jet first spread out before impingement and is diverted upwards by the cross flow that causes the distortion in the heat transfer characteristics upon impingement.

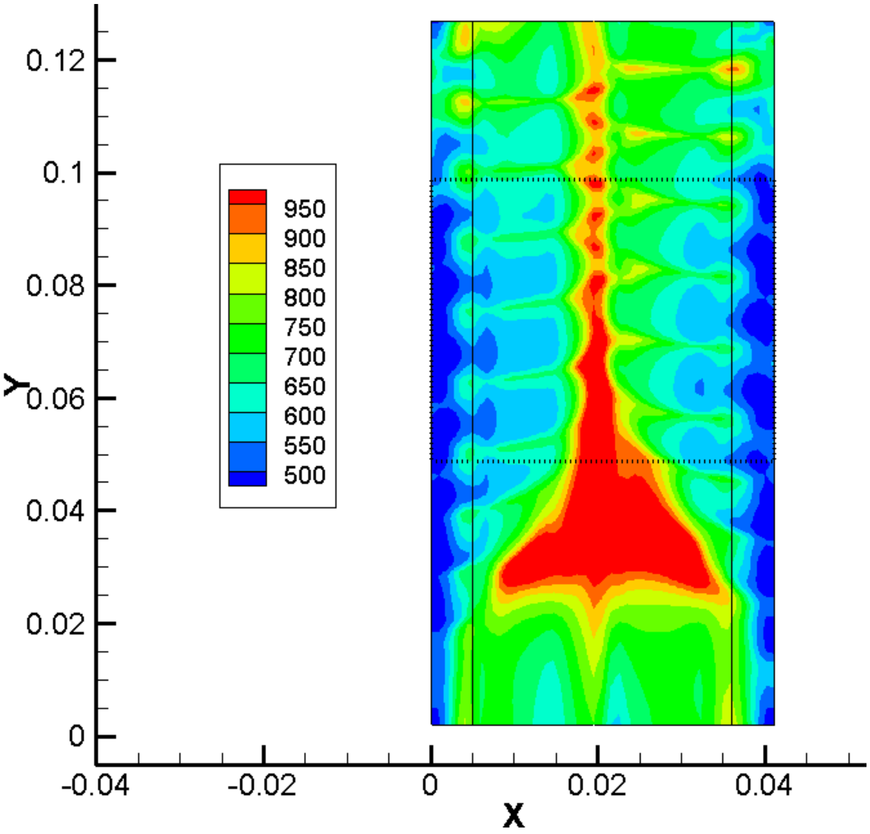

Figure 6-15 Simulated foil temperature contour (K)

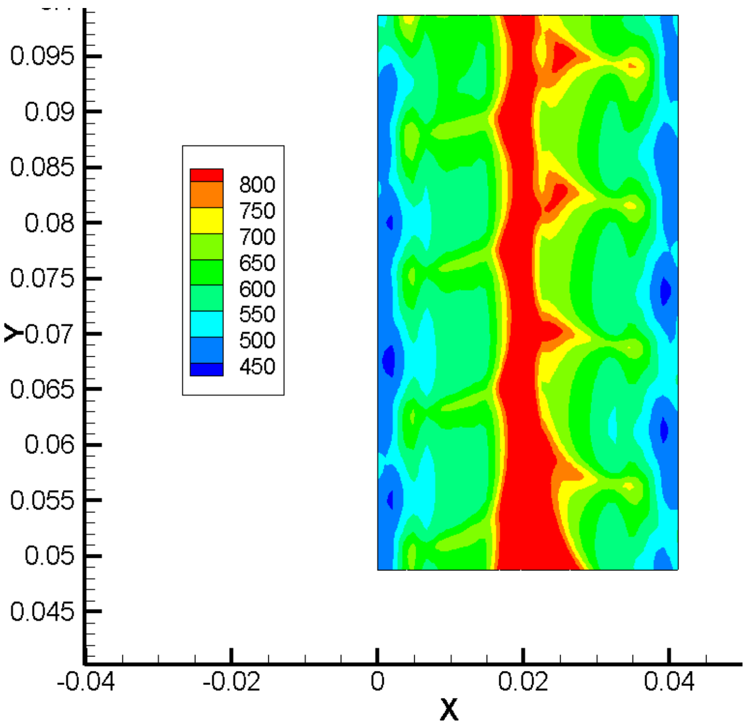

Figure 6- 16 Contour of foil temperature (K) of the analysis rectangle

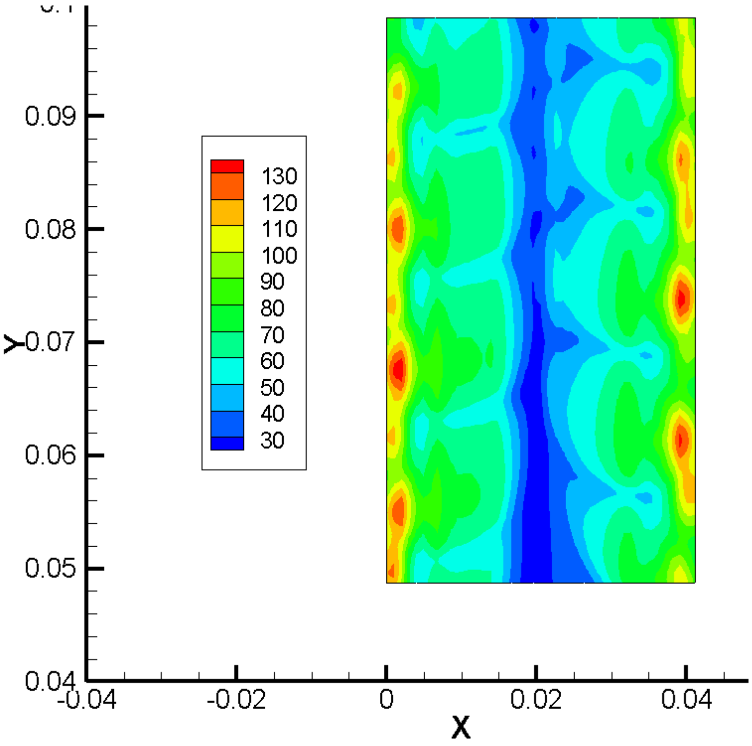

Figure 6-17 Contour of heat transfer coefficients (W/m^2-K) of the analysis box

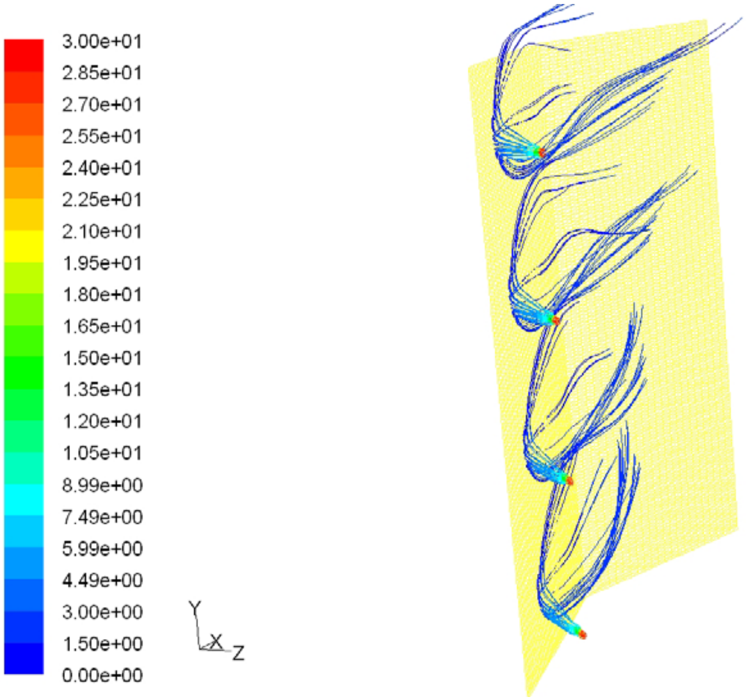

Figure 6-18 Predicted pathlines (colored by velocity magnitude) of the impinging jets

An experimental obtained IR image with similar parameters is also shown in Figure 6-19. Compared to the simulated temperature contour, the CFD model is able to predict a similar pattern of temperature distribution but different temperature values. This is because this model is much smaller in size than the actual experimental setup and less heat can be dissipated or transferred to the ambient, which produces higher foil temperatures even the same surface heat flux is used in the simulations.

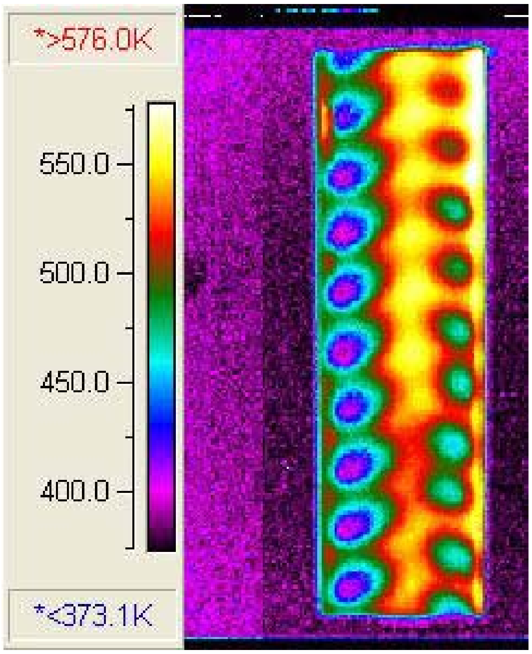

Figure 6-19 Experimental IR image

(ε=0.31, d=0.8 *mm*, V_{jet}=30.0 m/s, V_{∞}=4.0 m/s, impinging distance: 1/8W)

CHAPTER 7

CONCLUSIONS AND RECOMMENDATIONS

This chapter summarizes the conclusions drawn from the experimental and numerical investigations of gas laser hibachi foil cooling using both tangential and impinging near-wall jets. Recommendations for future work are also presented.

7.1 Conclusions

This dissertation research proposed and investigated an effective and feasible forced-convection cooling scheme using near-wall high speed jets for the hibachi foil in gas lasers. This foil serves as the transmission foil for the electron beam. The research was motivated by the necessity of identifying a reliable and cost-effective way to protect the transmission foil from the induced thermal load resulting from attenuation of a high energy, high intensity electron beam passing through the foil. Two types of jets (tangentially planar and circular impinging) were investigated for two types of foil design (flat and scalloped). The purpose of this dissertation research was to experimentally and numerically show the efficacy of cooling a heated metal foil using near wall jets that were injected locally.

The main conclusions to be conveyed to the Electra designers are,

1) Planar jet is inappropriate for the hibachi foil cooling;

2) Impinging jets should be placed as close as possible to the foil with impact

point as close as possible to the rib edge;

3) While scalloped foils may be advantageous from a stress analysis standpoint, the scalloped geometry will result in lower heat transfer coefficients, hence higher temperatures.

7.1.1 Flat foil cooling with a planar Jet

The method of tangentially injecting a planar jet was first proposed to effectively cool the hibachi foil. Various jet flow rates and surface heat fluxes were examined experimentally and numerically.

A 1.0 mm-thick 3.4 cm-wide near-wall parallel planar jet at various velocities was superimposed upon a main recirculating laser gas flow to provide additional convection heat transfer capability for the foil strip that represents the actual geometry of the hibachi foil between ribs. Foil temperature profile was measured and heat transfer coefficients were obtained to characterize heat transfer enhancement resulting from the planar jet injection.

Experimental results show that heat transfer rates from the foil to the gas flow were significantly enhanced with the injection of a planar jet. Near the leading edge, the heat transfer coefficient for a jet at 50.0 m/s is about twice the value for a jet at 25.0 m/s and four times the magnitude when only the main stream flow of ~4.0 m/s is present and the jet is turned off. Experimental results also show that heat transfer coefficients quickly decay downstream from the injection point, which results in much higher temperatures in the upper portion of the foil than in the lower portion when a constant surface heat flux is applied. This observation indicates that more injection points are needed downstream from the first point to offer better cooling performance for the entire foil. However, this would interfere with the e-beam. Thus, a single planar jet located at the bottom edge of a foil is not suitable for the application.

Experimental results were well correlated with the recommended forms from the literature. The correlation has good agreement with the experiments and can be used to predict the heat transfer enhancement for the entire foil from planar jet injection. CFD simulations were also performed. The two-dimensional model was validated by comparing the heat transfer coefficients, which indicates the standard and RNG k-ε turbulence models are applicable in the modeling of near-wall planar jets.

7.1.2 Flat foil cooling with impinging jets

Jet impingement cooling was proposed as an alternative cooling scheme for the flat hibachi foil. Impinging jets were arranged to cover the entire surface of the foil, so that the foil was cooled over its entire surface. The experimental studies used two parallel jet tubes issuing discrete circular jets obliquely towards the foil, which covered the foil lengthwise in a staggered fashion. A wide range of jet velocities, jet-to-foil spacing, and jet impingement locations/angles were examined to explore the heat transfer enhancement associated with the impinging jets.

Nusselt numbers obtained from the experiments were shown to increase with jet Reynolds number approximately following the trend of a power function. Nusselt numbers were also shown to be very sensitive to the variation of jet-to-foil spacing, where a slight increase in the spacing reduced Nusselt numbers significantly. The header tubes were also adjusted so that jets impinged on the foil at various locations. Experimental results showed the foil was better cooled when the jets impinged on the edges of the foil due to shorter jet-to-foil spacing and the forward spread of the jet.

Both stagnation and average Nusselt numbers obtained from the experiments were correlated empirically using the same formulae existing in the literature. The correlations were able to predict the experimental results within 20%.

CFD simulations were also performed using a simplified three-dimensional model for impinging jet cooling for the flat foil. The simulation results show that the CFD tools were able to predict the essential heat transfer and flow characteristics of the impinging jet cooling for a heated flat foil, with a qualitative agreement observed..

7.1.3 Scalloped foil cooling with impinging jets

The scalloped hibachi foil was proposed and developed to improve the performance of the foil by reducing the thermal and mechanical stresses under the rep-rate operation conditions. Jet impingement cooling was explored as an active cooling scheme for this new hibachi foil design. Impinging jets were arranged in a fashion to cover the entire surface of the foil. The experimental studies used two parallel jet tubes that issued two rows of discrete circular jets obliquely towards the foil, which covered the foil lengthwise in a staggered fashion. A wide range of jet velocities, jet-to-foil spacing, and jet impingement locations/angles were examined to explore the heat transfer enhancement associated with the impinging jets.

Nusselt numbers obtained from the experiments were shown to increase with jet Reynolds number approximately following the trend of a power function. As in the cooling of the flat foil, Nusselt numbers were also shown to be very sensitive to the variation of jet-to-foil spacing, where a slight increase in the spacing reduced Nusselt numbers significantly. Jet tubes were also adjusted so that jets impinged on the foil at various locations. Experimental results showed the foil was better cooled when the jets were made to impinge on the edges of the foil due to shorter jet-to-foil spacing and the forward spread of the jet.

Both stagnation and average Nusselt numbers obtained from the experiments were correlated empirically using the same formulae existing in the literature. The correlations were able to predict the experimental results within 20%.

CFD simulations were also performed using a simplified three-dimensional model for impinging jet cooling for the scalloped foil. The simulation results show that the CFD tools were able to predict the essential heat transfer and flow characteristics of the impinging jet cooling for a heated scalloped foil, with a qualitative agreement observed.

7.2 Recommendations for Future Work

This investigation involved the measurement of a large number of experimental quantities and used various measurement techniques. The experimental measurements can be improved and extended by the following suggestions:

- Impinging jets were produced through the circular openings on two jet tubes, which had a thin wall and relatively long length. Header tubes with larger hydraulic diameters will help produce more uniform jet flow rate among the jets. However, jet tubes should not be any wider than the hibachi ribs to avoid interference with the e-beam.

- In the actual foil cooling, laser gas will be extracted, cooled and reused as the coolant for the foil. Bench top tests with gas similar to the laser gas would offer direct information on the cooling performance of near-wall jets.
- The IR imaging area only covered a limited portion of the foil due to the limited angle of view. It would be more informative if a much larger portion of the foil is imaged. This will also reduce the uncertainty resulting from the non-uniformity of jet velocities.
- The impingement location was adjusted by the rotation of the jet tube. Due to the small jet-to-foil spacing, the location is very sensitive to the rotation of the tube. A new mechanism to accurately control the jet impingement position will improve the accuracy of heat transfer measurement.
- More detailed CFD models that closely simulate the actual experimental setup will improve the simulation performance.

APPENDIX A

UNCERTAINTY ANALYSIS

This section summarizes the uncertainty analysis methods and results for various experimental quantities that are measured directly or indirectly. Uncertainties were derived using the well-known error propagation formula (Eq. A-1),

$$U_X^2 = \left(\frac{\partial f}{\partial A}U_A\right)^2 + \left(\frac{\partial f}{\partial B}U_B\right)^2 + \left(\frac{\partial f}{\partial C}U_C\right)^2 + \cdots \qquad \text{(Eq. A-1)}$$

where $X = f\left(A,B,C\right)$. U_X, U_A, U_B, and U_C are the uncertainty in X, A, B and C, respectively.

A.1 Jet Flow Rate Uncertainty

The flow rate of the jets is measured by a calibrated float-type gas rotameter. The measured flow rate was corrected for the operating pressure and was used to calculate the average jet velocity. For the calibration of the gas rotameter, a positive-displacement gas volume flow meter was used to record a fixed volume of air passing through the rotameter at a fixed float rotation. A stopwatch measured the elapsed time. The calibration curve for the gas rotameter (Brooks Instrument, Model: R-8M-25-4F, S/N: 8402H32654, Tube type: R-8M-25-4F, Float type: 8-RS-31) used in the experiments is shown in Figure A-1.

The uncertainty in jet flow rate measurement was determined by the error propagation formula,

$$\dot{V} = \frac{V_{measured}}{t_{elapsed}} \qquad \text{(Eq. A-2)}$$

$$\frac{U_{\dot{V}}}{\dot{V}} = \sqrt{\left(U_{V_{measured}} \Big/ V_{measured} \right)^2 + \left(U_{t_{elapsed}} \Big/ t_{elapsed} \right)^2} \qquad \text{(Eq. A-3)}$$

The uncertainty in volume measurement takes the minimum resolution (0.05 ft^3) of the gas volume meter for a typical recorded volume of 4.0 ft^3, which corresponds to a relative uncertainty of 1.25%. Though the stopwatch has a resolution of 0.01 *s*, the uncertainty in the time elapsed is set at 0.5s to account the response time the experimenter used to operate the stopwatch. The two uncertainties above combine to give a maximum relative uncertainty in volumetric flow rate of 2.6% over all the float positions.

A.2 Jet Velocity Distribution Uncertainty

The flow rate of each individual jet varies due to pressure drop inside jet tube and the random variation in the jet diameter. The uncertainty in jet exit velocity is determined first by experimentally measuring the jet velocity using a thermal anemometer. If assuming that the jet velocity distribution is a Gauss distribution, the uncertainty corresponding to twice the standard deviation results in a 95% confidence interval.

Figures A-2 and A-3 shows the distribution of nominal jet velocity and the normalized jet velocity of 26 jets, respectively, where the air is supplied from two ends of the jet tube. From the plots of jet velocity distribution, it is obvious that the velocity distribution is strongly influenced by the location of the jet relative to the header. Statistical analysis of the jet velocity distribution showed that the uncertainty in jet velocity is 18% for jet diameter of 0.8 mm and velocity at 33.2 m/s, 12% for jet diameter of 1.2 mm and jet velocity at 29.3 m/s, and 15% for jet diameter of 1.6 mm and jet velocity at 35.3 m/s.

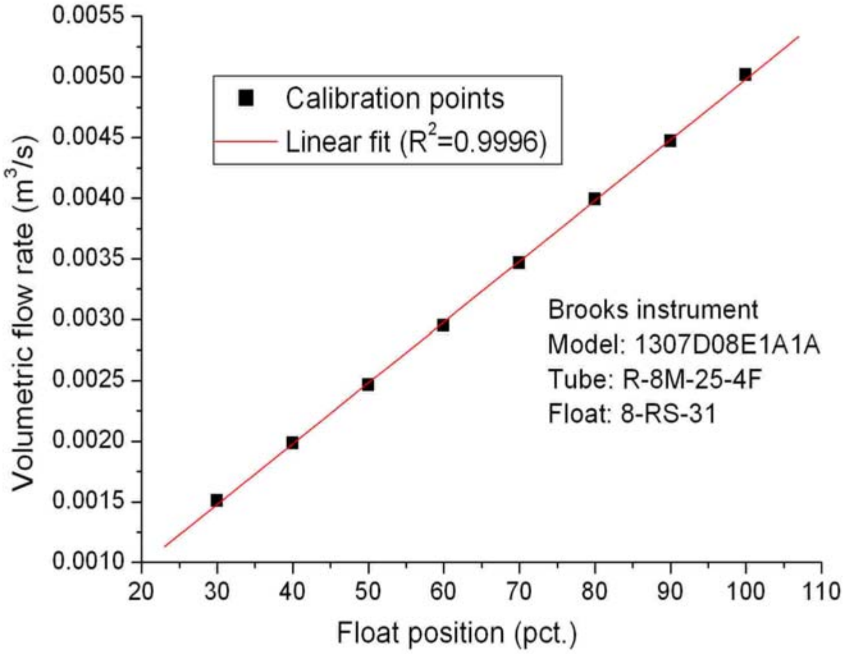

Figure A-1 Calibration curve for the gas rotameter (Model: R-8M-25-4F)

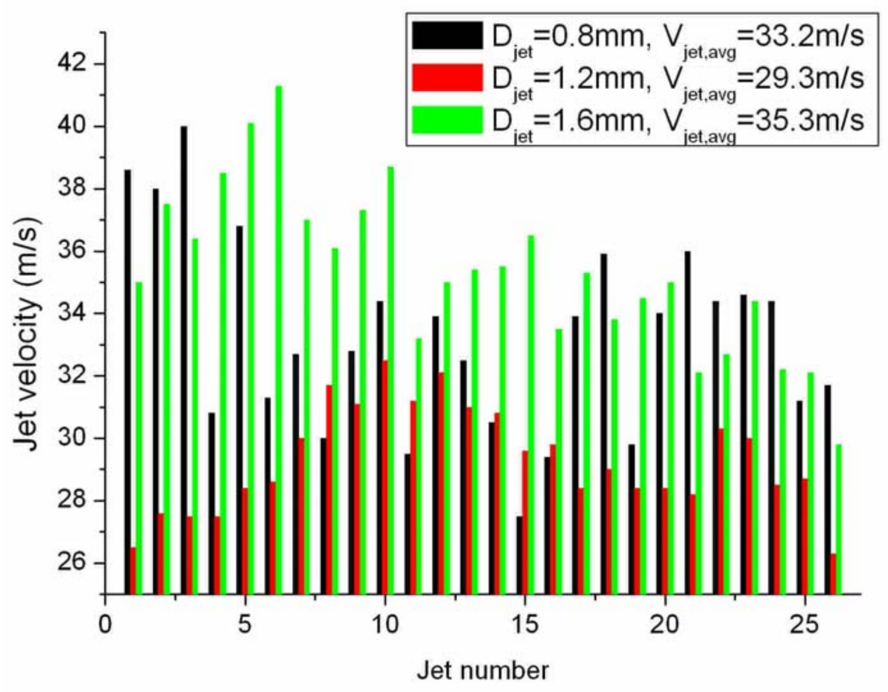

Figure A-2 Jet velocity distribution for 26 jets of one jet tube

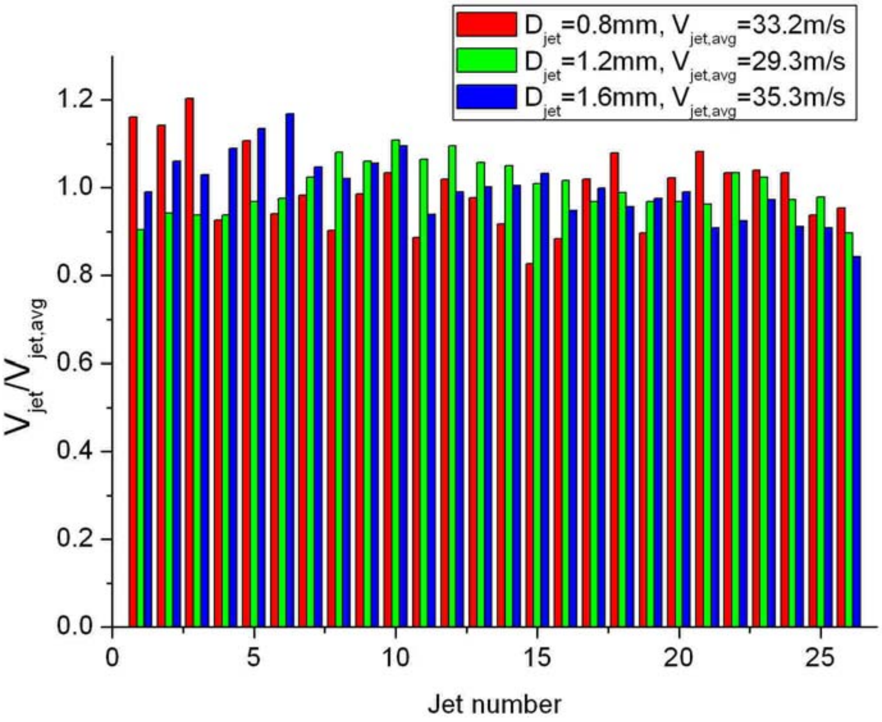

Figure A-3 Normalized jet velocity distribution for 26 jets for various jet diameters

A.3 Temperature Uncertainty

Two temperature techniques were used in the experiments to for both gas and foil temperature measurement: type-E thermocouples from OMEGA® and FLIR PM-280 Infrared thermography camera.

The uncertainty in the thermocouple reading was obtained from the manufacture provided uncertainty of 1.7 ^{o}C and the statistical fluctuations in the experimental measurement. For a typical case where the average foil temperature was at 110 ^{o}C, the standard deviation was 1.5 ^{o}C. These two terms combined to give an uncertainty in the thermocouple reading of 2.3 ^{o}C.

The IR camera used in the experiments has a resolution of 1.0 ^{o}C in temperature measurement. The camera computes the surface temperature based on a preset and constant emissivity for the entire target surface. Since the emissivity of the foil varies at different temperatures, the fixed emissivity value will give rise to the uncertainty in the temperature measurement. This uncertainty component in the temperature was accounted for by varying the emissivity values according to its range and determining the corresponding temperature change, which was used as the uncertainty resulting from the non-uniform emissivity of the foil. For a change of emissivity of 0.04 around the average value of 0.31, the resulting uncertainty in the temperature is under 5.0%.

A.4 Surface Heat Flux Uncertainty

The surface heat flux of the foil was determined by measuring the voltage drop (V), the current in the foil (I) and the area of the foil (A_f), where

$$q'' = \frac{V \times I}{A_f} \qquad \text{(Eq. A-4)}$$

The uncertainty in surface heat flux was determined using the error propagation formula,

$$\frac{U_{q''}}{q''} = \sqrt{\left(\frac{U_V}{V}\right)^2 + \left(\frac{U_I}{I}\right)^2 + \left(\frac{U_{A_f}}{A_f}\right)^2} \qquad \text{(Eq. A-5)}$$

The voltage was measured by an Agilent 34970A data acquisition system with a measurement accuracy of 0.01%; the current was measured using a shunt (Deltec MKB-300-100) with 0.25% measurement accuracy; the uncertainty in the foil area was determined by the resolution of the ruler (1mm) to be 2.95%. For a typical case where *V* has a average of 9.64V and uncertainty of 0.13% and *I* has a average of 25.11 A and uncertainty of 0.36% that corresponds to a 95% confidence interval, Eq. A-5 gives the uncertainty in surface heat flux of 2.99%.

A.5 Heat Transfer Coefficient Uncertainty

The uncertainty in heat transfer coefficient (*h*) was determined using the error propagation formula,

$$h = \frac{q''}{T_f - T_j} \qquad \text{(Eq. A-6)}$$

$$\frac{U_h}{h} = \sqrt{\left(\frac{U_{q''}}{q''}\right)^2 + \left(\frac{U_{T_j}}{T_f - T_j}\right)^2 + \left(\frac{U_{T_f}}{T_f - T_j}\right)^2} \qquad \text{(Eq. A-7)}$$

For the same case as in the above section, where T_f=361.1±15.6°C and T_j=22.2±1.7 °C, the uncertainty in heat transfer coefficient was calculated using Eq. A-7 at 5.51%.

A.6 Nusselt Number Uncertainty

The uncertainty in Nusselt number is similarly calculated using the error propagation formula, where

$$\frac{U_{Nu_D}}{Nu_D} = \sqrt{\left(\frac{U_h}{h}\right)^2 + \left(\frac{U_D}{D}\right)^2} \qquad \text{(Eq. A-8)}$$

The uncertainty in the diameter of a circular jet or the width of a slot jet was 0.05mm (based on the machining tolerances) and 0.025mm (measuring accuracy), respectively. For the same case as above, Eq. A-8 computes the uncertainty in Nusselt number to be 8.33% for the circular jet at 0.8 mm diameter and 6.05% for the slot jet of 1.0 mm width.

A.7 Jet Impingement Location Uncertainty

The alignment of jets towards the foil is adjusted by the rotation of the jet tube to a pre-calculated angle. Figure A-3 shows the jet impingement cooling scheme for the flat foil. The uncertainty in impingement location on the foil is mainly caused by the uncertainty in controlling the rotation angle of the jet tube, which is at least the angle that the opening on the jet tube subtends at the axis of the jet tube. So the uncertainty in jet impingement location for the flat foil is approximately as follows,

$$\frac{U_{loc}}{W_{foil}} = \frac{D_{jet}}{D_{tube}/2}\frac{L + D_{tube}/2}{W_{foil}} \qquad \text{(Eq. A-9)}$$

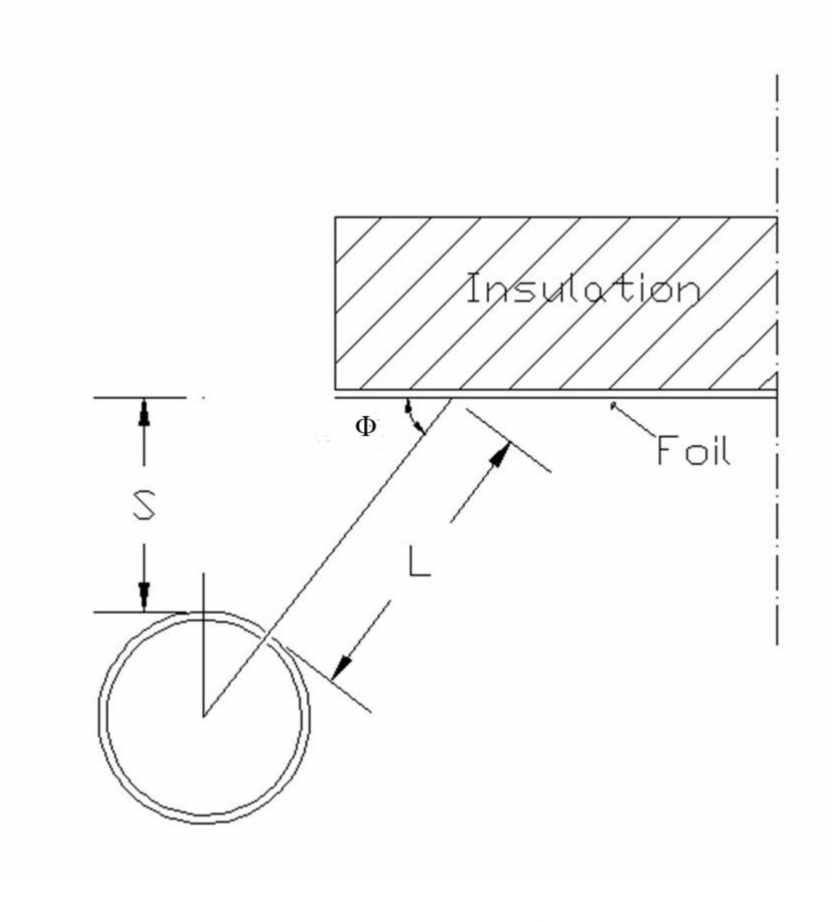

Figure A-4 Jet impinging scheme

The uncertainty for jet impingement location at various jet-to-foil spacing and jet diameters is summarized in Table A-1.

Table A-1 Uncertainty in impingement locations

d_{jet} (mm)	L (mm)	U_{loc} (mm)	U_{loc}/W (%)
0.8	8.7	2.2	6.61%
	10.4	2.5	7.46%
	12.2	2.8	8.31%
	13.9	3.1	9.16%
1.2	8.7	3.4	9.91%
	10.4	3.8	11.19%
	12.2	4.2	12.46%
	13.9	4.7	13.74%
1.6	8.7	4.5	13.22%
	10.4	5.1	14.92%
	12.2	5.7	16.62%
	13.9	6.2	18.32%

APPENDIX B

SUMMARY OF EXPERIMENTAL RESULTS OF FOIL COOLING USING PLANAR AND IMPINGING JETS

This appendix section summarizes the experimental results for all the tests of foil cooling using both planar and impinging jets. Detailed experimental parameters, including foil temperature, heat transfer coefficient, Nusselt number and other physical quantities, are tabulated.

B.1 Experimental Results of Flat Foil Cooling with a Planar Jet

Directly and indirectly measured experimental quantities included foil temperature, jet temperature and Reynolds number, bulk flow temperature and velocity, surface heat flux, heat transfer coefficient and Nusselt number. A total of six sets of experiments are summarized.

Table B-1 Experimental result for test case 1
($q''=2076.49 W/m^2$, $Re_s=0$, $V_{bulk}=4.0$ m/s, $T_{jet}=23.05^oC$, $T_{bulk}=22.10^oC$, S=1.0 mm)

T/C Location (m)	T_f (^oC)	h (W/m^2-K)	Nu_s
0.03	72.34	38.32	1.41
0.06	83.36	30.88	1.12
0.09	92.08	26.66	0.96
0.12	97.05	24.69	0.88
0.15	101.98	22.98	0.81
0.18	106.86	21.48	0.76
0.21	109.50	20.74	0.73
0.24	112.56	19.94	0.70
0.27	109.90	20.63	0.73

Table B-2 Experimental result for test case 2
($q''=2107.16 W/m^2$, $Re_s=1623$, $V_{bulk}=4.0$ m/s, $T_{jet}=22.68\ ^oC$, $T_{bulk}=21.83\ ^oC$, S=1.0 mm)

T/C Location (m)	T_f (^oC)	h (W/m^2-K)	Nu_s
0.03	45.00	87.91	3.36
0.06	59.12	53.50	2.00
0.09	69.66	41.04	1.52
0.12	80.34	33.00	1.20
0.15	86.00	29.82	1.08
0.18	90.99	27.45	0.99
0.21	92.41	26.84	0.96
0.24	95.78	25.48	0.91
0.27	95.03	25.77	0.92

Table B-3 Experimental result for test case 3
($q''=2150.85 W/m^2$, $Re_s=3276$, $V_{bulk}=4.0$ m/s, $T_{jet}=21.15\ ^oC$, $T_{bulk}=21.30\ ^oC$, S=1.0 mm)

T/C Location (m)	T_f (^oC)	h (W/m^2-K)	Nu_s
0.03	34.81	156.20	6.06
0.06	41.41	103.90	3.99
0.09	44.79	88.55	3.39
0.12	55.68	59.55	2.24
0.15	61.81	50.08	1.87
0.18	71.91	39.48	1.46
0.21	72.54	38.96	1.43
0.24	78.03	34.90	1.28
0.27	79.18	34.14	1.25

Table B-4 Experimental result for test case 4
(q”=4390.16 W/m^2, Re$_s$=0, V$_{bulk}$=4.0 m/s, T$_{jet}$=23.24 ^{o}C, T$_{bulk}$=22.07 ^{o}C, S=1.0 mm)

T/C Location (m)	T$_f$ (^{o}C)	h (W/m^2-K)	Nu$_s$
0.03	124.80	39.72	1.37
0.06	147.40	32.01	1.07
0.09	164.24	27.87	0.91
0.12	173.87	25.91	0.84
0.15	182.78	24.30	0.78
0.18	192.72	22.71	0.72
0.21	198.13	21.92	0.69
0.24	204.16	21.10	0.66
0.27	195.61	22.28	0.71

Table B-5 Experimental result for test case 5
(q”=4338.07 W/m^2, Re$_s$=1619, V$_{bulk}$=4.0 m/s, T$_{jet}$=23.07 ^{o}C, T$_{bulk}$=22.32 ^{o}C, S=1.0 mm)

T/C Location (m)	T$_f$ (^{o}C)	h (W/m^2-K)	Nu$_s$
0.03	45.34	91.23	3.38
0.06	58.04	57.72	2.07
0.09	67.98	44.49	1.55
0.12	78.07	35.9	1.22
0.15	85.19	31.49	1.05
0.18	91.24	28.46	0.94
0.21	92.98	27.68	0.91
0.24	96.89	26.07	0.85
0.27	95.60	26.59	0.87

Table B-6 Experimental results for test case 6
(q”=4335.21 W/m^2, Re$_s$=3279, V$_{bulk}$=4.0 m/s, T$_{jet}$=21.0 ^{o}C, T$_{bulk}$=22.17 ^{o}C, S=1.0 mm)

T/C Location (m)	T$_f$ (^{o}C)	h (W/m^2-K)	Nu$_s$
0.03	35.23	162.96	6.20
0.06	41.25	110.64	4.14
0.09	46.44	86.29	3.19
0.12	56.05	60.96	2.19
0.15	61.36	52.30	1.86
0.18	71.65	40.80	1.41
0.21	72.54	40.03	1.38
0.24	78.15	35.71	1.22
0.27	78.35	35.57	1.21

B.2 Experimental Results of Flat Foil Cooling with Impinging Jets

Experimental results include the original IR images, jet temperature, typical foil temperatures (min, max and mean) and corresponding heat transfer coefficient and Nusselt number computed for the analysis box.

Table B-7 Summary of experimental data for test case 1
(d_{jet}=0.8 mm, L=8.7 mm, Impact number=1/8, Impacting angle=47^o, T_{jet}=22.1 ^{o}C)

Re_d	q"(W/m^2)	T_{min}(^{o}C)	T_{max}(^{o}C)	T_{avg}(^{o}C)	h_{min}(W/m^2-K)	h_{max}(W/m^2-K)	h_{mean}(W/m^2-K)	$Nu_{d,min}$	$Nu_{d,max}$	$Nu_{d,mean}$
517	21633.7	151.2	330.3	240.8	65.4	155.2	92.2	2.1	4.9	2.9
1035	22634.9	120.0	256.5	188.3	92.5	221.4	130.5	2.9	7.0	4.1
1535	23195.2	97.0	190.0	143.5	134.6	302.0	186.2	4.2	9.8	5.8
2067	23604.5	79.5	180.5	130.0	145.7	401.9	213.9	4.6	12.6	6.7

Table B-8 Summary of experimental data for test case 2
(d_{jet}=0.8 mm, L=10.4 mm, Impact number=1/8, Impacting angle=47^o, T_{jet}=22.5 ^{o}C)

Re_d	q"(W/m^2)	T_{min}(^{o}C)	T_{max}(^{o}C)	T_{avg}(^{o}C)	h_{min}(W/m^2-K)	h_{max}(W/m^2-K)	h_{mean}(W/m^2-K)	$Nu_{d,min}$	$Nu_{d,max}$	$Nu_{d,mean}$
517	21855.5	191.8	344.3	268.1	62.3	118.4	81.65	2.0	3.7	2.6
1033	22891.7	120.0	265.2	192.6	90.2	224.3	128.7	2.8	7.0	4.0
1546	23262.1	106.3	197.6	152.0	130.2	272.7	176.1	4.1	8.5	5.5
2061	23663.8	88.7	182.5	135.6	144.7	350.3	204.8	4.5	11.0	6.4

Table B-9 Summary of experimental data for test case 3
(d_{jet}=0.8 mm, L=12.2 mm, Impact number=1/8, Impacting angle=47^o, T_{jet}=22.5 ^{o}C)

Re_d	q"(W/m^2)	T_{min}(^{o}C)	T_{max}(^{o}C)	T_{avg}(^{o}C)	h_{min}(W/m^2-K)	h_{max}(W/m^2-K)	h_{mean}(W/m^2-K)	$Nu_{d,min}$	$Nu_{d,max}$	$Nu_{d,mean}$
516	21757.0	203.2	351.1	277.2	60.4	109.8	77.9	1.9	3.4	2.4
1032	22622.5	128.3	265.6	197.0	88.8	204.0	123.8	2.8	6.4	3.9
1547	23023.3	116.8	220.2	168.5	111.8	234.3	151.4	3.5	7.4	4.8
2061	23324.1	97.9	205.8	151.9	123.8	301.8	175.6	3.9	9.5	5.5

Table B-10 Summary of experimental data for test case 4
(d_{jet}=0.8 mm, L=13.9 mm, Impact number=1/8, Impacting angle=47^o, T_{jet}=22.5 ^{o}C)

Re_d	q"(W/m^2)	T_{min}(^{o}C)	T_{max}(^{o}C)	T_{avg}(^{o}C)	h_{min}(W/m^2-K)	h_{max}(W/m^2-K)	h_{mean}(W/m^2-K)	$Nu_{d,min}$	$Nu_{d,max}$	$Nu_{d,mean}$
516	21757.0	220.2	364.7	292.5	57.7	99.8	73.1	1.8	3.1	2.6
1032	22622.5	165.5	290.2	227.9	79.7	149.1	103.8	2.5	4.7	3.3
1547	23023.3	120.0	250.2	185.1	97.5	227.7	136.5	3.1	7.1	4.3
2061	23324.1	118.0	246.6	182.3	99.8	234.4	140.0	3.1	7.4	4.4

Table B-11 Summary of experimental data for test case 5
(d_{jet}=0.8 mm, L=19.3 mm, Impact number=1/2, Impacting angle=24^o, T_{jet}=22.5 ^{o}C)

Re_d	q"(W/m^2)	T_{min}(^{o}C)	T_{max}(^{o}C)	T_{avg}(^{o}C)	h_{min}(W/m^2-K)	h_{max}(W/m^2-K)	h_{mean}(W/m^2-K)	$Nu_{d,min}$	$Nu_{d,max}$	$Nu_{d,mean}$
516	22243.7	260.1	361.1	310.6	58.5	83.4	68.8	1.8	2.6	2.2
1032	22824.2	220.1	351.1	285.6	63.2	105.1	79.0	2.0	3.3	2.5
1547	23262.5	125.9	309.9	217.9	76.7	213.2	112.8	2.4	6.7	3.5
2061	23389.9	112.4	296.1	204.3	81.0	246.9	122.0	2.5	7.7	3.8

Table B-12 Summary of experimental data for test case 6
(d_{jet}=0.8 mm, L=22.4 mm, Impact number=1/2, Impacting angle=24^o, T_{jet}=22.6 ^{o}C)

Re_d	q"(W/m^2)	T_{min}(^{o}C)	T_{max}(^{o}C)	T_{avg}(^{o}C)	h_{min}(W/m^2-K)	h_{max}(W/m^2-K)	h_{mean}(W/m^2-K)	$Nu_{d,min}$	$Nu_{d,max}$	$Nu_{d,mean}$
516	21248.4	215.5	351.5	283.5	58.6	99.7	73.7	1.8	3.1	2.3
1032	21884.7	224.4	347.3	285.9	61.1	98.3	75.4	1.9	3.1	2.4
1547	22489.4	127.9	328.7	228.3	69.1	201.0	102.9	2.2	6.3	3.2
2061	23202.3	107.5	287.7	197.6	83.7	261.8	126.8	2.6	8.2	4.0

Table B-13 Summary of experimental data for test case 7
(d_{jet}=0.8 mm, L=25.5 mm, Impact number=1/2, Impacting angle=24°, T_{jet}=22.4 °C)

Re_d	q"(W/m^2)	T_{min}(°C)	T_{max}(°C)	T_{avg}(°C)	h_{min}(W/m^2-K)	h_{max}(W/m^2-K)	h_{mean}(W/m^2-K)	$Nu_{d,min}$	$Nu_{d,max}$	$Nu_{d,mean}$
516	21670.2	265.8	376.0	320.9	55.0	79.9	65.2	1.7	2.5	2.1
1032	22191.9	217.9	358.9	288.4	61.1	105.1	77.2	1.9	3.3	2.4
1547	22768.3	192.1	332.4	262.3	67.9	124.0	87.7	2.1	3.9	2.8
2061	23287.8	125.9	320.0	223.0	74.0	213.0	109.8	2.3	6.7	3.5

Table B-14 Summary of experimental data for test case 8
(d_{jet}=0.8 mm, L=28.6 mm, Impact number=1/2, Impacting angle=24°, T_{jet}=22.4 °C)

Re_d	q"(W/m^2)	T_{min}(°C)	T_{max}(°C)	T_{avg}(°C)	h_{min}(W/m^2-K)	h_{max}(W/m^2-K)	h_{mean}(W/m^2-K)	$Nu_{d,min}$	$Nu_{d,max}$	$Nu_{d,mean}$
516	21410.2	261.7	367.5	314.6	54.9	79.1	64.8	1.7	2.5	2.0
1032	21784.7	246.0	350.4	298.2	59.6	87.5	70.9	1.9	2.7	2.2
1547	22354.2	200.0	341.2	270.6	64.4	115.6	82.7	2.0	3.6	2.6
2061	22894.9	166.5	301.3	233.9	77.2	149.4	101.7	2.4	4.5	3.2

Table B-15 Summary of experimental data for test case 9
(d_{jet}=1.2 mm, L=8.7 mm, Impact number=1/8, Impacting angle=47^o, T_{jet}=22.0 ^{o}C)

Re_d	q"(W/m^2)	T_{min}(^{o}C)	T_{max}(^{o}C)	T_{avg}(^{o}C)	h_{min}(W/m^2-K)	h_{max}(W/m^2-K)	h_{mean}(W/m^2-K)	$Nu_{d,min}$	$Nu_{d,max}$	$Nu_{d,mean}$
772	21231.1	140.9	318.6	241.1	71.7	179.5	97.2	3.4	8.4	4.6
1545	21874.7	90.7	199.2	145.0	128.1	328.1	184.2	6.0	15.4	9.7
2317	22914.2	71.9	120.7	96.3	240.2	471.4	318.2	11.3	22.3	15.0
3118	23494.0	58.3	107.5	82.9	272.5	634.8	381.3	12.9	30.0	18.0

Table B-16 Summary of experimental data for test case 10
(d_{jet}=1.2 mm, L=10.4 mm, Impact number=1/8, Impacting angle=47^o, T_{jet}=21.8 ^{o}C)

Re_d	q"(W/m^2)	T_{min}(^{o}C)	T_{max}(^{o}C)	T_{avg}(^{o}C)	h_{min}(W/m^2-K)	h_{max}(W/m^2-K)	h_{mean}(W/m^2-K)	$Nu_{d,min}$	$Nu_{d,max}$	$Nu_{d,mean}$
772	21878.0	151.6	335.6	243.6	65.2	158.4	92.4	3.1	7.4	4.3
1557	23010.3	100.9	203	152.0	123.2	281.6	171.4	5.8	13.3	8.1
2336	23410.4	79.9	151.2	115.6	177.1	393.1	244.2	8.4	18.7	11.5
3119	23807.7	62.8	123.3	93.1	230.3	565.6	327.3	10.9	26.7	15.5

Table B-17 Summary of experimental data for test case 11
(d_{jet}=1.2 mm, L=12.2 mm, Impact number=1/8, Impacting angle=47°, T_{jet}=22.1 °C)

Re_d	q"(W/m^2)	T_{min}(°C)	T_{max}(°C)	T_{avg}(°C)	h_{min}(W/m^2-K)	h_{max}(W/m^2-K)	h_{mean}(W/m^2-K)	$Nu_{d,min}$	$Nu_{d,max}$	$Nu_{d,mean}$
772	20146.4	161.6	334.8	248.2	64.7	145.6	89.6	3.0	6.8	4.2
1557	22178.6	110.9	215.2	163.1	114.7	249.0	157.1	5.4	11.7	7.4
2336	22695.7	87.3	199.9	143.6	127.4	346.3	186.3	6.0	16.3	8.8
3119	23167.8	71.4	179.5	125.5	146.8	466.1	223.3	6.9	22.0	10.5

Table B-18 Summary of experimental data for test case 12
(d_{jet}=1.2 mm, L=13.9 mm, Impact number=1/8, Impacting angle=47°, T_{jet}=22.2 °C)

Re_d	q"(W/m^2)	T_{min}(°C)	T_{max}(°C)	T_{avg}(°C)	h_{min}(W/m^2-K)	h_{max}(W/m^2-K)	h_{mean}(W/m^2-K)	$Nu_{d,min}$	$Nu_{d,max}$	$Nu_{d,mean}$
772	22862.3	174.1	374.0	274.1	62.4	145.2	87.3	2.9	6.8	4.9
1557	24229.6	120.0	302.8	211.4	86.2	246.7	127.8	4.1	11.6	6.0
2336	24974.4	115.0	272.7	193.9	99.6	268.3	145.3	4.7	12.6	6.8
3119	25715.2	92.0	241.0	166.5	117.3	366.6	177.8	5.5	17.3	8.4

Table B-19 Summary of experimental data for test case 13
(d_{jet}=1.2 mm, L=19.3 mm, Impact number=1/2, Impacting angle=24^o, T_{jet}=22.0 ^{o}C)

Re_d	q"(W/m^2)	T_{min}(^{o}C)	T_{max}(^{o}C)	T_{avg}(^{o}C)	h_{min}(W/m^2-K)	h_{max}(W/m^2-K)	h_{mean}(W/m^2-K)	$Nu_{d,min}$	$Nu_{d,max}$	$Nu_{d,mean}$
772	20215.6	249.6	347.7	298.7	62.3	89.4	73.4	2.9	4.2	3.4
1557	22131.9	121.4	313.4	217.4	75.9	222.1	113.1	3.6	10.5	5.3
2336	22620.7	120.0	303.5	211.8	80.3	229.9	119.0	3.8	10.8	5.6
3119	23188.7	109.2	266.9	188.1	94.5	264.1	139.2	4.5	12.5	6.6

Table B-20 Summary of experimental data for test case 14
(d_{jet}=1.2 mm, L=22.4 mm, Impact number=1/2, Impacting angle=24^o, T_{jet}=22.2 ^{o}C)

Re_d	q"(W/m^2)	T_{min}(^{o}C)	T_{max}(^{o}C)	T_{avg}(^{o}C)	h_{min}(W/m^2-K)	h_{max}(W/m^2-K)	h_{mean}(W/m^2-K)	$Nu_{d,min}$	$Nu_{d,max}$	$Nu_{d,mean}$
772	21928.9	260.9	392.9	326.9	59.4	92.4	72.3	2.8	4.3	3.4
1557	22101.8	158.0	350.8	254.4	67.1	176.7	103.5	3.2	8.3	4.9
2336	22183.7	104.4	328.3	216.4	72.4	268.9	114.1	3.4	12.7	5.4
3119	26069.6	115.7	261.6	188.7	108.7	277.5	156.2	5.1	13.1	7.4

Table B-21 Summary of experimental data for test case 15
(d_{jet}=1.2 mm, L=25.5 mm, Impact number=1/2, Impacting angle=24^o, T_{jet}=22.3 ^{o}C)

Re_d	q"(W/m^2)	T_{min}(^{o}C)	T_{max}(^{o}C)	T_{avg}(^{o}C)	h_{min}(W/m^2-K)	h_{max}(W/m^2-K)	h_{mean}(W/m^2-K)	$Nu_{d,min}$	$Nu_{d,max}$	$Nu_{d,mean}$
772	19483.4	267.8	373.6	320.7	55.6	79.7	56.5	2.6	3.7	3.1
1557	21548.4	146.2	337.2	241.7	68.3	173.0	97.9	3.2	8.2	4.6
2336	22366.0	120.0	294.3	207.2	82.1	227.6	120.6	3.9	10.7	5.7
3119	23204.7	107.0	204.4	155.7	127.1	272.2	173.2	6.0	12.8	8.2

Table B-22 Summary of experimental data for test case 16
(d_{jet}=1.2 mm, L=28.6 mm, Impact number=1/2, Impacting angle=24^o, T_{jet}=22.2 ^{o}C)

Re_d	q"(W/m^2)	T_{min}(^{o}C)	T_{max}(^{o}C)	T_{avg}(^{o}C)	h_{min}(W/m^2-K)	h_{max}(W/m^2-K)	h_{mean}(W/m^2-K)	$Nu_{d,min}$	$Nu_{d,max}$	$Nu_{d,mean}$
772	19060.4	269.7	369.6	319.7	55.0	77.3	64.3	2.6	3.6	3.0
1557	21251.7	149.6	334.8	242.2	67.9	166.3	96.4	3.2	7.8	4.5
2336	22230.0	125.0	287.8	206.4	83.7	215.8	122.2	3.9	10.5	5.8
3119	23175.5	109.0	200.0	154.5	130.1	266.2	174.8	6.1	12.5	8.2

Table B-23 Summary of experimental data for test case 17
(d_{jet}=1.6 mm, L=8.7 mm, Impact number=1/8, Impacting angle=47^o, T_{jet}=23.3 ^{o}C)

Re_d	q"(W/m^2)	T_{min}(^{o}C)	T_{max}(^{o}C)	T_{avg}(^{o}C)	h_{min}(W/m^2-K)	h_{max}(W/m^2-K)	h_{mean}(W/m^2-K)	$Nu_{d,min}$	$Nu_{d,max}$	$Nu_{d,mean}$
1027	22146.7	120.0	278.3	199.2	86.8	228.9	125.9	5.4	14.3	7.9
2075	23396.6	77.9	168.1	123.0	159.7	415.6	230.8	10.0	26.1	14.5
3116	24046.4	58.9	102.7	80.8	295.8	641.2	404.8	18.6	40.3	25.5
4159	24320.5	47.3	100.7	74.0	306.0	932.2	460.7	19.3	58.7	29.0

Table B-24 Summary of experimental data for test case 18
(d_{jet}=1.6 mm, L=10.4 mm, Impact number=1/8, Impacting angle=47^o, T_{jet}=22.9 ^{o}C)

Re_d	q"(W/m^2)	T_{min}(^{o}C)	T_{max}(^{o}C)	T_{avg}(^{o}C)	h_{min}(W/m^2-K)	h_{max}(W/m^2-K)	h_{mean}(W/m^2-K)	$Nu_{d,min}$	$Nu_{d,max}$	$Nu_{d,mean}$
1027	21569.5	125.0	255.1	190.1	92.9	211.2	129.0	5.8	13.2	8.1
2075	22747.7	80.7	197.6	139.2	128.9	382.2	192.8	8.1	24.1	12.1
3116	23715.3	62.3	137.0	99.7	205.1	579.6	303.0	12.9	36.5	19.1
4159	23779.3	51.0	102.6	76.8	294.2	813.5	432.1	18.5	51.1	27.2

Table B-25 Summary of experimental data for test case 19
(d_{jet}=1.6 mm, L=12.2 mm, Impact number=1/8, Impacting angle=47^o, T_{jet}=23.2 ^{o}C)

Re_d	q"(W/m^2)	T_{min}(^{o}C)	T_{max}(^{o}C)	T_{avg}(^{o}C)	h_{min}(W/m^2-K)	h_{max}(W/m^2-K)	h_{mean}(W/m^2-K)	$Nu_{d,min}$	$Nu_{d,max}$	$Nu_{d,mean}$
1027	21105.2	128.3	252.1	190.2	92.2	200.8	126.4	5.8	12.6	7.9
2075	22106.9	86.2	209.3	147.8	117.7	341.7	175.1	7.4	21.5	11.0
3116	22708.9	67.4	155.9	111.7	169.1	496.0	252.2	10.6	31.2	15.9
4159	23130.1	54.9	111.3	83.1	258.4	698.6	377.3	16.2	43.9	23.7

Table B-26 Summary of experimental data for test case 20
(d_{jet}=1.6 mm, L=13.9 mm, Impact number=1/8, Impacting angle=47^o, T_{jet}=23.5 ^{o}C)

Re_d	q"(W/m^2)	T_{min}(^{o}C)	T_{max}(^{o}C)	T_{avg}(^{o}C)	h_{min}(W/m^2-K)	h_{max}(W/m^2-K)	h_{mean}(W/m^2-K)	$Nu_{d,min}$	$Nu_{d,max}$	$Nu_{d,mean}$
1027	21094.9	132.8	275.8	204.3	83.6	193.0	116.4	5.2	12.1	7.3
2075	22463.6	92.5	213.3	152.9	117.4	318.5	171.6	7.4	20.0	10.8
3116	23015.9	73.8	174.0	123.9	151.5	445.0	226.0	9.5	27.9	14.2
4159	23473.6	63.3	144.5	103.9	191.4	566.4	286.1	12.0	35.6	18.0

Table B-27 Summary of experimental data for test case 21
(d_{jet}=1.6 mm, L=19.3 mm, Impact number=1/2, Impacting angle=24^o, T_{jet}=22.5 ^{o}C)

Re_d	q"(W/m^2)	T_{min}(^{o}C)	T_{max}(^{o}C)	T_{avg}(^{o}C)	h_{min}(W/m^2-K)	h_{max}(W/m^2-K)	h_{mean}(W/m^2-K)	$Nu_{d,min}$	$Nu_{d,max}$	$Nu_{d,mean}$
1027	20281.7	147.9	270.3	209.1	82.7	163.8	119.6	5.2	10.3	7.5
2075	21614.2	108.7	201.4	155.1	121.7	254.6	164.7	7.6	15.9	10.3
3116	22315.6	84.1	176.3	130.2	144.3	357.1	205.5	9.1	22.4	12.9
4159	22877.1	70.9	152.8	111.9	174.1	462.2	252.9	11.0	29.1	15.9

Table B-28 Summary of experimental data for test case 22
(d_{jet}=1.6 mm, L=22.4 mm, Impact number=1/2, Impacting angle=24^o, T_{jet}=22.2 ^{o}C)

Re_d	q"(W/m^2)	T_{min}(^{o}C)	T_{max}(^{o}C)	T_{avg}(^{o}C)	h_{min}(W/m^2-K)	h_{max}(W/m^2-K)	h_{mean}(W/m^2-K)	$Nu_{d,min}$	$Nu_{d,max}$	$Nu_{d,mean}$
1027	20212.9	199.9	313.9	256.9	69.6	114.6	86.6	4.4	7.2	5.4
2075	21764.0	120.0	252.1	186.1	94.6	222.1	132.7	5.9	13.9	8.3
3116	22631.7	100.7	196.8	148.8	129.3	286.6	178.2	8.1	18.0	11.2
4159	23283.0	83.7	144.5	114.1	189.4	374.7	251.6	11.9	23.6	15.8

Table B-29 Summary of experimental data for test case 23
(d_{jet}=1.6 mm, L=25.5 mm, Impact number=1/2, Impacting angle=24^o, T_{jet}=22.6 ^{o}C)

Re_d	q"(W/m^2)	T_{min}(^{o}C)	T_{max}(^{o}C)	T_{avg}(^{o}C)	h_{min}(W/m^2-K)	h_{max}(W/m^2-K)	h_{mean}(W/m^2-K)	$Nu_{d,min}$	$Nu_{d,max}$	$Nu_{d,mean}$
1027	20351.4	217.8	329.1	273.5	66.6	104.7	81.4	4.2	6.6	5.1
2075	22093.7	130.0	261.2	195.6	92.4	204.6	127.3	5.8	12.8	8.0
3116	22878.0	98.9	201.4	150.2	127.6	297.9	178.7	8.0	18.7	11.2
4159	23283.2	85.9	170.5	128.2	157.6	369.0	220.9	9.9	23.1	13.8

Table B-30 Summary of experimental data for test case 24
(d_{jet}=1.6 mm, L=28.6 mm, Impact number=1/2, Impacting angle=24^o, T_{jet}=22.0 ^{o}C)

Re_d	q"(W/m^2)	T_{min}(^{o}C)	T_{max}(^{o}C)	T_{avg}(^{o}C)	h_{min}(W/m^2-K)	h_{max}(W/m^2-K)	h_{mean}(W/m^2-K)	$Nu_{d,min}$	$Nu_{d,max}$	$Nu_{d,mean}$
1027	19895.4	236.6	343.1	289.9	62.0	92.8	74.4	3.9	5.8	4.7
2075	21774.2	140.0	292.6	216.3	80.4	184.1	111.9	5.1	11.6	7.0
3116	22725.6	107.9	225.0	166.5	111.9	264.3	157.2	7.0	16.6	9.9
4159	23242.5	91.0	177.3	134.2	149.6	336.4	207.1	9.4	21.1	13.0

B.3 Experimental Results of Scalloped Foil Cooling with Impinging Jets

Experimental results include the original IR images, jet temperature, typical foil temperatures (min, max and mean) and corresponding heat transfer coefficient and Nusselt number computed for the analysis box.

Table B-31 Summary of experimental data for test case 25
(d_{jet}=0.8 mm, L=8.1 mm, Impact number=1/8, Impacting angle=33.5^o, T_{jet}=22.8 ^{o}C)

Re_d	q"(W/m^2)	T_{min}(^{o}C)	T_{max}(^{o}C)	T_{avg}(^{o}C)	h_{min}(W/m^2-K)	h_{max}(W/m^2-K)	h_{mean}(W/m^2-K)	$Nu_{d,min}$	$Nu_{d,max}$	$Nu_{d,mean}$
514.9	22121.6	206.9	392.3	315.1	59.9	120.2	75.7	1.9	3.8	2.4
1031	24260.5	107.5	319.3	233.3	81.8	286.6	115.3	2.6	9.0	3.6
1548	25930.7	98.9	243.6	171.3	117.2	339.1	174.2	3.7	10.6	5.5
2063	27125.2	92.0	215.2	153.6	140.8	390.7	207.0	4.4	12.2	6.5

Table B-32 Summary of experimental data for test case 26
(d_{jet}=0.8 mm, L=10.1 mm, Impact number=1/8, Impacting angle=35.3^o, T_{jet}=22.7 ^{o}C)

Re_d	q"(W/m^2)	T_{min}(^{o}C)	T_{max}(^{o}C)	T_{avg}(^{o}C)	h_{min}(W/m^2-K)	h_{max}(W/m^2-K)	h_{mean}(W/m^2-K)	$Nu_{d,min}$	$Nu_{d,max}$	$Nu_{d,mean}$
514.5	22121.6	222.3	395.8	332.7	59.8	111.9	72.0	1.9	3.5	2.3
1030	24340.1	121.4	326.2	248.6	80.2	246.7	107.8	2.5	7.7	3.4
1545	25731.3	102.7	244.1	173.4	116.2	321.8	170.8	3.6	10.1	5.4
2062	26484.0	97.0	220.2	158.6	134.0	356.1	194.8	4.2	11.2	6.1

Table B-33 Summary of experimental data for test case 27
(d_{jet}=0.8 mm, L=12.0 mm, Impact number=1/8, Impacting angle=37.0°, T_{jet}=22.7 °C)

Re_d	q"(W/m^2)	T_{min}(°C)	T_{max}(°C)	T_{avg}(°C)	h_{min}(W/m^2-K)	h_{max}(W/m^2-K)	h_{mean}(W/m^2-K)	$Nu_{d,min}$	$Nu_{d,max}$	$Nu_{d,mean}$
514.5	23944.0	278.2	414.1	353.1	61.2	93.8	72.5	1.9	2.9	2.3
1030	26181.0	163.8	339.2	273.3	82.7	185.8	104.5	2.6	5.8	3.2
1545	27989.0	120.0	278.7	199.4	109.4	287.9	158.5	3.4	9.0	5.0
2060	28350.0	107.5	270.3	188.9	114.6	334.8	170.7	3.6	10.5	5.4

Table B-34 Summary of experimental data for test case 28
(d_{jet}=0.8 mm, L=13.9 mm, Impact number=1/8, Impacting angle=38.7°, T_{jet}=22.7 °C)

Re_d	q"(W/m^2)	T_{min}(°C)	T_{max}(°C)	T_{avg}(°C)	h_{min}(W/m^2-K)	h_{max}(W/m^2-K)	h_{mean}(W/m^2-K)	$Nu_{d,min}$	$Nu_{d,max}$	$Nu_{d,mean}$
514.9	23331.0	273.4	408.2	362.2	60.6	93.1	68.8	1.9	2.9	2.2
1030	25535.0	188.6	351.9	290.1	77.6	154.0	95.5	2.4	4.8	3.0
1546	27414.0	112.4	285.3	218.4	104.4	305.7	140.0	3.6	9.6	4.4
2061	28660.0	109.2	261.2	185.2	120.2	331.5	176.4	3.8	10.4	5.5

Table B-35 Summary of experimental data for test case 29
(d_{jet}=0.8 mm, L=22.1 mm, Impact number=1/2, Impacting angle=35.4^o, T_{jet}=22.7 ^{o}C)

Re_d	q"(W/m^2)	T_{min}(^{o}C)	T_{max}(^{o}C)	T_{avg}(^{o}C)	h_{min}(W/m^2-K)	h_{max}(W/m^2-K)	h_{mean}(W/m^2-K)	$Nu_{d,min}$	$Nu_{d,max}$	$Nu_{d,mean}$
516	22871.0	331.6	412.9	371.1	58.6	74.0	65.6	1.8	2.3	2.1
1031	24778.0	252.3	366.4	318.6	72.1	107.9	83.7	2.3	3.4	2.6
1545	26167.0	204.3	282.5	282.5	83.6	144.1	100.7	2.6	4.5	3.2
2060	28029.0	149.6	304.0	238.6	99.7	221.1	129.9	3.1	6.9	4.1

Table B-36 Summary of experimental data for test case 30
(d_{jet}=0.8 mm, L=24.2 mm, Impact number=1/2, Impacting angle=38.4^o, T_{jet}=22.7 ^{o}C)

Re_d	q"(W/m^2)	T_{min}(^{o}C)	T_{max}(^{o}C)	T_{avg}(^{o}C)	h_{min}(W/m^2-K)	h_{max}(W/m^2-K)	h_{mean}(W/m^2-K)	$Nu_{d,min}$	$Nu_{d,max}$	$Nu_{d,mean}$
516	22575.0	336.8	406.1	375.4	58.9	71.8	64.0	1.9	2.3	2.0
1031	24479.0	264.2	358.9	311.5	72.8	101.3	84.7	2.3	3.2	2.7
1545	25739.0	200.0	337.6	275.9	81.8	145.3	101.7	2.6	4.6	3.2
2058	27388.0	128.3	286.5	220.7	103.9	260.1	138.5	3.3	8.1	4.3

Table B-37 Summary of experimental data for test case 31
(d_{jet}=0.8 mm, L=26.2 mm, Impact number=1/2, Impacting angle=41.2°, T_{jet}=22.9 °C)

Re_d	q"(W/m^2)	T_{min}(°C)	T_{max}(°C)	T_{avg}(°C)	h_{min}(W/m^2-K)	h_{max}(W/m^2-K)	h_{mean}(W/m^2-K)	$Nu_{d,min}$	$Nu_{d,max}$	$Nu_{d,mean}$
515.6	23157.0	333.6	405.0	378.4	60.6	74.5	65.1	1.9	2.3	2.0
1030	25107.0	276.9	353.8	315.3	75.6	98.4	85.5	2.4	3.1	2.7
1543	26343.0	200.0	318.8	271.9	89.1	148.9	105.9	2.8	4.7	3.3
2054	29069.0	123.3	273.5	214.8	112.2	280.7	146.6	2.5	8.8	4.6

Table B-38 Summary of experimental data for test case 32
(d_{jet}=0.8 mm, L=28.1 mm, Impact number=1/2, Impacting angle=43.9°, T_{jet}=22.8 °C)

Re_d	q"(W/m^2)	T_{min}(°C)	T_{max}(°C)	T_{avg}(°C)	h_{min}(W/m^2-K)	h_{max}(W/m^2-K)	h_{mean}(W/m^2-K)	$Nu_{d,min}$	$Nu_{d,max}$	$Nu_{d,mean}$
515.4	22616.0	287.1	394.4	366.3	60.8	85.5	65.8	1.9	2.7	2.1
1030	24365.0	273.4	354.5	309.5	73.5	97.2	85.0	2.3	3.1	2.7
1545	25805.0	215.2	309.7	267.1	90.0	134.1	105.6	2.8	4.2	3.3
2059	27600.0	152.8	271.1	223.3	111.2	212.5	137.7	3.5	6.7	4.3

Table B-39 Summary of experimental data for test case 33
(d_{jet}=1.2 mm, L=8.1 mm, Impact number=1/8, Impacting angle=33.5°, T_{jet}=22.0 °C)

Re_d	q"(W/m^2)	T_{min}(°C)	T_{max}(°C)	T_{avg}(°C)	h_{min}(W/m^2-K)	h_{max}(W/m^2-K)	h_{mean}(W/m^2-K)	$Nu_{d,min}$	$Nu_{d,max}$	$Nu_{d,mean}$
769.4	22790.0	158.0	376.0	299.7	64.7	169.4	82.5	3.0	7.9	3.9
1554	25055.0	113.5	261.6	187.4	104.5	273.2	151.3	4.9	12.9	7.1
2334	26010.0	89.5	194.3	141.9	150.6	383.0	216.2	7.1	18.1	10.2
3118	26993.0	71.9	261.2	103.4	237.5	533.0	328.6	11.2	25.2	15.5

Table B-40 Summary of experimental data for test case 34
(d_{jet}=1.2 mm, L=10.1 mm, Impact number=1/8, Impacting angle=35.3°, T_{jet}=22.3 °C)

Re_d	q"(W/m^2)	T_{min}(°C)	T_{max}(°C)	T_{avg}(°C)	h_{min}(W/m^2-K)	h_{max}(W/m^2-K)	h_{mean}(W/m^2-K)	$Nu_{d,min}$	$Nu_{d,max}$	$Nu_{d,mean}$
769	22559.0	176.4	372.3	303.4	64.7	147.6	80.6	3.0	6.9	3.8
1559	24751.0	116.8	266.1	191.5	101.1	259.2	145.4	4.8	12.2	6.9
2332	25893.0	88.9	181.5	135.2	162.1	385.7	228.2	7.6	18.2	10.8
3100	26982.0	72.4	114.8	93.6	291.6	538.2	378.3	13.7	25.3	17.8

Table B-41 Summary of experimental data for test case 35
(d_{jet}=1.2 mm, L=12.0 mm, Impact number=1/8, Impacting angle=37.0^o, T_{jet}=21.7 ^{o}C)

Re_d	q"(W/m^2)	T_{min}(^{o}C)	T_{max}(^{o}C)	T_{avg}(^{o}C)	h_{min}(W/m^2-K)	h_{max}(W/m^2-K)	h_{mean}(W/m^2-K)	$Nu_{d,min}$	$Nu_{d,max}$	$Nu_{d,mean}$
770	23812.0	206.9	395.5	325.8	64.0	129.8	78.8	3.0	3.7	6.1
1563	26862.0	120.0	276.9	198.5	104.9	270.9	151.2	5.0	7.1	12.8
2342	28198.0	100.7	198.4	149.6	159.0	354.1	219.4	7.5	10.4	16.7
3115	29505.0	83.7	137.0	110.4	255.4	474.1	331.8	12.0	15.7	22.4

Table B-42 Summary of experimental data for test case 36
(d_{jet}=1.2 mm, L=13.9 mm, Impact number=1/8, Impacting angle=38.7^o, T_{jet}=22.0 ^{o}C)

Re_d	q"(W/m^2)	T_{min}(^{o}C)	T_{max}(^{o}C)	T_{avg}(^{o}C)	h_{min}(W/m^2-K)	h_{max}(W/m^2-K)	h_{mean}(W/m^2-K)	$Nu_{d,min}$	$Nu_{d,max}$	$Nu_{d,mean}$
769	22732.0	217.9	390.8	327.1	61.9	117.0	74.9	2.9	5.5	3.5
1560	25634.0	125.0	260.3	191.7	107.2	246.9	149.4	5.1	11.7	7.1
2335	26666.0	101.7	181.5	141.6	166.7	332.7	222.1	7.9	15.7	10.5
3109	27602.0	82.8	120.7	101.8	279.1	452.4	345.2	13.2	21.3	16.3

Table B-43 Summary of experimental data for test case 37
(d_{jet}=1.2 mm, L=22.1 mm, Impact number=1/2, Impacting angle=35.4^o, T_{jet}=21.6 ^{o}C)

Re_d	q"(W/m^2)	T_{min}(^{o}C)	T_{max}(^{o}C)	T_{avg}(^{o}C)	h_{min}(W/m^2-K)	h_{max}(W/m^2-K)	h_{mean}(W/m^2-K)	$Nu_{d,min}$	$Nu_{d,max}$	$Nu_{d,mean}$
770.7	23776.0	272.6	362.5	325.3	70.1	95.3	78.7	3.3	3.7	4.5
1563	26056.0	162.9	275.0	227.9	102.5	183.4	125.8	4.8	6.0	8.7
2344	26541.0	102.7	230.1	180.6	126.9	324.5	166.2	6.0	7.9	15.3
3114	27993.0	90.0	206.5	148.3	151.3	408.7	220.8	7.1	10.4	19.3

Table B-44 Summary of experimental data for test case 38
(d_{jet}=1.2 mm, L=24.2 mm, Impact number=1/2, Impacting angle=38.4^o, T_{jet}=22.2 ^{o}C)

Re_d	q"(W/m^2)	T_{min}(^{o}C)	T_{max}(^{o}C)	T_{avg}(^{o}C)	h_{min}(W/m^2-K)	h_{max}(W/m^2-K)	h_{mean}(W/m^2-K)	$Nu_{d,min}$	$Nu_{d,max}$	$Nu_{d,mean}$
768.6	23511.0	291.2	358.2	328.4	70.3	87.9	77.2	3.3	4.1	3.6
1555	25636.0	201.5	287.1	247.5	96.6	142.6	113.6	4.6	6.7	5.4
2331	27032.0	130.6	233.5	192.6	127.7	248.5	158.3	6.0	11.7	7.5
3114	28244.0	120.0	209.3	164.7	150.4	286.7	197.2	7.1	13.5	9.3

Table B-45 Summary of experimental data for test case 39
(d_{jet}=1.2 mm, L=26.2 mm, Impact number=1/2, Impacting angle=41.2^o, T_{jet}=21.7 ^{o}C)

Re_d	q"(W/m^2)	T_{min}(^{o}C)	T_{max}(^{o}C)	T_{avg}(^{o}C)	h_{min}(W/m^2-K)	h_{max}(W/m^2-K)	h_{mean}(W/m^2-K)	$Nu_{d,min}$	$Nu_{d,max}$	$Nu_{d,mean}$
770.6	23284.0	304.3	373.0	337.1	66.6	82.8	74.2	3.1	3.9	3.5
1564	25649.0	216.7	293.9	253.1	93.9	130.9	110.4	4.4	6.2	5.2
2340	27120.0	139.0	248.1	201.4	119.5	230.1	150.5	6.5	10.9	7.1
3109	28317.0	125.0	214.6	169.8	146.8	274.3	191.3	6.9	12.9	9.0

Table B-46 Summary of experimental data for test case 40
(d_{jet}=1.2 mm, L=28.0 mm, Impact number=1/2, Impacting angle=43.9^o, T_{jet}=22.0 ^{o}C)

Re_d	q"(W/m^2)	T_{min}(^{o}C)	T_{max}(^{o}C)	T_{avg}(^{o}C)	h_{min}(W/m^2-K)	h_{max}(W/m^2-K)	h_{mean}(W/m^2-K)	$Nu_{d,min}$	$Nu_{d,max}$	$Nu_{d,mean}$
770.2	21840.0	282.8	356.0	323.8	65.6	84.2	72.7	3.1	4.0	3.4
1558	23916.0	198.4	282.2	236.4	91.7	135.1	111.2	4.3	6.4	5.3
2335	24999.0	111.3	250.2	180.0	109.3	278.5	157.8	5.2	13.1	7.4
3109	26033.0	95.0	199.2	147.1	146.7	355.6	207.7	6.9	16.8	9.8

Table B-47 Summary of experimental data for test case 41
(d_{jet}=1.6 mm, L=8.1 mm, Impact number=1/8, Impacting angle=33.5^o, T_{jet}=21.8 ^{o}C)

Re_d	q"(W/m^2)	T_{min}(^{o}C)	T_{max}(^{o}C)	T_{avg}(^{o}C)	h_{min}(W/m^2-K)	h_{max}(W/m^2-K)	h_{mean}(W/m^2-K)	$Nu_{d,min}$	$Nu_{d,max}$	$Nu_{d,mean}$
1024	23932.0	104.4	319.7	238.1	80.9	297.0	111.7	5.1	18.6	7.0
2077	25623.0	86.5	188.2	137.4	153.7	393.9	221.1	9.7	24.8	13.9
3121	26440.0	66.4	114.8	90.6	282.2	583.3	380.5	17.8	36.8	24.0
4166	26894.0	56.3	110.0	83.2	302.0	760.6	432.0	19.0	47.9	27.2

Table B-48 Summary of experimental data for test case 42
(d_{jet}=1.6 mm, L=10.1 mm, Impact number=1/8, Impacting angle=35.3^o, T_{jet}=22.1 ^{o}C)

Re_d	q"(W/m^2)	T_{min}(^{o}C)	T_{max}(^{o}C)	T_{avg}(^{o}C)	h_{min}(W/m^2-K)	h_{max}(W/m^2-K)	h_{mean}(W/m^2-K)	$Nu_{d,min}$	$Nu_{d,max}$	$Nu_{d,mean}$
1026	23687.0	112.4	308.7	234.6	83.0	266.1	112.2	5.2	16.6	7.0
2071	25465.0	90.0	181.5	135.8	159.5	373.9	223.5	10.0	23.5	14.0
3110	26258.0	69.4	132.8	101.1	236.3	550.5	330.7	14.9	34.6	20.8
4154	27000.0	47.6	120.0	88.9	273.9	746.5	400.8	17.2	46.9	25.2

Table B-49 Summary of experimental data for test case 43
(d_{jet}=1.6 mm, L=12.0 mm, Impact number=1/8, Impacting angle=37.0^o, T_{jet}=22.0 ^{o}C)

Re_d	q"(W/m^2)	T_{min}(^{o}C)	T_{max}(^{o}C)	T_{avg}(^{o}C)	h_{min}(W/m^2-K)	h_{max}(W/m^2-K)	h_{mean}(W/m^2-K)	$Nu_{d,min}$	$Nu_{d,max}$	$Nu_{d,mean}$
1027	25391.0	138.2	334.4	262.5	81.6	221.1	106.2	5.1	13.8	6.6
2078	27568.0	99.9	205.1	152.5	150.0	350.8	210.2	9.4	22.1	13.2
3113	28531.0	81.0	164.2	122.6	200.0	480.1	282.4	12.6	30.2	17.8
4145	29565.0	68.4	130.6	199.5	271.7	634.4	380.5	17.2	39.9	23.9

Table B-50 Summary of experimental data for test case 44
(d_{jet}=1.6 mm, L=13.9 mm, Impact number=1/8, Impacting angle=38.7^o, T_{jet}=21.6 ^{o}C)

Re_d	q"(W/m^2)	T_{min}(^{o}C)	T_{max}(^{o}C)	T_{avg}(^{o}C)	h_{min}(W/m^2-K)	h_{max}(W/m^2-K)	h_{mean}(W/m^2-K)	$Nu_{d,min}$	$Nu_{d,max}$	$Nu_{d,mean}$
1026	25638.0	180.8	362.2	295.4	75.7	162.9	94.3	4.7	10.2	5.9
2083	28234.0	110.5	212.7	161.6	147.8	316.4	201.4	9.3	19.9	12.7
3121	29195.0	86.5	169.3	127.9	197.1	446.7	273.5	12.4	28.1	17.2
4163	29677.0	70.9	139.0	105.0	251.6	595.3	353.5	15.8	37.5	22.3

Table B-51 Summary of experimental data for test case 45
(d_{jet}=1.6 mm, L=22.1 mm, Impact number=1/2, Impacting angle=35.4^{o}, T_{jet}=21.8 ^{o}C)

Re_d	q"(W/m^2)	T_{min}(^{o}C)	T_{max}(^{o}C)	T_{avg}(^{o}C)	h_{min}(W/m^2-K)	h_{max}(W/m^2-K)	h_{mean}(W/m^2-K)	$Nu_{d,min}$	$Nu_{d,max}$	$Nu_{d,mean}$
1028	22514.0	201.5	304.3	262.9	80.1	126.3	93.9	5.9	7.9	5.0
2074	24231.0	150.0	205.8	177.9	131.6	188.8	155.1	8.3	11.9	9.8
3116	25001.0	119.2	165.5	142.4	173.5	255.6	206.6	10.9	16.1	13.0
4166	25693.0	100.7	130.6	115.7	234.5	322.6	271.5	14.8	20.3	17.1

Table B-52 Summary of experimental data for test case 46
(d_{jet}=1.6 mm, L=24.2 mm, Impact number=1/2, Impacting angle=38.4^{o}, T_{jet}=21.9 ^{o}C)

Re_d	q"(W/m^2)	T_{min}(^{o}C)	T_{max}(^{o}C)	T_{avg}(^{o}C)	h_{min}(W/m^2-K)	h_{max}(W/m^2-K)	h_{mean}(W/m^2-K)	$Nu_{d,min}$	$Nu_{d,max}$	$Nu_{d,mean}$
1028	24576.0	231.7	320.1	284.3	82.8	117.8	94.1	5.2	7.4	5.9
2080	26395.0	142.7	283.3	200.0	121.6	217.3	147.6	7.7	13.7	9.3
3116	27609.0	125.0	195.2	160.1	158.9	266.5	199.1	10.0	16.8	12.5
4146	28504.0	116.5	158.8	137.7	208.1	301.0	245.9	13.1	18.9	15.5

Table B-53 Summary of experimental data for test case 47
(d_{jet}=1.6 mm, L=26.2 mm, Impact number=1/2, Impacting angle=41.2°, T_{jet}=21.5 °C)

Re_d	q"(W/m^2)	T_{min}(°C)	T_{max}(°C)	T_{avg}(°C)	h_{min}(W/m^2-K)	h_{max}(W/m^2-K)	h_{mean}(W/m^2-K)	$Nu_{d,min}$	$Nu_{d,max}$	$Nu_{d,mean}$
1031	24162.0	235.6	317.9	281.0	81.8	113.4	93.5	5.1	7.1	5.9
2081	27407.0	149.6	255.0	205.0	111.2	202.5	141.6	7.0	12.8	8.9
3122	27044.0	135.0	227.3	181.2	151.1	237.4	168.9	8.3	14.9	10.6
4163	27931.0	116.0	190.9	153.5	164.5	294.2	210.9	10.4	18.5	13.3

Table B-54 Summary of experimental data for test case 48
(d_{jet}=1.6 mm, L=28.1 mm, Impact number=1/2, Impacting angle=43.9°, T_{jet}=21.5 °C)

Re_d	q"(W/m^2)	T_{min}(°C)	T_{max}(°C)	T_{avg}(°C)	h_{min}(W/m^2-K)	h_{max}(W/m^2-K)	h_{mean}(W/m^2-K)	$Nu_{d,min}$	$Nu_{d,max}$	$Nu_{d,mean}$
1030	24148.0	258.4	331.2	292.2	78.3	102.5	89.6	4.9	6.4	5.6
2081	27811.0	157.3	251.6	210.2	114.5	193.8	139.6	7.2	12.2	8.8
3124	28327.0	140.0	214.6	177.3	140.7	228.9	174.3	8.9	14.4	11.0
4162	29133.0	112.3	168.1	140.2	193.2	311.4	238.4	12.2	19.6	15.0

REFERENCES

Al-Sanea, S., “A Numerical Study of the Flow and Heat-Transfer Characteristics of an Impinging Laminar Slot-Jet Including Crossflow Effects”, *Int. J. Heat and Mass Transfer*, Vol. 35, pp. 2501-2513, 1992.

Ballal, D. and Lefebvre, A., “Film Cooling Effectiveness in the Near Slot Region”, *J. Heat Transfer*, *Serials C*, Vol. 95, pp. 265, 1973.

Bayramian, A., Beach, R., Bibeau, C., Campbell, R., Davis, W., Dawson, J., Dimercurio L., Ebbers, C., Freitas, B., Hood, K., Kanz, V., Menapace, J., Payne, S., Schaffers, K., Skulina, K., Telford, S., Tassano, J., DeWald, A., Rankin, J., Hill, M. and Randles, M., “Operation of the Mercury Laser; Testbed for DPSSL IFE Driver Technology”, *Proceedings of 3rd Inertial Fusion Sciences and Applications*, pp. 563-567, Sep.7-12, Monterey, CA, USA, 2003.

Behbahani, A. and Goldstein, R., “Local Heat Transfer to Staggered Arrays of Impinging Circular Air Jets”, *J. Engineering for Power,* Vol. 105, pp. 354-360, 1983

Bouchez, J. and Goldstein, R., “Impingement Cooling from a Circular Jet in a Cross Flow”, *Int. J. Heat Mass Transfer,* Vol. 18, pp. 719-730, 1975.

Burns, W. and Stollery J., “The Influence of Foreign Gas Injection on Slot Geometry on Film Cooling Effectiveness”, *Int. J. Heat Mass Transfer,* Vol. 12, pp. 935-951, 1969.

Burns, P., Myers, M., Sethian, J., Wolford, M., Giuliani, J., Lehmberg, R., Friedman, M., Hegeler, F., Jaynes, R., Abdel-Khalik, S., Sadowski, D. and Schoonover, K., “Electra: An Electron Beam Pumped KrF Rep-Rated Laser System for Inertial Fusion Energy”, *Fusion Science and Technology*, Vol. 56, pp. 346-351, 2009.

Chatterjee, A. and Deviprasath, L., “Heat Transfer in Confined Laminar Axisymmetric Impinging Jets at Small Nozzle-Plate Distances: the Role of Upstream Vorticity Diffusion”, *Numerical Heat Transfer, Part A*, Vol. 39, pp. 777-800, 2001

Choi, M., Yoo, H., Yang, G., Lee, J. and Sohn, D., “Measurements of Impinging Jet Flow and Heat Transfer on a Semi-Circular Concave Surface”, *Int. J. Heat Mass Flow*, Vol. 43, pp. 1811-1822, 2000

Dano, B., Liburdy, J. and Kanokjaruvijit, K, "Flow Characteristics and Heat Transfer Performances of a Semi-confined Impinging Array of Jets: Effect of Nozzle Geometry", *Int. J. Heat and Mass Transfer*, Vol. 48, pp. 691-701, 2005

Gardon, R. and Akfirat, J., "The Role of Turbulence in Determining the Heat-Transfer Characteristics of Impinging Jets", *Int. J. Heat Mass Transfer,* Vol. 8, pp. 1264-1272, 1965.

Gardon, R. and Akfirat, J., "Heat Transfer Characteristics of Impinging Two-Dimensional Air Jets", *J. Heat Transfer,* Vol. 88, pp. 101-108, 1966.

Garimella, S. and Rice R., "Confined and Submerged Liquid Jet Impingement Heat Transfer", *J. Heat Transfer*, Vol. 177, pp. 871-877, 1995

Giuliani, J., Hegeler, F., Sethian, J., Wolford, M., Myers, M., Abdel-Khalik, S., Sadowski, D., Schoonover, K. and Novak, V., "Foil Cooling for Rep-Rated Electron Beam Pumped KrF Lasers", *J. Phys. IV France,* Vol. 133, pp. 637-639, 2006.

Giuliani, J., Hegeler, F., Sethian, J., Wolford, M., Myers, M., Abdel-Khalik, S., Sadowski, D. and Schoonover, K., "Foil Cooling for Rep-Rated Electron Beam Pumped KrF Lasers", *Proceedings of 33rd IEEE International Conference on Plasma Science*, Jun. 4-8, Traverse City, MI, USA, 2006.

Glynn, C. and Murray, B., "Jet Impingement Cooling in Microscale", *ECI International Conference on Heat Transfer and Fluid Flow in Microscale,* Castelvecchio Pascoli, Italy, Sep. 25-30, 2005

Goldstein, R.,"Film Cooling", *Advances in Heat Transfer*, Vol. 7, pp. 321-379, Irvine Jr., T. and Harnett, J., *Ed*., Academic Press, New York, NY, 1971.

Goldstein, R., Behbahani, A. and Heppelmann, K., "Streamwise Distribution of the Recovery Factor and the Local Heat Transfer Coefficient to an Impinging Circular Air Jet", *Int. J. Heat Mass Transfer*, Vol. 29, pp. 1227-1235, 1986.

Hartnett, J., Birkebak, R. and Eckert E., "Velocity Distributions, Temperature Distributions, Effectiveness and Heat Transfer for Air Injected through a Tangential Slot into a Turbulent Boundary Layer", *J. Heat Transfer*, Vol. 83, pp. 293-306, 1961.

Hegeler, F., Giuliani, J., Sethian, J., Myers, M., Wolford, M. and Friedman, M., "Thermal Loading of Thin Metal Foils Used as Electron Beam Windows for a KrF Laser", *Proceedings of 15th IEEE International Pulsed Power Conference*, Monterey, CA, USA, Jun. 13-17, 2005.

Hegeler, F., Burns, P., Giuliani, J., Sadowski, D. and Schoonover, K., "Hibachi Foil Cooling", *NIKE Meeting Presentation*, June 2007.

Hegeler, F., Giuliani, J., Sethian, J., Myers, M., Wolford, Burns, P. and Friedman, M., "Forced Convective Cooling of Foils in a Repetitively Pulsed Electron-Beam Diode", *IEEE Transactions of Plasma Science,* Vol. 36, pp. 778-793, 2008.

Huang, L. and El-Genk, M., "Heat Transfer of an Impinging Jet on a Flat Surface", *Int. J. Heat Mass Transfer*, Vol. 37, pp. 1915-1923, 1994.

Incropera, F. and DeWitt, D., *Fundamentals of Heat and Mass Transfer,* 5th ed., John Wiley and Sons, 2002.

Jambunathan, K., Lai, E., Moss, M. and Button, B., "A Review of Heat Transfer Data for Single Circular Jet Impingement", *Int. J. Heat and Fluid Flow*, Vol. 13, pp. 106-115, 1992.

Jansson, L. S., Davidson, L. and Olsson, E., "Calculation of Steady and Unsteady Flows in a Film-Cooling Arrangement Using a Two-Layer Algebraic Stress Model", *Numerical Heat Transfer*, Part A, Vol.25, pp.237-258, 1994.

Kercher, D. and Tabakoff, W., "Heat Transferf by a Square Array of Round Air Jets Impinging Perpendicular to a Flat Surface Including the Effect of Spent Air", *J. Engineering for Power,* Vol. 92, pp. 73-82, 1970

Kim, S.-E. and Choudhury, D., "A Near-Wall Treatment Using Wall Functions Sensitized to Pressure Gradient", *ASME FED*, *Separated and Complex Flow*, Vol. 217, pp. 273-279, 1995

Klein, J. and Tribus, M., “Forced Convection from Non-Isothermal Surfaces”, *Heat Transfer, a Symposium*, University of Michigan Press, Ann Arbor, MI, 1953.

Launder, B. and Rodi, W., “The Turbulence Wall Jet – Measurement and Modeling”, *Annual Review of Fluid Mechanics*, Vol.15, pp.249-459, Annual Review Inc., Palo Alto, CA, 1983.

Lee, X., Ma, C., Zheng, Q., Zhuang, Y. and Tian, Y., “Numerical Study of Recovery Effect and Impingement Heat Transfer with Submerged Circular Jets of Large Prandtl Number Liquid”, *Int. J. Heat Mass Transer,* Vol. 40, pp. 2647-2653, 1997.

Lefebvre, A., *Gas Turbine Combustion*, Taylor and Francis, London, 1999.

Lin, Z., Chou, Y. and Hung, Y., “Heat Transfer Behaviors of a Confined Slot Jet Impingement”, *Int. J. Heat Mass Transfer,* Vol. 40, pp. 1095-1107, 1997.

Lu, B., Abdel-Khalik, S., Sadowski, D., Schoonover, K., Hegeler, F., Burns, P. and Sethian, J., “Electra KrF Laser Hibachi Foil Cooling with Near-Wall Jets”, *Fusion Science and Technology*, Vol. 56, pp. 441-445, 2009.

Martin, H, ”Heat and Mass Transfer between Impinging Gas Jets and Solid Surfaces”, *Advances in Heat Transfer*, Vol. 13, pp. 1-60, Irvine Jr., T. and Harnett, J., *Ed.*, Academic Press, New York, NY, 1977.

Metzger, D., Florschuetz, L., Takeuchi, D., Behee, R. and Berry, R., “Heat Transfer Characteristics for Inline and Staggered Arrays of Circular Jets with Crosslfow of Spent Air”, *J. Heat Transfer*, Vol. 101. pp. 526-531, 1979.

Novak, V., Sadowski, D., Shin, S., Schoonover, K. and Abdel-Khalik, S., “Experimental and Numerical Investigation of Mist Cooling for the Electra Hibachi”, *Fusion Science and Technology*, Vol. 47, pp.610-615, 2005.

Novak, V., Abdel-Khalik, S., Sadowski, D. and Schoonover, K., “Investigation of Mist Cooling for the Electra KrF Laser Hibachi”, *Fusion Science and Technology,* Vol. 52, pp. 483-488, 2007.

Perry, K., “Heat Transfer by Convection from a Hot Gas Jet to a Plane Surface”, *Proceedings of the Institution of Mechanical Engineers*, Vol. 168, pp. 775-784, 1954.

Salamah, S. and Kaminski, D., “Modeling of Turbulent Heat Transfer from an Arrya of Submerged Jets Impinging on a Solid Surface”, *Numerical Heat Transfer, Part A,* Vol. 48, pp. 315-337, 2005.

San, J., Huang, C. and Shu, M., “Impingement Cooling of a Confined Circular Air Jet”, *Int. J. Heat Mass Transfer*, Vol. 40, pp. 1355-1364, 1997.

San, J. and Lai, M., “Optimum Jet-to-Jet Spacing of Heat Transfer for Staggered Arrays of Impinging Air Jets”, *Int. J. Heat and Mass Transfer*, Vol. 44, pp. 3997-4007, 2001.

San, J., Tsou, Y. and Chen, Z, “Impingement Heat Transfer of Staggered Arrays of Air Jets Confined in a Channel”, *Int. J. Heat and Mass Transfer,* Vol. 50, pp. 3718-3727, 2007.

Saripalli, K., “Visualization of Multijet Impingement Flow”, *AIAA Journal*, Vol. 21, pp. 483-484, 1983.

Seban, R., “Heat Transfer and Effectiveness for a Turbulent Boundary layer with Tangential Fluid Injection”, *J. Heat Transfer, Series C,* Vol. 82, pp. 303-312, 1960.

Seban, R. and Back, L., “Velocity and Temperature Profiles in a Wall Jet”, *Int. J. Heat Mass Transfer*, Vol. 3, pp. 255-265, 1961.

Sethian, J., Friedman, M., Giuliani, J., Lehmberg, R., Myers, M., Obenschain, S., Hegeler, F. and Swanekamp, S., “Fusion Electra: A Krypton Fluoride Laser for Fusion Energy”, *Proceedings of Inertial Fusion Sciences and Applications Conference (IFSA)*, Kyoto, Japan, Sep. 10-15, 2001.

Sethian, J., Friedman, M., Giuliani, JR., J., Lehmberg, R., Obenschain, S., Kepple, P., Wolford, M., Hegeler, F., Swanekamp, S., Weidenheimer, D., Welch, D., Rose, D and Searles, S., “Electron Beam Pumped KrF Lasers for Fusion Energy”, *Physics of Plasma*, Vol. 10, No. 5, pp. 2142-2146, 2003.

Sethian, J., Myers, M., Giuliani, JR., J., Lehmberg, R., Kepple, P., Obenschain, S., Hegeler, F., Friedman, M., Wolford, M., Smilgys, R., Swanekamp, S., Weidenheimer, D., Giorgi, D., Welch, D., Rose, D., and Searles, S., "Electron Beam Pumped Krypton Fluoride Lasers for Fusion Energy", *Proceedings of the IEEE*, Vol. 92, No. 7, pp. 1043-1056, 2004.

Shih, T-H., Liou, W., Shabbir, A., Yang, Z. and Zhu, J., "A New *k-ε* Eddy Viscosity Model for High Reynolds Number Turbulent Flows", *Computer and Fluids,* Vol. 24, No. 3, pp. 227-238, 1995

Simon, F., "Jet Model for Slot Film Cooling with Effect of Free Stream and Coolant Turbulence", *NASA TP 2655*, Oct., 1986.

Smirnov, V., Verevochkin, G. and Brdlick, P., "Heat Transfer between a Jet and a Held Plate Normal to Flow", *Int. J. Heat Mass Transfer*, vol. 2, pp. 1-7, 1961.

Souris, N., Liakos, H. and Founti, M, "Impinging Jet Cooling on Concave Surfaces", *AIChe Journal*, Vol. 50, pp. 1672-1683, 2004

Stollery, J. and El-Ehwany, A., "A Note on the Use of Boundary-Layer Model for Correlating Film Cooling Data", *Int. J. Heat Mass Transfer*, Vol. 8, pp. 55-65, 1965.

Viskanta, R., "Heat Transfer to Impinging Isothermal Gas and Flame Jets", *Experimental Thermal and Fluid Science,* Vol. 6, pp. 111-134, 1993.

Wieghardt, K., "Hot Air Discharge for De-Icing", *Air Material Command,* AAF Translations No. F-TS-919-RE, December, 1946.

Yang, Y. and Wang, Y., "Three-Dimensional Numerical Simulation of an Inclined Jet with Cross-Flow", *Int. J. Heat Mass Transfer*, Vol. 48, pp. 4019-4027, 2005.

Zhou, J., Salcudean, M. and Gartshore, I., "A Numerical Computation of Film Cooling Effectiveness", *Near-Wall Turbulent Flows,* Elsevier Science Publisher, The Netherlands, pp. 377-386, 1993.

Zhou, D. and Lee, S., "Forced Convective Heat Transfer with Impinging Rectangular

Jets", *Int. J. Heat Mass Transfer*, Vol. 50, pp. 1916-1926, 2007.

VITA

Bo Lu was born on March 23, 1980 in Xinchang County, Zhejiang Province, P. R. China, where he attended grade school and high school. He was enrolled in the Department of Engineering Physics, Tsinghua University in September 1998 and graduated with a Bachelor of Engineering in Nuclear Engineering and Technology in July 2002. From October 2002 to December 2003, he worked as a research engineer in the Institute of Plasma Physics, Chinese Academy of Sciences mainly on X-ray spectrum measurements for determining electron temperatures for magnetic confinement fusion research before he was accepted into the Nuclear Engineering Department at the University of Tennessee, Knoxville. He obtained his Master of Science degree in Nuclear Engineering in May 2006 and began to pursue his Ph.D. in Nuclear Engineering at the Georgia Institute of Technology in August 2006, where he has been continuously working on experimental and numerical heat transfer in the near-wall jets for electron beam pumped gas lasers as part of the inertial fusion energy research.